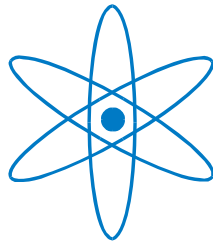


Physik – Department



**Assembly of Engineered Spider Silk in Microfluidic  
Devices and Free Surface Flow**

Dissertation

von

Sebastian Rammensee

**TECHNISCHE UNIVERSITÄT MÜNCHEN**





# **TECHNISCHE UNIVERSITÄT MÜNCHEN**

Physik – Department  
Lehrstuhl für Biophysik E27

## **Assembly of Engineered Spider Silk in Microfluidic Devices and Free Surface Flow**

Sebastian Rammensee

Vollständiger Abdruck der von der Fakultät für Physik der Technischen Universität München zur Erlangung des akademischen Grades eines  
Doktors der Naturwissenschaften  
genehmigten Dissertation.

Vorsitzender: Univ.-Prof. Dr. Roland Netz

Prüfer der Dissertation:

1. Univ.-Prof. Dr. Andreas Bausch
2. Univ.-Prof. Dr. Friedrich Simmel

Die Dissertation wurde am 16.06.2009 bei der Technischen Universität München eingereicht und durch die Fakultät für Physik am 17.07.2009 angenommen.



Technische Universität München  
Physik-Department  
E27-Biophysik

Dissertation

**Assembly of Engineered Spider Silk  
in Microfluidic Devices and Free  
Surface Flow**

Sebastian Rammensee

June 2009



# Contents

<b>1. Summary</b>	<b>1</b>
<b>2. Introduction</b>	<b>5</b>
2.1. Spider Silk . . . . .	5
2.2. Natural assembly process of silk . . . . .	9
2.3. Spider Silk's mechanical properties . . . . .	11
2.4. Hydrophobic Effect . . . . .	13
2.5. Shear Induced Aggregation . . . . .	14
2.6. Microfluidic Devices . . . . .	15
2.7. Elongational Flow . . . . .	16
<b>3. Materials and Methods</b>	<b>21</b>
3.1. FEM Simulation of Flow . . . . .	21
3.2. Fabrication of Microfluidic Devices . . . . .	22
3.3. Recombinantly produced spider silk proteins and peptides . . . . .	23
3.3.1. Engineered Spider Silks . . . . .	23
3.3.2. Fragments of engineered spider silk proteins . . . . .	26
3.3.3. Solvents . . . . .	27
3.4. Protein Analysis . . . . .	27
3.4.1. UV Spectroscopy . . . . .	27
3.4.2. Infrared Spectroscopy . . . . .	28
3.5. Scanning Electron Microscopy . . . . .	29
3.6. Rheometry . . . . .	29
3.6.1. Shear Viscosimetry . . . . .	30
3.6.2. Elongational Viscosimetry . . . . .	30
3.6.3. Apparent Elongational Viscosity in CABER . . . . .	31
3.6.4. Experimental Setup for CABER . . . . .	33
3.6.5. High-speed imaging . . . . .	34
3.6.6. Elongational Viscosimetry Data Analysis . . . . .	34
3.6.7. Sample system: Polyacrylamide solutions . . . . .	35
3.7. Fiber Tester Setup . . . . .	37
3.7.1. Linearity of Motor . . . . .	37
3.7.2. Climatized Chamber . . . . .	37
3.7.3. Force Sensor . . . . .	38
3.7.4. Sample preparation for fiber testing . . . . .	38
<b>4. Shear induced aggregation: First insights into silk assembly</b>	<b>41</b>
4.1. Shear-activated aggregation of eADF3 with phosphate . . . . .	41
4.2. Shear Ramps . . . . .	43
4.3. Shear Hold . . . . .	43

4.4. Discussion of the shear activated aggregation . . . . .	45
<b>5. Mimicking a spider's spinning duct by microfluidics</b>	<b>47</b>
5.1. Design and Characterization of Microfluidic Channels . . . . .	47
5.2. Assembly Process in the microfluidic channels . . . . .	49
5.2.1. eADF3 assembles into fibers under certain conditions . . . . .	49
5.2.2. eADF4 always assembles into spherical aggregates . . . . .	52
5.2.3. Blends of eADF3 and eADF4 form stable fibers . . . . .	52
5.2.4. Mode of action of pH change, phosphate addition, and flow effects . . . . .	53
5.3. Characterization of Spider Silk Aggregates formed in the Channels	55
5.3.1. Secondary Structure composition . . . . .	55
5.3.2. Stability in denaturing agents . . . . .	57
5.3.3. Water content . . . . .	59
5.3.4. Mechanical testing of short fibers . . . . .	60
5.4. Analysis of the Flow Conditions that lead to Fiber Formation . . . . .	62
5.4.1. Shear thinning behaviour of concentrated eADF solutions . . . . .	62
5.4.2. Simulation of the flow in Fiber forming channels . . . . .	64
5.5. Discussion of the Fiber assembly process . . . . .	65
5.5.1. Assembly kinetics . . . . .	65
5.5.2. Differences between eADF3 and eADF4 . . . . .	67
5.5.3. Influence of elongational flow . . . . .	67
5.5.4. Further Directions of Research . . . . .	68
<b>6. Capillary Breakup: Rheology and Fiber formation</b>	<b>69</b>
6.1. Ohnesorge Number . . . . .	70
6.2. Elongational Viscosity of eADFs in aequos solution . . . . .	70
6.2.1. Elongational Rheology of dilute solutions of eADF3 . . . . .	71
6.2.2. Elongational Rheology of Highly Concentrated Phase eADF3	72
6.2.3. Discussion . . . . .	75
6.3. eADF Rheology in nonaequos solvents . . . . .	76
6.4. Thread Formation . . . . .	80
6.5. Mechanical properties of formed fibers . . . . .	81
6.6. Effect of Methanol treatment . . . . .	82
6.7. Molecular Weight Dependence of the Mechanical Stability . . . . .	83
6.8. Natural Spider Silk . . . . .	85
<b>7. Discussion and Outlook</b>	<b>89</b>
<b>Bibliography</b>	<b>92</b>
<b>Appendix</b>	<b>100</b>
<b>A. Structural Comparison of Films formed from engineered spider silk and short fragments</b>	<b>101</b>



<b>B. Fabrication of PDMS Microfluidic Devices</b>	<b>105</b>
B.1. Preparation of Masters . . . . .	105
B.2. Preparation of PDMS Replicas . . . . .	106
B.3. Preparation of Microfluidic Devices for Experiments . . . . .	107
<b>C. Block Diagram for Fiber Tester</b>	<b>109</b>



# Thank you!

Vielen Dank an die folgenden Menschen:

- An erster Stelle möchte ich mich bei Prof. Dr. Andreas Bausch bedanken. Er hatte die Idee zum Thema dieser Dissertation, und hat mich mit seinem unerschütterlichen Optimismus so manches mal neu motiviert. Eine vergleichbare Umgebung, die jungen Leuten so viel Freiheit und trotzdem immer eine offene Tür zum Gespräch mit dem Chef bietet, wird man lange suchen müssen!
- Prof. Dr. Thomas Scheibel möchte ich für die viele Spinnenseide danken, und für das Beantworten meiner unzähligen Fragen. Vielen Dank auch für die Gutachten! Übrigens: Tut mir immer noch leid wegen der Pizza...
- Dr. Daniel Huemmerich, Ute Slotta, David Keerl und Andreas Lammel danke sehr herzlich ich für die Versorgung mit Spinnenseidenprotein, und unendliche Geduld beim Erklären der Geheimnisse der Spinnenseidenproduktion.
- Martin Schmidt, der eigens seine Bioreaktoren für meine AQ24NR3 Produktion angeschmissen hat.
- Lin Römer und der AMSilk GmbH danke ich ebenfalls für das zur Verfügung gestellte Spinnenseidenprotein.
- Kristina Spieß für das biotynilierte C16.
- Christian Freudiger, Markus Harasim, Heinrich Grabmayr waren eine große Hilfe bei der Herstellung der Mikrofluidik-Kanäle. Es hat großen Spaß gemacht, mit euch zu basteln!
- Bernhard Wunderlich und Uli Kleßinger möchte ich für die vielen hilfreichen Diskussionen zum Fluß in Mikrokanälen danken.
- Dr. Marianne Hanzlik für die Hilfe bei der Elektronenmikroskopie.
- Dr. Kevin Hermanson, Dr. Cyrille Vézy, Dr. John Hardy für viele Diskussionen zur Spinnenseide, Einkapselung und Fäden!
- Prof. Dr. Christian Wagner für lehrreiche Diskussionen zur Elongationsrheometrie.
- Melanie Reisinger für die Kraftmessungen mit der optischen Falle.
- Dr. Mireille Claessens und Dr. Pablo Fernandez waren und sind wirklich großartige Bürokollegen.

## Contents

- Felix Berkemeier für IGORpong,
- Allen anderen am E22/E27, die ich noch nicht explizit erwähnt habe, möchte ich für die großartige Atmosphäre danken!
- Besonders erwähnenswert natürlich: Ein Hoch auf alle vergangenen und zukünftigen Kaffeeminister!
- Meinen langjährigen Mitbewohnerinnen und Mitbewohner Veronika Klinger, Friederike Sigmund, Tobias Töpfer und Esther Vitt danke ich für ihre Nachsicht mit den 'verschobenen' Putzdiensten.
- Zu guter Letzt: Meinen wunderbaren Eltern danke ich für sehr Vieles, nicht nur für die Unterstützung, die mir ein sorgenfreies Studium ermöglicht hat.

# 1. Summary

Spider silk threads are formed by the irreversible aggregation of silk proteins in a spinning duct with dimensions of only a few micrometers. Here, we present a microfluidic device in which engineered and recombinantly produced spider dragline silk proteins eADF3 (engineered *Araneus Diadematus* Fibroin) and eADF4 are assembled into fibers. Our approach allows the direct observation and identification of the essential parameters of dragline silk assembly. Changes in ionic conditions and pH value result in aggregation of both proteins. Assembly of eADF3 fibers was only induced in the presence of an elongational flow component. Strikingly eADF4 only formed fibers in combination with eADF3.

In spiders, the spinning duct is a thin S-shaped channel of up to several centimeters in length (depending on spider species and body weight), surrounded by secretory cells that are involved in adjusting the ionic conditions and pH. Thus, flow conditions in spider glands can be technically best mimicked by microfluidic devices: laminar flow conditions enable precise control of ion concentrations and pH values along the channel, and elongational flow conditions can be easily adjusted. Different designs of microfluidic channels allow disentangling various effects, since the solvent conditions can be varied in combination with various flow conditions, and thus all processes can be observed optically in a time resolved manner. Therefore, microfluidic devices enable examination of all parameters necessary for assembly of spider silk proteins.

In the microfluidic channels, moderate flow rates render Brownian motion the dominating cause of aggregation of spherical protein colloidal assemblies. The aggregation rate  $A$  is proportional to the density of particles  $N$ , their radius  $R$ , and their diffusion constant  $D$ . In the proximity of the small orifice in the microfluidic device, particles traveling along the streamlines of the medium are forced into contact, drastically increasing the aggregation rate. Under these conditions, aggregation rate  $A$  is proportional to the shear rate and to the third power of the particles' radius  $R$ .

As the fluids that are important in silk fiber formation in the engineered spinning ducts show highly non-Newtonian complex fluid behaviour, a thorough rheological analysis of the involved protein solutions was performed. From this

## 1. Summary

results, parameters for constitutive models, such as the Carreau-Yasuda model for shear thinning fluids, were obtained. The flow conditions in the microfluidic channels were then simulated by Finite Element Simulations, using the experimentally obtained parameters. Of particular interest was the determination, where in the microfluidic devices the flow would be a shear flow or rather an elongational flow. This was quantified by a dimensionless flow-type parameter,  $\xi$ .

eADF4 spherical colloidal assemblies are apparently "smooth", no dangling ends stick out and contribute to sticking interactions with neighboring colloidal assemblies. In contrast, eADF3 spherical colloidal assemblies are supposed to have dangling ends which can mediate interactions between neighboring aggregates. Moreover, eADF3 spherical aggregates can be dissolved before aggregation into fibers.

Interestingly, eADF4 can be incorporated into fibers, when eADF3 is also present. This could be shown in an experiment, where only eADF4 was fluorescently labeled. Fibers formed of a mixture of the two protein species show homogenous fluorescence.

In summary, if no shear forces are present, eADF3 aggregates into spheres. If shear flow is present, eADF3 can be driven into an aggregation form with very similar morphology to silk fibers spun by living animals. In order to test which of the involved processes are necessary for fiber formation, we divided the experiment into different parts, by introducing different solutions into the microfluidic device and/or by changing the geometry of the device.

In order to produce longer fibers that are suitable for mechanical testing, we intended to implement drying of the fiber on the microfluidic device. However, surface tension will immediately break up the fluid filament into droplets. The solution to this problem lies in increasing the viscosity of the solutions used to produce fibers. A very high elongational viscosity has been reported for spinning dope from spider's spinning glands.

In order to elucidate how important the elongational viscosity is for fiber formation, and how it changes with protein concentration and protein molecular weight, an experimental setup was developed to assess this important material parameter experimentally. The new elongational viscosimeter relies on the principle of capillary breakup.

It was found that at a concentration of 100 mg/ml, the 88 kDa Protein C32 was able to form stable fibers, while at the same mass concentration, the 44 kDa C16 does not show a sufficient elongational viscosity to undergo the liquid-solid

transition required for the formation of fibers.

The newly constructed elongational viscosimeter was extended in such a way that force-strain measurements of the produced fibers were possible. In the focus of our research was the dependence of mechanical properties from the molecular mass of the proteins. It was found, that fibers consisting of exclusively the longest engineered silk proteins were forming the most extensible and most stable fibers. Fibers which had a high amount of small fragments added were brittle and showed only little resistance to mechanical stress.

In the end, this and further studies will allow to connect molecular properties (amino-acid sequence) and processing conditions with resulting mechanical properties.





## 2. Introduction

### 2.1. Spider Silk

Silks are a lightweight and strong biomaterial composed of aggregated protein [Scheibel, 2005a]. Remarkably, the stability of silk materials is not caused by covalent chemical bonds, but by the collective action of many hydrogen bonds. These form between certain amino acid residues on the protein backbones, thus forming crystalline intermolecular  $\beta$ -sheets. Combined with loosely entangled parts of the polymer, these crystalline regions ultimately lay the foundation for the material's unique combination of toughness and extensibility.

In contrast to other biomaterials such as bone, tendon and hair, silks are produced not by relatively slow growth processes, but are spun almost instantaneously at the time of necessity. The spinning process has thus evolved to satisfy two needs of the spider: it allows the spider to control the properties of the fiber and to produce the fiber at a range of useful speeds for different purposes.

Spiders belong to the class of *Arachnida* with approximately 110 families and about 40,000 species known to date. They have eight legs on a body that is divided into two parts, the cephalothorax and the abdomen. Many spider species hunt prey by means of special webs. After building a web, these spiders will wait motionless for small animals, typically insects, to get trapped in the web. Spiders can sense very fine vibrations of the web with their legs and are able to detect the impact of an insect immediately.

Spiders are able to produce a certain variety of fiber types, which serve different well-defined purposes in the makeup of the web. These different silk types are produced in distinct silk glands at the lower abdomen. Most spiders have six silk glands (Figure 2.3).

The two main silk types that spiders use to construct their webs are dragline silk and flagelliform silk. Dragline silk is used for as the lifeline of the spider. A short piece of dragline silk is always available at the abdomen of the spider, in order to be quickly attached or glued to any fixed ground, and thereby securing the spider from falling down. The other purpose of Dragline silk is the makeup

## 2. Introduction

of the web's frame (see Figure 2.2). Dragline silk's mechanical properties are characterized by a relatively low extensibility and a very high rupture stress (Table 2.1).

Silk type	Extensibility	Rupture Stress [GPa]	Toughness [MJ/m <sup>3</sup> ]
Dragline Silk	0.27	1.1	160
Catchline Silk	2.7	0.5	150
Kevlar	0.025	3.6	50
Steel	0.008	1.5	6

**Table 2.1.:** Mechanical properties of the most important silk fiber types and some other materials.

Flagelliform silk is produced in the Major Ampullate gland. It is used to build the capture spiral of the web (Figure 2.2). In contrast to dragline silk, Flagelliform silk is highly extensible, with a relatively low tensile strength. However, the toughness almost matches that of dragline silk (Table 2.1).

### Structure-Function relations in silk proteins

Generally, the structure of proteins is determined by their function. For example, DNA binding proteins such as nucleases are not much larger than the features they recognize (see figure 2.1). In general, one can state that proteins are usually not much larger than the resulting combination of functional domains for enzymatic reactivity or for binding specific ligands.

This is fundamentally different for silk proteins. Silk proteins do not possess enzymatic activity. Most parts of silk proteins are even natively unfolded in solution, so that one could say that silk proteins do not have a tertiary structure, but are functional only on the level of quaternary structure. As described above, silks are stable due to many intermolecular beta-sheet structures. As protein size, and thus amino acid sequence length, is usually determined by the required size to accommodate reactive areas, regulatory domains and spacing relative to targets in the cell, this is not the case for the repetitive spider silk proteins. They seemingly exhibit an arbitrary number of almost identical repeats. One question of interest in the understanding of silk materials is thus, why silk proteins are so large.

On a molecular level, spider silk proteins consist of a region of repetitive sequences and of a non repetitive, N-terminal domain. The purpose of the N-terminal domain seems to be mainly the control of the assembly process (Hagn 2009) and it is thought to contribute only weakly to the stability of the fiber.

It is the repetitive sequences, which usually make up approximately 90-95 % of the molecular mass and provide the sequence features which allow for intermolecular beta-sheet formation. The sum of many hydrogen bonds in these intermolecular beta sheets accounts for the great stability of spider silk fibers.



**Figure 2.1.:** Typically, the size of proteins is given by their purpose in the cell. Here are a few examples: Left, structure of Myoglobin. The protein is just large enough to accommodate the prosthetic Heme group and provide the necessary chemical environment (Protein Data Base # 2O5T). Middle, structure of the restriction nuclease EcoRI together with the DNA it is binding to. The protein is not much larger than the DNA sequence it has to detect (Protein Data Base # 2OXV). Right, spider silk molecules consist of a seemingly arbitrary number of repeats of very similar motifs. Crystalline areas are embedded in an amorphous matrix. A single spider silk protein does not show a defined tertiary structure (from [Glisovic et al., 2008])

Questions that can be asked concerning the molecular mass of spider silk proteins, and that are addressed in this thesis include

- Are the mechanical properties of silks related to the molecular mass of their constituting proteins?
- Do flow properties of the spinning dope depend on the molecular weight of the proteins in solution?

### **Availability of Spider Silk and Commercial Applications**

Since literally thousands of years, silks are used commercially, mostly as fibers for clothing. Virtually all commercially used silk has been and is generated by the silkworm *Bombyx Mori*. Silkworm silk fibers are less tough and much less extensible than spider silk fibers, but perfectly useful for most clothing purposes.

Since spider silk was extremely difficult and thus expensive to produce in relevant amounts, its role in commercial applications has been limited to very special

## 2. Introduction

purposes such as representative clothing for outstandingly rich or powerful persons.

As already stated, the availability of spider silk as a biomaterial is very limited. In order to provide for more and well defined amounts purified spider silk protein, the genes encoding for spidroin proteins have been expressed in bacteria. To this end, the nucleic acid codon usage had to be adopted, which means that the genes had to be synthesized completely from scratch. Thus, these proteins are referred to as *engineered Araneus Diadematus Fibroins* (eADF) or spider-silk analogous proteins [Huemmerich et al., 2004c, Huemmerich et al., 2004a].

Producing engineered spider silk proteins recombinantly in bacteria provided new possibilities for the investigation of spinning processes. In this work, I employed previously established engineered variants of the dragline silk fibroins ADF3 and ADF4. One advantage of eADF3 and eADF4 is their easy accessibility at high purity. Under distinct solvent conditions these engineered silk proteins controllably assemble into different morphologies, such as nanofibrils [Huemmerich et al., 2004c], hydrogels [Rammensee et al., 2006], films [Huemmerich et al., 2006, Slotta et al., 2006] and microcapsules [Hermanson et al., 2007]. Further, conditions for a liquid-liquid phase separation have been identified leading to large colloidal assemblies which likely reflect a prerequisite for silk fiber formation [Exler et al., 2007b].

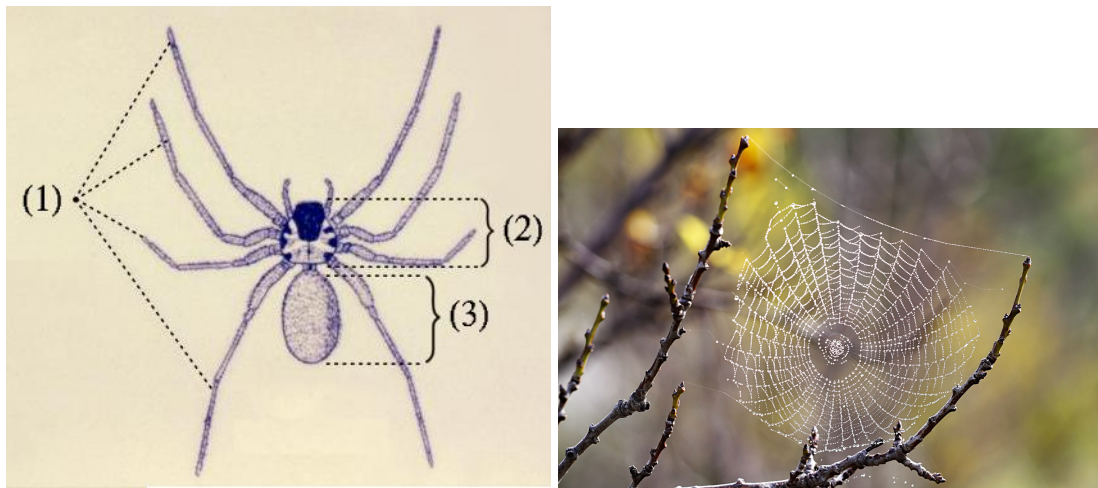


**Figure 2.2.:** Left: Sketch of a typical spider with typical body attributes: (1) Eight legs, (2) Cephalothorax, (3) Abdomen (Public Health Image Library, #5446). Right: A spider's web with dew drops. The frame of the web is made of stronger silk than the capture spiral, which is made of more elastic and ductile silk.

## 2.2. Natural assembly process of silk

As the natural assembly process of spider silk is a dynamic and microscopic process, it is generally difficult to investigate and thus not very well understood. There are two partially disparate models for fiber formation: One, proposed by Vollrath et al [Vollrath and Knight, 2001] assumes the silk molecules to be in a liquid crystalline state when passing through the spinning duct. Orientation of silk molecules is supposed to be achieved by shearing this nematic phase, and thus aligning silk molecules along the axis of the spinning duct.

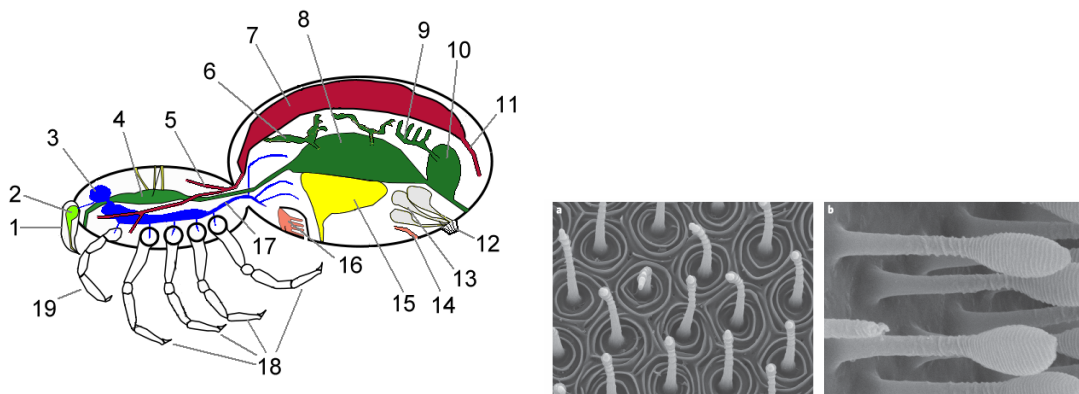


**Figure 2.3.:** Left: Organs of the spider. The spinning ducts (12) are located on the abdomen. (source: Wikipedia, based on [Ruppert et al., 2004]) Right: Electron micrographs of the outlets of the spinning ducts (spigots), where the silk threads actually leave the spider's body (source: Phylogeny of Spiders project, <http://research.amnh.org/atol/files/>)

The other model assumes that silk proteins are solubilized in the spinning gland. As salts are added in the passage through the spinning duct, the hydrophobic effect (see section 2.4) is increased, and the formation of micellar structures or clusters is initiated (Figure 2.4). This is due to the minimization of interactions with the solvent, when the hydrophobic parts of the silk molecules are hidden in the interior of the clusters [Jin and Kaplan, 2003].

It should be noted that the two models mentioned above are not completely mutually exclusive. Amphiphilic liquid crystals tend to assemble into micelles at low concentrations, whereas a favoured configuration at high concentrations consists of hexagonal columns. It has been proposed this could explain why in natural spinning dopes, liquid crystallinity is observed whereas *in vitro* (where usually lower protein concentrations are employed) micellar structures are observed in the spinning dope [Heim et al., 2009].

Both models are highly dynamic on a microscopic level, and thus hardly in-

## 2. Introduction

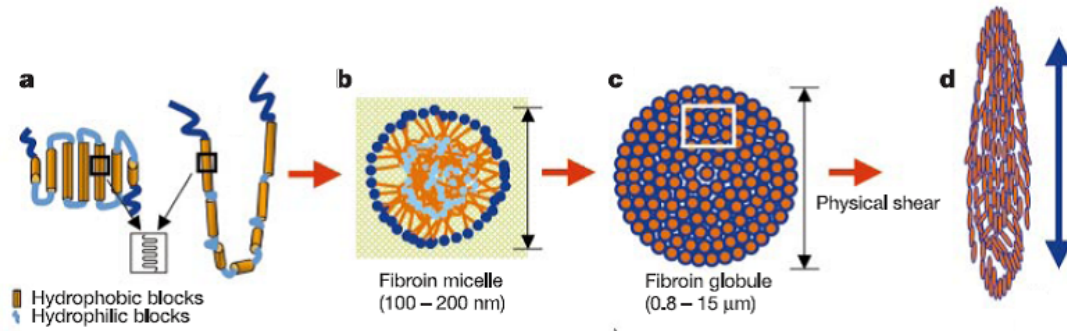


**Figure 2.4.:** Model for silk fiber formation proposed by [Jin and Kaplan, 2003]. Changes in the salt concentration lead to an increased hydrophobic effect, thus causing the proteins to hide hydrophobic regions in the inner part of micellar-like structures. As flow is aligning the globules, a fiber is formed.

investigated *in vivo*, and many details in the field remain to be solved. A good deal of studies have concentrated on rheological properties of the contents of the spinning duct. However, all of these studies suffer from poorly defined contents of the samples that were actually analyzed. Neither the exact composition of the proteins in those solutions are known, nor even the salt concentrations, as tissue had to be dissected in order to obtain the samples.

One common result of these experiments is, that shear causes aggregation and an increase in the viscosity of spinning gland extracts [Holland et al., 2006].

The morphology of the spinning apparatus has been well studied. For several spider species, micrographs of the lower abdomen with the spinning spigots were obtained by optical microscopy and scanning electron microscopy (Figures 2.3 and 2.5). Thus, different spigots for different silk variations could be identified.

Quantitative studies on the formation of spider silk have been difficult and rare, due to

1. Small size of the spinning organ.
2. Lack of purified protein solutions due to difficulties with expressing large proteins with repetitive sequences.
3. Lack of well-defined spinning dopes due to salts and sericin proteins in natural spinning dopes extracted from animals.
4. Only estimated data about flow conditions in the spinning duct.

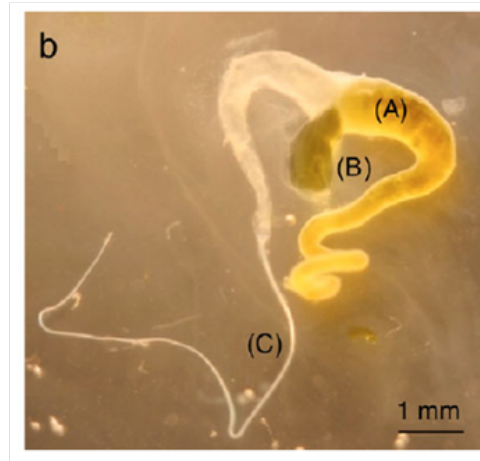


**Figure 2.5.:** (A) Dissected major ampullate (MA) gland of the spider. Visible is a  $\approx 1 \mu\text{L}$  blob (B) protruding through a rupture of the gland wall near the spinning canal (C). Figure from [Kojic et al., 2006]

#### Structure of Natural Spider Silk

The core of silk fibers consists of an amorphous matrix of supposedly oriented silk proteins, with  $\beta$ -sheet rich crystallites embedded. The crystalline areas are exceptionally rich in Alanin. Some authors describe a larger-scale order in fibers, and claim a non-uniform distribution of the silk protein species across the fiber diameter [Vollrath et al., 1996]. Also, using x-ray diffraction, substructures such as nanofibrils have been identified [Sapede et al., 2005].

Using an x-ray micobeam setup, it could also be shown that the orientation of  $\beta$ -sheet rich crystallites along the fiber axis increases with increasing strain [Glisovic et al., 2008].

From NMR studies, there is evidence that fibroin proteins assume a 'string of beads' hairpin folding in the fibers. In this model, there is no mechanical connectivity between the beads on one chain. However, mechanical connections are formed on the surfaces of the beads [Vollrath, 2005].

### 2.3. Spider Silk's mechanical properties

Extensive studies have been attempted to model the mechanical properties of spider silk [Porter et al., 2005]. An analytical, but complex model is the Hierarchical Chain Model [Zhou and Zhang, 2005], where a polymer is composed of many structural motifs which organize into structural modules and supramodules in a hierarchical manner. Such models were able to reproduce the data that was obtained on different silks, however relatively little insights were obtained using

## 2. Introduction

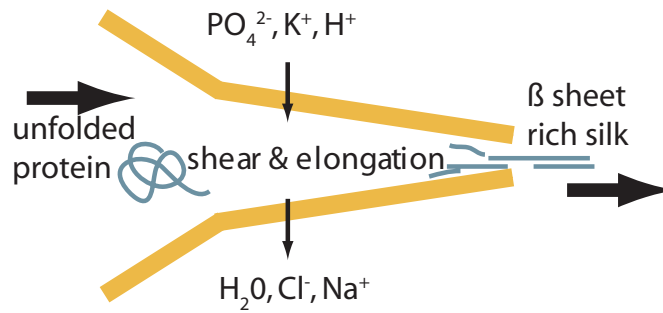


**Figure 2.6.:** Simplified sketch of the natural spinning process. Unfolded protein in solution is introduced to the spinning duct from the left. During the passage through the duct, ions are exchanged and water is extracted from the solution. At the end of the duct, silk molecules are aligned in the flow and exposed to post-spinning drawing.

these models as they possess many free variables.

Another model which makes stronger assumptions but is more straightforward considers the amorphous matrix as a mesh of springs, which are coupled to smaller domains with higher spring constant [Termonia, 1994]. The latter domains are to represent the crystalline regions in the fiber. All protein-protein-interactions are thus summed up in these spring constants. The model can actually predict shape of force-extension curves both the dry and supercontracted state. However, a volume fraction of 50 % has to be assumed for the crystallites, while in scattering experiments only about 30 % of of the fiber are found to be in crystalline order [Jelinski, 1998, Vollrath and Edmonds, 1989].

Other studies used molecular dynamics simulations to elucidate mechanical properties of short fragments of the silk fibers, such as the beta-sheet motifs, to extrapolate mechanical properties of whole fibers [Keten and Buehler, 2008]. It was found, that for single beta-strands, the highest shear resistance is found at a characteristic length scale of 3.1 residues (Figure 2.7). Beyond this length, the shear strength drops rapidly. When analyzing beta-strand stabilized proteins, they found that short beta-strands are more prevalent, and that there are only few strands with five or more residues in beta-strands.

A major problem in the development and application of quantitative models for silk elasticity is the great variability in silk properties found in nature. Environmental conditions, the diet of the animal prior to spinning, and the conduction of the spinning process itself contribute to the variation in mechanical properties [Madsen et al., 1999]. Using the bead size resulting from considering the 'string of beads' model and applying models that were used to predict material



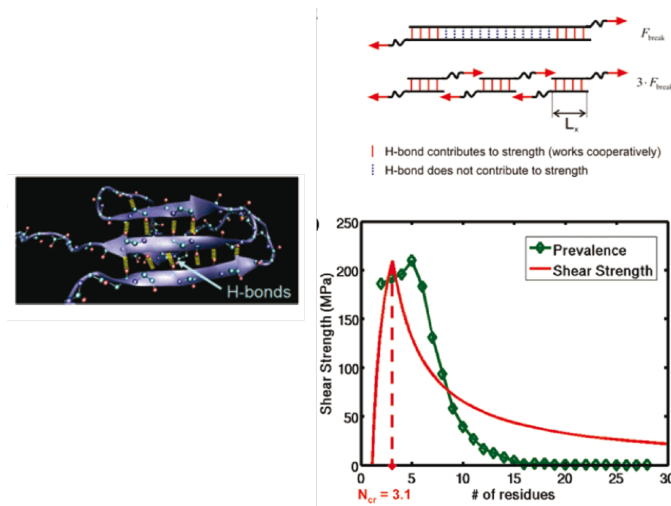


**Figure 2.7.:** Left: Three-strand system with free chains at the ends, as a model to study the strength of beta strands. Right: Shear strength of beta-sheets as a function of strand length and the prevalence of beta-sheet strand length. The highest shear resistance is found at a characteristic length scale of 3.1 residues. Beyond this length scale, the shear strength drops rapidly. The plot of the prevalence over the strand length illustrates that shorter beta-strands are more prevalent; in particular, strands that employ less than five residues are most common, and the prevalence decays sharply for longer strands. [Keten and Buehler, 2008].

properties of nanocrystalline metals and ceramics, it was possible to estimate correctly the observed strength of dragline silk (around 2 GPa) [Vollrath, 2006, Porter and Vollrath, 2009]. The fact that no long-distance mechanical connectivity along the fiber axis in this model also helps to explain why silks show a surprisingly low elastic modulus compare to their high strength.

## 2.4. Hydrophobic Effect

The Hydrophobic effect is a special case of solvent-solute interactions occurring in aqueous solutions. Hydrophobic effects are an important driving force for biological systems on a molecular level and specifically assume an important role in protein folding.

In this work, the hydrophobic effect and especially its dependence on the presence of salts in the solvent becomes important when protein solutions meet streams of salt solutions in the engineered spinning ducts.

For the transfer of a non-polar (np) molecule from non-polar solvent to water, a positive energy  $\Delta G_{np}$  is required.  $\Delta G_{np}$  can be decomposed into an enthalpic

## 2. Introduction

and an entropic contribution:

$$\Delta G_{np} = \Delta H_{np} - T\Delta S_{np}$$

$\Delta H_{np}$  is negligible at room temperature and thus the hydrophobic effect is driven by the entropic term  $\Delta S_{np}$ , which is negative.

The hydrophobic effect depends on the polarity and size of the solvent molecules, and on the salt content of the solvent. Ions, such as Potassium phosphate cause the water molecules to form cages of relatively ordered water molecules around them. This decreases the amount of water that is free, and thus decreases the entropy of the system.

Experiments on engineered spider silk proteins revealed that water-structure effects and dispersive interactions give contributions of comparable magnitude that largely cancel out. Thus, the correct modeling of peptide hydrophobicity must take the intimate coupling of solvation and dispersive effects into account [Horinek et al., 2008].

It should also be noted, the adhesion of silk proteins to surfaces of different hydrophobicity is influenced by the hydrophobicity of the silk protein in a given solution, indicating that hydrophobic and Hofmeister series effects are closely related [Geisler et al., 2008].

## 2.5. Shear Induced Aggregation

For many applications in engineering and food processing, precise control of the aggregation behaviour of particles in suspension is of interest. In most cases, stability of the suspension is desired and conditions to minimize unfavourable aggregation are to be found.

Aggregation occurs when it is energetically favourable for suspended particles to decrease the area that is exposed to the continuous phase. In an undisturbed liquid, the rate of aggregation is mainly governed by the Brownian motion of the particles.

Shear forces may influence the particles to overcome the energy barrier that keeps them in suspension and thus induce aggregation.

For modelling purposes, two particles that have met are considered as aggregated, and treated as a single particle afterwards. Using this approach, and considering uncharged particles, shear induced aggregation could be described as the balance

$$\frac{4N\phi\dot{\gamma}}{\pi} = \frac{16}{3}N^2a^3\dot{\gamma} \quad (2.1)$$

where  $N$  is the number of suspended particles,  $a$  is their hydrodynamic radius and  $\dot{\gamma}$  is the shear rate. Thus, the rate of aggregation depends linearly on the shear rate [Smoluchowski, 1917].

As protein aggregates are often charged, it is important to extend this result by introducing the interaction potentials between charged particles developed in the Derjagui-Landau-Verwey-Overbeek (DLVO) theory. When charge effects are taken into account, the rate of particle aggregation was found to be [Husband and Adams, 1992]:

$$\frac{-dN}{dt} \propto \frac{N^2a^3\dot{\gamma}^{0.82}}{W} \quad (2.2)$$

This result shows, that the rate of aggregation is strongly dependent of the interaction potential  $W$  but slightly less dependent on shear rates than in the case of uncharged particles.

While the arguments described above were true for particles that undergo Brownian motion, shear induced aggregation has also been found to be very prominent in suspensions of non-brownian particles [Guery et al., 2006]. Solid particles were found to aggregate at remarkably low volume fractions (smaller than 0.1). Furthermore, shear-induced aggregation was found to result in a dramatic increase in the viscosity. The increase in viscosity was found to occur after a shear-rate dependent induction time  $t_c$ . The induction time was found to follow the expression

$$t_c \propto \frac{1}{\dot{\gamma}^{F(\phi_g)}} e^{\frac{-\eta\dot{\gamma}a^2\delta}{k_B T} F(\phi_g)} \quad (2.3)$$

where  $F(\phi_g)$  is the probability of a particle to belong to a final solidlike cluster, at a volume fraction  $\phi_g$ . The parameter  $\delta$  is the length over which the interparticle repulsive potential is effective and  $a$  is the particle radius [Guery et al., 2006].

## 2.6. Microfluidic Devices

Microfluidic Devices consist of channels with typically less than 1 mm width, in many cases smaller than 100  $\mu\text{m}$ . Microfluidic devices are typically produced by photolithography, using techniques similar to those that have been originally developed for microelectronics.

Many aspects of fluid dynamics can be conveniently described by a set of dimensionless numbers, which weigh various physical properties against each

## 2. Introduction

other and thus provide qualitative descriptions of the flow.

For a description of microfluidic devices with typical lengthscale  $L$ , flow velocity  $v$ , typical polymer relaxation time  $\tau_p$ , density  $\rho$ , viscosity  $\eta$  and surface tension  $\sigma$  the following dimensionless numbers are most important [Squires and Quake, 2005]:

	Number	Formula	Description
Reynolds	Re	$\rho v L / \eta$	inertial/viscous
Weissenberg	Wi	$\tau_p / \dot{\gamma}$	relaxation / shear rate
Deborah	De	$\tau_p / t_{flow}$	relaxation / flow time
Ohnesorge	Oh	$\eta / \sqrt{\rho \sigma L}$	viscous / surface tension

**Table 2.2.:** Dimensionless numbers important for fluid flow in microfluidic devices.

Here, we focus on conditions for controlled aggregation necessary for fiber formation in a laminar flow. In spiders, the spinning duct is a thin S-shaped channel of up to several centimetres in length (depending on spider species and body weight), surrounded by secretory cells that are involved in adjusting the ionic conditions and pH [Jin and Kaplan, 2003, Vollrath and Knight, 2001]. Thus, flow conditions in spider glands can be technically best mimicked by microfluidic devices: laminar flow conditions enable precise control of ion concentrations and pH values along the channel, and elongation flow conditions can be easily adjusted. Different designs of microfluidic channels allow disentangling various effects, since the solvent conditions can be varied in respect to the various flow conditions and all processes can be observed optically in a time resolved manner. Therefore, microfluidic devices enable examination of all parameters necessary for assembly of spider silk proteins.

The modular architecture of our microfluidic devices (Figure 5.1) enables solvent adjustments similar to those found in nature by ion exchange and pH using different streams of liquids which are brought into contact. Further, an elongational flow component was applied by narrowing the channel width. Variation of the order of events in the microfluidic device allowed identifying the necessity of each individual contribution and the influence of the sequential order thereof.

### 2.7. Elongational Flow

The elongational viscosity of a fluid is a measure of its resistance to elongational deformations. It is defined as the ratio of the measured tensile stress and the rate of stretching. Therefore, a fluid's elongational viscosity is in the same relationship

to the shear viscosity as its Young's modulus is to the shear modulus for an elastic body.

For an incompressible Newtonian fluid, the elongational viscosity is exactly three times the shear viscosity [Trouton, 1906]. This can be derived as follows: For an idealized, shear free flow, the rate of strain tensor has only diagonal components different from zero:

$$\underline{\underline{\dot{\gamma}}} = \begin{pmatrix} 2a_1 & 0 & 0 \\ 0 & 2e_2 & 0 \\ 0 & 0 & 2a_3 \end{pmatrix} \quad (2.4)$$

For an incompressible fluid, the sum of the diagonal components vanishes,  $a_1 + a_2 + a_3 = 0$ . Simple elongational flow can be parametrized by

$$a_1 = d\epsilon/dt \quad (2.5)$$

$$a_2 = -1/2d\epsilon/dt \quad (2.6)$$

$$a_3 = -1/2d\epsilon/dt \quad (2.7)$$

$$(2.8)$$

In steady elongational flow, a constitutive parameter equivalent to viscosity relates the elongational stress difference (normal stress difference) to the elongational strain rate,

$$\tau_{11} - \tau_{33} = \bar{\eta}\dot{\epsilon} \quad (2.9)$$

For a Newtonian fluid,  $\tau = \eta_s d\gamma/dt$ , where  $\eta_s$  is the shear viscosity. Under simple elongational flow, this yields

$$\underline{\underline{\tau}} = \eta_s \begin{pmatrix} 2\dot{\epsilon} & 0 & 0 \\ 0 & -\dot{\epsilon} & 0 \\ 0 & 0 & -\dot{\epsilon} \end{pmatrix} \quad (2.10)$$

so,  $\tau_{11} - \tau_{33} = 3\eta_s d\epsilon/dt$ . Table 2.3 compares a few quantities commonly used to describe shear and elongational flow.

For non-Newtonian fluids such as silk solutions, the elongational viscosity is an independent material function that is not directly related to the shear viscosity. Consequently, the relation  $\tau_{11} - \tau_{33} = 3\eta_s d\epsilon/dt$  does not hold true for polymer solutions. Generally, elongational viscosity of these complex fluids is a function of the polymer stretching in the flow, the rate of elongation and of the total accu-

## 2. Introduction

Shear Flow	Elongational Flow
Deformation	Elongation
$\gamma = \frac{\Delta x}{h}$	$\epsilon = \frac{\Delta l}{l_0}$
Deformation Rate	Elongation Rate
$\dot{\gamma} = \frac{v}{h}$	$\dot{\epsilon} = \frac{\partial v_x}{\partial x}$
Shear Stress	Axial Stress
$\sigma = \eta \dot{\gamma}$	$\sigma_x = \eta_E \dot{\epsilon}$

**Table 2.3.:** Definitions of properties in shear and elongational flow.

mulated strain.

The strain is often given in terms of the Hencky Strain  $H$ , which is defined by

$$H = \ln \frac{L}{L_0} \quad (2.11)$$

where  $L_0$  is the initial length of a fluid element and  $L$  is the final length. Hencky strain is used in this work to characterize the stretching of a fluid filament in chapter 6.

A simple shear flow may be represented as a superposition of a purely rotational flow and a purely elongational flow. The following considerations are taken from [Smith et al., 1999].

In general, any planar flow of the form  $\vec{v} = v_x \vec{x} + v_y \vec{y}$  may be represented as a linear superposition of a rotational flow with a vorticity

$$\omega = \frac{1}{2} \left( \frac{\partial v_y}{\partial x} - \frac{\partial v_x}{\partial y} \right)$$

and an elongational flow with a strain rate

$$\dot{\epsilon} = \frac{1}{2} \left( \frac{\partial v_y}{\partial x} + \frac{\partial v_x}{\partial y} \right).$$

In a pure elongational flow ( $\omega = 0$ ) one expects large deformations of a polymer, whereas in a pure rotational flow ( $\dot{\epsilon} = 0$ ) one expects only rotation and no deformation.

Most practical flows consist of a mixture of both rotational and elongational components, and the resulting polymer deformation depends on the relative magnitudes of  $\dot{\epsilon}$  and  $\omega$ . In general, the response is not necessarily a linear superposition of the responses to each component. In a simple shear flow ( $v_y = 0$  and  $v_x = \dot{\gamma} y$ , where  $\dot{\gamma} = dv_x/dy$  is the shear rate) the magnitude of the elonga-

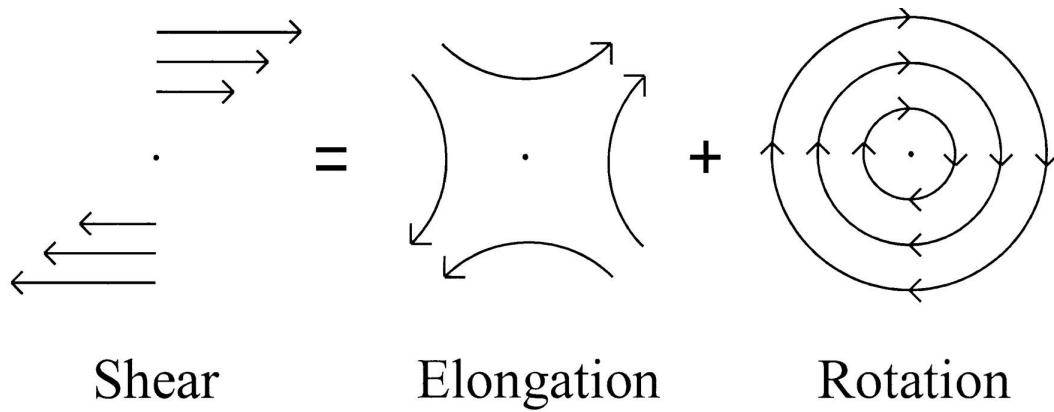


**Figure 2.8.:** A simple shear flow may be represented as a superposition of a purely rotational flow and a purely elongational flow [Smith et al., 1999].

tional and rotational components are equal ( $|\dot{\epsilon}| = |\omega|$ ).

In contrast to shear flow, where stream lines are parallel, stream lines converge in elongational flow (Figure 2.8). Consequently, the velocity gradient in elongational flow is in the direction of the flow.





## 3. Materials and Methods

### 3.1. FEM Simulation of Flow

Spider silk solutions exhibit complex fluid properties and follow non-trivial stress-strain relations. Specifically, the viscosity depends strongly on the shear rate that is dominant in a certain flow problem. Thus, spider silk solutions can be regarded as shear thinning fluids.

In this study, we attempted to mimick important aspects of spider's spinning ducts in microfluidic devices. Thus, the flow of complex fluids through geometries as designed was modelled using Finite Element Simulations.

Incompressible fluid flow is generally described by the Navier-Stokes-Equation:

$$\rho \left( \frac{\partial v}{\partial t} + v \cdot \nabla v \right) = -\nabla p + \eta \Delta v + f \quad (3.1)$$

where  $\rho$  is the density,  $v$  is the velocity of a fluid element,  $\eta$  is the viscosity,  $p$  is the pressure, and  $f$  are the body forces (such as gravity) per unit volume acting on the fluid element.

As soon as  $\eta$  is not a constant, but by itself a function of the shear rate, the system must be analyzed by coupling these differential equations, which is generally not possible analytically.

Finite Element Simulations (FEM) is a method to approximate partial differential equation (PDE) systems on a given geometry. The space on which a solution for a PDE system should be found is divided into small volumes (Figure 3.1). At the limits of the geometry, boundary conditions are defined. Then solutions for each volume element are computed and continuity is ensured. The simulations in this thesis were performed using the Comsol Multiphysics 3.5 software package (Comsol A.B., Sweden).

The simulations were done in two dimensions, which is assumed to represent a cross section in the middle of a very high channel. On the inlet side, a flow with a given inflow velocity was defined. On the exit side, a neutral boundary condition was selected. All other walls were set to the no-slip boundary condition.

The main challenge in Finite Element Simulations for finding a converging so-

### 3. Materials and Methods

lution is to find appropriate starting conditions. In the presented simulations, this was achieved by simulating in a transient (time-dependent, as opposed to static) manner, and by setting the inflow velocity (or pressure, in some cases) as to follow a relatively slow growth function. In this way, the flow starts gently and the solutions of the PDE keep converging also in higher flow speeds. Typically, the simulated time was 5 seconds, with the flow set to increase during the first second. The flow patterns that developed then were observed to be stable.

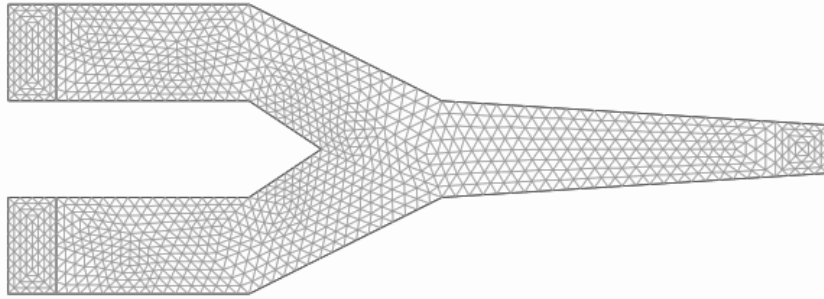


**Figure 3.1.:** Example for the mesh used for finite element simulations. For actual simulations, the mesh size was actually approximately half as large as shown here for visualization.

### 3.2. Fabrication of Microfluidic Devices

Rapid-prototyping of microfluidic devices cast of Polydimethylsiloxane (PDMS) was used [McDonald et al., 2001, McDonald and Whitesides, 2002]. Briefly, the design of the device is printed in high resolution (4000 dpi) on a transparency which is used as a mask to expose SU-8 50 positive photoresist (Microchem). After developing, the SU-8 structure serves as a master for the casting of PDMS which is poured onto the master as a liquid (see Figure 3.2). PDMS was cured for 1 hour at 70 °C.

After being removed from the master, the PDMS replica of the channels is sealed to standard microscopy coverslips after plasma oxidation of both PDMS and glass. Liquid connections were incorporated by punching holes with biopsy punchers (WPI, Berlin). To prevent excessive sticking of silk proteins to the walls of the microfluidic device, a 1% wt/vol solution of F108 block-copolymer was introduced into the channels and incubated for 1h at 60 °C ([Hellmich et al., 2005]).

### 3.3. Recombinantly produced spider silk proteins and peptides

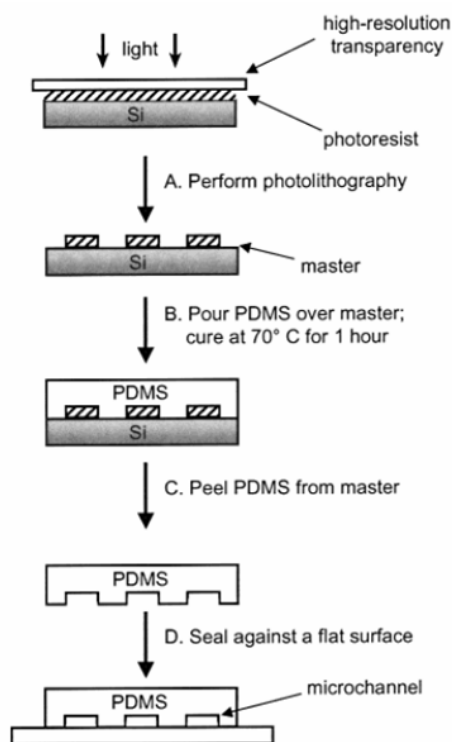


**Figure 3.2.:** Fabrication of microfluidic devices using PDMS lithography. Figure from [McDonald and Whitesides, 2002]

Before use, all channels were thoroughly rinsed with 10 mM Tris buffer, pH 8. Fluid flow during the experiments was controlled by syringe pumps (SP210iw, WPI, Berlin).

A detailed step-by-step procedure for the fabrication of microfluidic devices from PDMS can be found in Appendix B.

## 3.3. Recombinantly produced spider silk proteins and peptides

### 3.3.1. Engineered Spider Silks

In order to express engineered spider silk proteins in *E.coli*, consensus motifs for the repetitive sequences of the two silk proteins eADF3 and eADF4 were determined.

As spiders and bacteria differ quite largely in codon usage, direct expression of spider genes in bacteria leads to insufficient yields. Therefore, the codon usage was translated to the usage preferred by *E. coli*, and plasmids were produced using a seamless cloning technique [Huemmerich et al., 2004b].

### 3. Materials and Methods

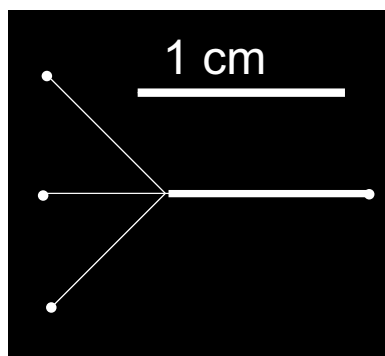


**Figure 3.3.:** An example for the lithographic masks used to produce the PDMS microfluidic devices.

Repetitive elements from the sequence of ADF3 revealed a polyalanine-rich motif (named A here) and a glutamine and glycine-rich motif (named Q), and the non repetitive carboxyterminus which was called NR. 24 repetitions of the A and Q motifs were concatenated using a seamless cloning technique [Huemerich et al., 2004b]. Thus the engineered protein eADF3 consists of the sequence (AQ)<sub>24</sub>NR, and the two terms are used synonymously.

For some studies on the stability of assemblies, also an eADF3 without NR domain, named eADF3- $\Delta$ C was used.

ADF4 revealed a repetitive sequence with more dominant polyalanine repeats, and less glycine-rich motifs. The repetitive sequence of eADF4 is referred to as C. Again, using the seamless cloning technique, 16 repeats of the C motif were concatenated. The resulting engineered spider silk protein eADF4 has the sequence C<sub>16</sub> and the two terms are used synonymously.

Protein production was performed in fermenters, with optical density at 600 nm reaching up to 40 at 9 hours after induction. The fermenter was programmed to maintain 37 °C, more than 45 % partial pressure of oxygen, and to stir at 600 rounds per minute (RPM). After 9 hours, bacteria were centrifuged down and the pellet washed with Tris pH8 for 3 times. Then the pellet of bacteria was frozen overnight.

The next day, bacteria were thawed slowly at room temperature and incubated with 0.2 mg/mL lysozyme on ice. Lysozyme treatment was finished when the suspension turned mucilaginous (slimy)<sup>1</sup>. To breakup DNA fragments, 6 cycles of 3 times 15 seconds sonication each were performed. After centrifugation at 20,000 RPM for 30 minutes, the supernatant was exposed to a heat treatment at

<sup>1</sup>Interestingly, the slimy behaviour of the lysed cells is partially due to the elongational viscosity of the large amounts of DNA present in the suspension.

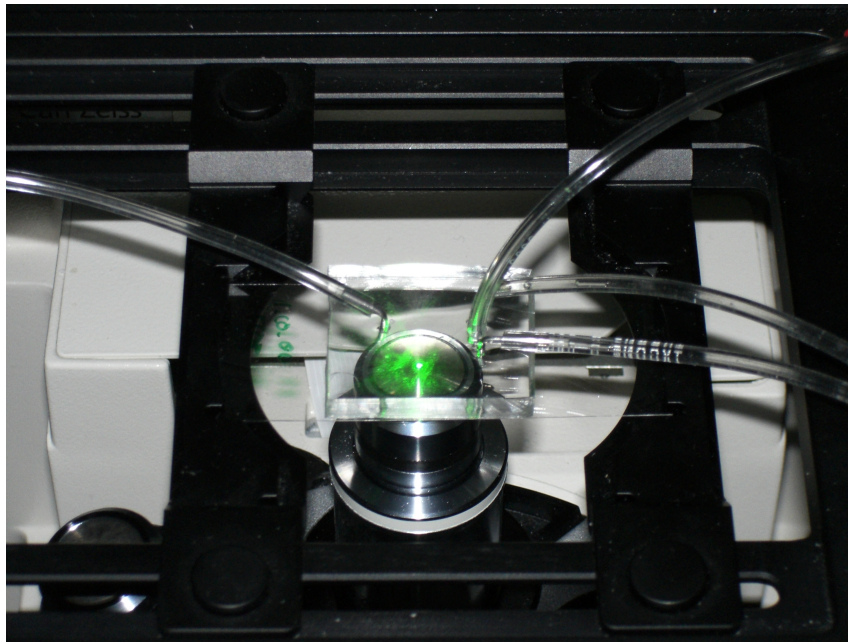


**Figure 3.4.:** Assembled Microfluidic Spinning Duct on the microscope stage.

80 °C for 25 minutes, before cooling down on ice.

After another centrifugation step (30 minutes, 20,000 RPM), the supernatant was treated with 20 % ammonium sulfate to precipitate silk proteins. The precipitates were centrifuged down for 20 minutes at 6000 RPM. A typical preparation was then dissolved again in 15 ml of 6 M guanidinium thiocyanate (GuaSCN). For storage, the latter solution was dissolved 3 times for 3 hours minimum in 10 mM Tris pH 8 buffer, before lyophilisation over night.

After purification, the purity was checked by UV-VIS spectrophotometry (to determine DNA contamination) and by silver-stain SDS-PAGE (to determine possible protein degradation by proteases). Silver stain had to be used as silk proteins are not stained by Coomassie.

### **Amphiphilic Properties**

The repetitive units of silk proteins show highly amphiphilic properties. This means that parts of the sequence are distinctly hydrophilic, and others hydrophobic. One can assign a measure of the strength of the hydrophobicity to each type of amino acid, and then plot this hydrophobicity index of the sequence [Gasteiger et al., 2005]. In figure 3.5, hydrophobicity indices for one repetitive unit of eADF3 and eADF4 are plotted.

### 3. Materials and Methods

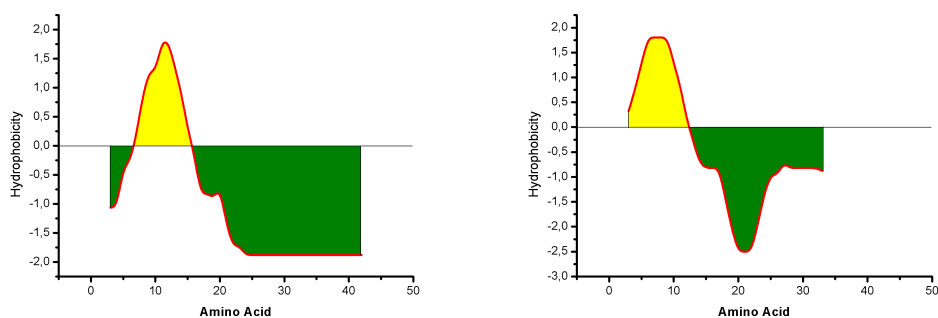


**Figure 3.5.:** Hydrophobicity Plots of the repetitive motifs of the two engineered spider silk proteins. Left: one AQ sequence. Right: one C sequence.

#### 3.3.2. Fragments of engineered spider silk proteins



In addition to the full engineered spider silk proteins, a variety of fragments, typically representing the repetitive units, were created. These are intended to elucidate the contributions from repetitive motifs with different characteristics, such as hydrophobicity and the propensity to form beta-sheets. It must be kept in mind that the influence of the NR domains, which play an important role in the assembly process, are not present in the aggregation process of these short fragments.

Sequence	Origin	Mass (kDa)
AAAAAASGYGPEN	C	1.1
GSSAAAAAAG	C	1.0
GPGGP	C	0.42
GPQGP	C	0.41

**Table 3.1.:** Synthesized fragments of engineered spider silk.

The fragments listed in table 3.1 were purchased from ThermoElectron Corporation (Ulm, Germany) and dissolved in Guanidinium-Thiocyanate and dialyzed to aqueous buffers, or were dissolved in HFIP directly, depending on the experiment.

Proteins were produced and purified as described previously and lyophilized. Next, lyophilized proteins were dissolved in 6 M Guanidinium-Thiocyanate and dialyzed into 10 mM Trishydroxymethylaminomethane (Tris) buffer, titrated to pH 8 with HCl. Protein concentrations were measured by absorption at 280 nm in a ND-1000 spectrophotometer (Nanodrop) using the calculated extinction coefficients of 73950 M<sup>-1</sup>cm<sup>-1</sup> for eADF3 and 46400 M<sup>-1</sup>cm<sup>-1</sup> for eADF4. Potassium phosphate buffers were prepared at 300 mM and 500 mM at pH 8 or 6 [Scheibel, 2005b].

native proteins	elements of the original sequence	synthetic sequence
ADF-3	<p>GPYGP GASAAAAAA GGYGP GSGQQ module A</p> <p>GPGQQ GPGQQ GPGQQ GPGQQ module Q</p> <p>non-repetitive region module NR3</p>	 <p>eADF3</p>
ADF-4	<p>GSSAAAAAAA SGP GGQGP EN QGPSGP GQ GPGGP module C</p>	 <p>eADF4</p>

**Figure 3.6.:** Overview on consensus motifs in *Araneus Diadematus* Fibroin (ADF) proteins, used in the engineered spider silk proteins. Synthetic sequences mimic natural ones and are composed by repeating these oligopeptide motifs. eADF3 is composed of 24 repeats of the A and Q motif, followed by the non repetitive region NR3. eADF4 is composed of 16 repeats of the C motif. Molecular weights are 106 kDa for eADF3 and 48 kDa for eADF4.

### 3.3.3. Solvents

In general, engineered spider silk proteins were dissolved in GuaSCN and dialyzed into Tris pH 8 or other aqueous solutions.

For experiments that required a high concentration of eADF4 and derived proteins, Hexafluoro-isopropanol (HFIP), which exhibits strong hydrogen bonding properties enabling it to dissolve substances that serve as hydrogen-bond acceptors, such as amides and ethers, was used as a solvent. C16 is soluble in excess of 200 mg/ml in HFIP.

## 3.4. Protein Analysis

### 3.4.1. UV Spectroscopy

Using the Lambert-Beer relation one can calculate the concentration  $c$  of a protein with absorption  $E_\lambda$ , molar extinction coefficient  $\epsilon_\lambda$  and layer thickness  $d$ :

$$c = E_\lambda / (\epsilon_\lambda d).$$

Absorbances at 276 nm that were used [Huemmerich et al., 2004b, Huemmerich et al., 2004c]:

### 3. Materials and Methods

Protein	$M_w$ (kDa)	$\epsilon_{276}$ ( $M^{-1}cm^{-1}$ )
C16 (eADF4)	47.7	46400
AQ24NR3 (eADF3)	106.3	73950

**Table 3.2.:** Absorbances of engineered Spider silk proteins.

#### 3.4.2. Infrared Spectroscopy

By infrared spectroscopy it is possible to analyze the relative vibrations of individual atoms in a molecule. For protein analysis, C=O stretching vibrations in the peptide bonds are of special interest, as their energy eigenvalues depend on how much the protein backbone is bent. This allows to determine in which secondary structure the protein is [Winter and Noll, 1998].

Depending on secondary structure, the frequency of the Amide I-vibration shifts. Depending on the shape of the Amide I band, relative secondary structure contributions can be calculated.

The following secondary structure features are assigned to wavenumber bands [Winter and Noll, 1998, Byler and Susi, 1986]:

Wavenumber $\nu$ in $cm^{-1}$	Assignment
1620-1640	$\beta$ -sheet
1640-1650	random coil
1650-1658	$\alpha$ -helical
1660-1690	turns
1670-1680	$\beta$ -sheet

Infrared spectra were taken between 7000 and 1000  $cm^{-1}$  using a Bruker IFS66/s spectrometer connected to a Bruker IRscope II infrared microscope with a 36x objective.

Dried samples were placed on  $CaF_2$  slides. Spots not covered with protein were used for background measurements. Fibers were localized and then a suiting aperture was chosen, in order to measure only spectra of fibrous assemblies. Secondary structure elements were assigned by fitting gauss peaks to the absorbance spectra in the range between 1580  $cm^{-1}$  and 1700  $cm^{-1}$ .

A baseline was subtracted from the spectra and a set of Gaussian peaks was fit to the absorption curve. Data analysis was performed using the PeakFit routine of the Origin Software (Origin Lab Corp.).



### 3.5. Scanning Electron Microscopy

Spider silk assemblies usually exhibit a three-dimensional structure, on lengthscales of around  $1\ \mu\text{m}$ . For instance, typical diameters for dragline silk threads are in the  $\mu\text{m}$  range.

Therefore, Scanning Electron Microscopy is a valuable tool to investigate the morphology of the assemblies without further labelling or staining.

For Scanning Electron Microscopy, samples were dried and washed on aluminium pieces. Good results were obtained after washing three times with Millipore water.

Samples were then sputtered for one minute, in order to create a continuous gold layer on the surface of the sample. Silver contact glue was used to ensure electrical conductivity from the gold layer to the sample holder.

Digital SEM images were then obtained using a JEOL instrument.

### 3.6. Rheometry

Spider silk solutions are polymeric solutions, which exhibit a complex strain-stress relation, which makes it difficult to predict fluid properties. To understand and analyze dynamic experiments, such as the assembly in the microfluidic devices or in free surface flow, it is necessary to carefully obtain rheological data on the specific spider silk solutions used for the experiments.

Rheological measurements can lead to important insights into the polymer relaxation times for complex liquids like spider silk solutions, and can help to judge whether the polymers are present in a stretched or randomly coiled conformation at a given time in the experiment. In this thesis, it is important to distinguish the two principally different rheological methods employed:

- Shear Rheometry is applied to determine mostly the inter-molecular interactions due to electrostatic forces and due to molecular entanglement [Bird et al., 1987].
- Elongational Rheometry is more sensitive to stretching effects of single polymer molecules. As purely elongational flow is shear-free, intermolecular effects are less prominent [Schroeder et al., 2003].

### 3. Materials and Methods

#### 3.6.1. Shear Viscosimetry

Rheological characterization of engineered spider silk solutions was performed on either a Physica MCR 301 rheometer (Anton Paar, Germany) or an AR-G2 rheometer (TA Instruments). The measurement geometry was a 25 mm cone-and-plate with a sample volume of 160  $\mu\text{l}$ . Temperature of the lower rheometer plate was set to 21° C. A solvent trap was placed over the measurement gap in order to avoid drying of the sample.

#### 3.6.2. Elongational Viscosimetry

##### Introduction to Elongational Viscosimetry

As Elongational Viscosity is a less commonly tested property of fluids than shear rheology, a few general remarks on measurement methods in this field may be helpful.

In general, two techniques have been mostly investigated during the last years to study elongational flow in polymer solutions:

- Opposing Jets
- Capillary Breakup Extensional Viskosimetry

##### Opposing Jets

In this technique, opposing jets of liquid are shot against each other, resulting in a biaxial elongational flow. An opposed jet rheometer for studying low viscosity non-Newtonian fluids has been used to measure the properties of various aqueous solutions [Fuller et al., 1987]. Large deformation rates (typically greater than 1000  $\text{s}^{-1}$ ) are required to induce significant viscoelastic effects, and at such rates inertial stresses in the fluid can completely mask the viscoelastic stresses resulting from molecular deformation and lead to erroneous results [Dontula et al., 1997]. Analysis of jet break-up and drop pinchoff have also been proposed as a means of studying the transient extensional viscosity of dilute polymer solutions. After the formation of a neck in the jet or in the thin ligament connecting a falling drop to the nozzle, the dynamics of the local necking processes in these geometries are very similar to that in a capillary break-up rheometer. However, the location of the neck or 'pinchpoint' is spatially-varying, which turns subsequent analysis of the pinch-off dynamics more difficult.

For macromolecules, a microfluidic opposing jet setup was developed, which allowed to trap for instance a DNA molecule in the center of the biaxial elongational flow [Babcock et al., 2003, Chu et al., 1995]. This allowed to directly observe the relaxation dynamics of single, fluorescently labelled DNA molecules [Perkins et al., 1994].

### Capillary Breakup Extensional Viskosimetry (CABER)

In this technique, a liquid bridge of the test fluid is formed between two cylindrical test fixtures as indicated schematically in Figure 3.8. An axial step-strain is then applied which results in the formation of an elongated liquid thread. The profile of the thread subsequently evolves under the action of capillary pressure and the necking of the liquid filament is resisted by the combined action of viscous and elastic stresses in the thread.

The advantages of this method are:

- Only low sample volumes are needed (down to  $\approx 10 \mu\text{l}$ ).
- As the mid-point fluid filament is spatially stationary, image analysis to elucidate the dynamics is relatively uncomplicated.
- Low deformation rates can be achieved which allows measurements on relatively low elasticity samples.

One drawback of the CABER method is, that meaningful data can generally only be obtained on fluids which show a shear viscosity of more than approximately 70 mPas and typical polymer relaxation times of more than 1 ms (Figure 3.7). For less viscous fluids, or polymers with faster relaxation times, surface tension dominates the breakup and all experiments on those fluids will yield indistinguishable results (mainly defined by the experimental setup), without allowing insights into fluid dynamics.

#### 3.6.3. Apparent Elongational Viscosity in CABER

The force balance for the fluid between the two plates in a CABER experiment is

$$\underbrace{3\eta_s \left( -\frac{2}{D_m} \frac{dD_m}{dt} \right)}_{\text{Viscous Stress}} = 3\eta_s \dot{\epsilon} = \underbrace{\frac{4F_z}{\pi D_m^2}}_{\text{Tensile Stress}} - \underbrace{[\tau_{zz} - \tau_{rr}]}_{\text{Elastic Non-Newtonian Stress}} - \underbrace{\frac{2\sigma}{D_m}}_{\text{Capillary Pressure}} \quad (3.2)$$

### 3. Materials and Methods

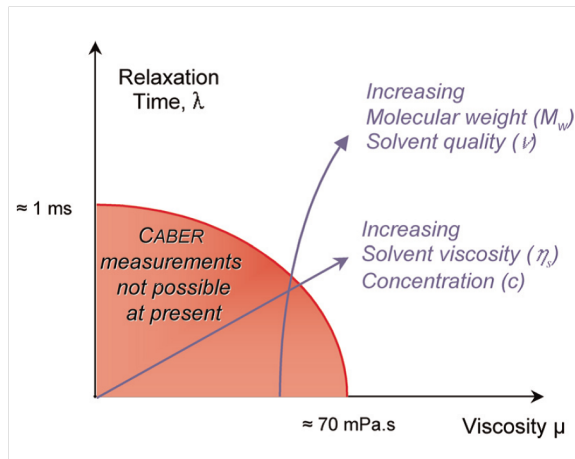


**Figure 3.7.:** Capillary Breakup Extensional Rheology (CABER) is a valuable tool for fluids that have a larger viscosity than about 70 mPas and a polymer relaxation time of more than about 1 ms.

where  $z$  is the axial direction and  $r$  indicates radial directions of the stress tensor  $\tau$ ,  $\eta_S$  is the shear viscosity,  $F_z$  is the force in the axial direction,  $\dot{\epsilon}$  is the elongation rate,  $\sigma$  is the surface tension and  $D_m$  is the mid-point diameter [Doyle et al., 1998, Rodd et al., 2005]. For actual measurements, it is not directly possible to measure the tensile stress because this is an internal stress in the fluid and there is no rigid connection to the plates. Thus, a force sensor connected to either of the plates will not record the stress  $[\tau_{zz} - \tau_{rr}]$ , but only the fraction of this stress that is transported by visous drag. Furthermore, it would be extremely difficult to extract the elastic stresses that may occur from the relatively large effect of down-pouring fluid, which leads to a smaller measured weight.

One strategy to circumfere the determination of the tensile stress is the analysis of a quantity that is referred to as the *apparent elongational viscosity*:

$$\eta_{app} = -\frac{d D_m(t)}{dt} \frac{1}{\sigma}$$

where  $D_m$  is the mid-filament diameter and  $\sigma$  is the surface tension. This relation gives a qualitative measure of the resistance to flow by elongational viscosity effects, and is a useful parameter for comparison of different fluids. For elastic fluids, such as polymer solutions, it is often found that  $\eta_{app}$  is a function of strain.

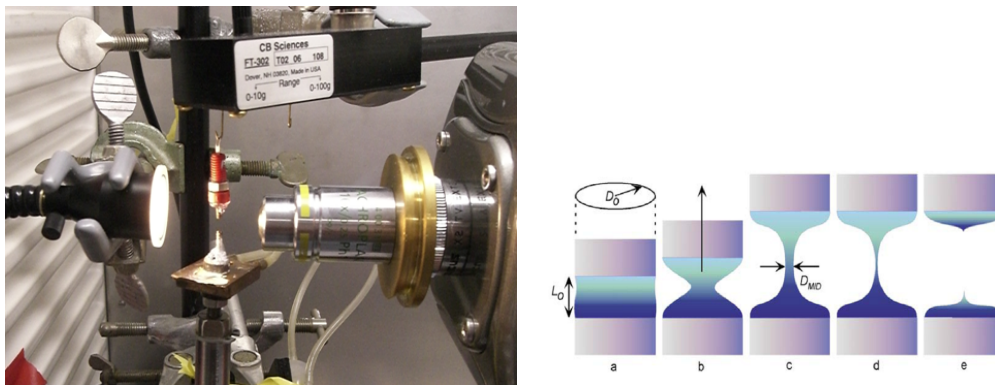


**Figure 3.8.:** Left: Elongational Viscosimetry Setup. The sample is placed on the holder in the center of the image, which is connected to a linear motor that moves the stage up and down. Light is coming from the left and the fluid filament diameter is monitored by the high-speed camera on the right. Right: Sketch of the anticipated time course of the mid diameter of a fluid with non-vanishing extensional viscosity [Corporation, 2003].



**Figure 3.9.:** Image processing for Fluid Filament diameter determination: Left, original image. Middle: After Black-white conversion. Right: After background subtraction (later in the movie).

### 3.6.4. Experimental Setup for CABER

#### Linear Motor

In capillary breakup experiments, the only motion required is the initial increase in gap size. This can be best realized using a linear motor (See picture 3.8). In this setup, a Linmot PS01-23x80 motor (Linmot AG, Switzerland) was used, which allows to achieve the displacements required for CABER measurements typically in less than  $50 \mu s$ .

The motor is controlled by a Linmot B1100 controller (Linmot) and connected to the control computer via RS-232. The B1100 controller was running the EasySteps program in it's firmware, which allows to predefine a set of commands and then

### 3. Materials and Methods

execute these commands by electric triggers directly wired to the B1100 controller. These triggers are generated by a Labview program. Since the B1100 requires  $\pm 20$  V signals, an external relais board (USBREL8, Quancom Informationssysteme GmbH) connected to a laboratory power source was used.

#### 3.6.5. High-speed imaging

Filament breakup usually takes place in less than a second. In order to monitor the time course of the filament diameter with sufficient precision in time, a high speed camera is required. In this setup, a Phantom V5.1 (Vision Research) camera was used, which is able to capture more than 1000 frames per second (fps) at 1024x1024 pixels, or 4000 fps at 384x786 pixels. The fluid filament was illuminated from the backside by an optical fiber which was illuminated by a 300 W halogen light source (Schott KL2500 LCD).

#### 3.6.6. Elongational Viscosimetry Data Analysis

During the filament breakup experiment, a grayscale movie is recorded with a highspeed camera. The frames of this movie are then analyzed in a software written in MATLAB to determine the diameter of the fluid filament in each frame. In the program, the following algorithm is used to reliably detect filament diameters (Figure 3.9):

1. One Frame from the end of the movie is selected as a background.
2. This background image is then subtracted from all preceding frames. By this means, most of the background noise and eventual dirt in the optics can already be eliminated.
3. The frames are converted to binary black and white images, with a threshold that is selected manually before the start of the procedure to maximize the contrast.
4. Manually, a region in the frames is selected in which to search for the filament. This is done by defining the position of cut-off lines on the left and on the right of the filament.
5. The actual thickness of the filament is determined by looking for the first change in pixel value from the left, and subsequently, the first change in pixel value from the right. In this way, filaments that appear darker in the middle will also be detected reliably.

6. The program then calculates values for the filament diameter in millimeters as well as the Hencky Strain  $H = \ln D(t)/D_0$ , based on the dimensions entered into the program before starting the analysis.

### 3.6.7. Sample system: Polyacrylamide solutions

To test the elongational rheometer, samples made of aqueous solutions of 5 MDa Polyacrylamide (PAA) with varying concentrations of glycerol to change the shear viscosity were tested. This system has been thoroughly investigated and elongational viscosity data has been assessed [Edmond et al., 2006]. Also, at high flow rates, 1% aqueous solutions are known to form jets that are 4-90  $\mu\text{m}$  in diameter and several centimeters long, which are stable to break-up into droplets even in a nonpolar solvent. This makes the behaviour of this kind of polymer interesting for the understanding of silk fiber formation in air.

The filament rupture times of PAA solutions of varying concentrations are plotted in figure 3.10. It can be clearly seen that there is an exponential relationship between the filament breakup time and the shear viscosity.

The time course of the filament breakup in Figure 3.10 leads to apparent elongational viscosities as plotted in Figure 3.6.7. It can be seen that the delayed filament breakup for the more concentrated solution results in a higher apparent elongational viscosity.

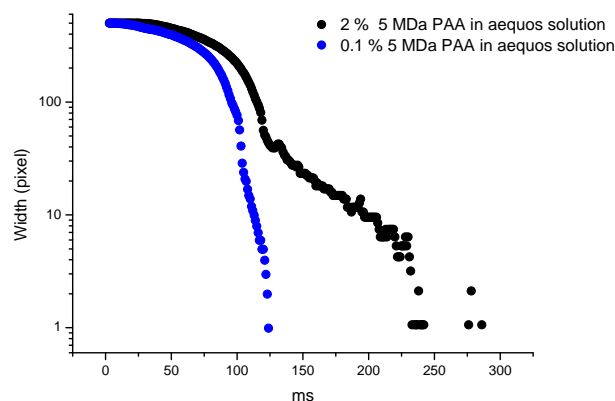


**Figure 3.10.:** Filament Breakup of PAA solutions at varying concentration.

When the solvent viscosity  $\eta_s$  is varied, by adding varying amounts of glycerol, a drastic increase in filament breakup time can be observed (Figure 3.6.7). In the

### 3. Materials and Methods

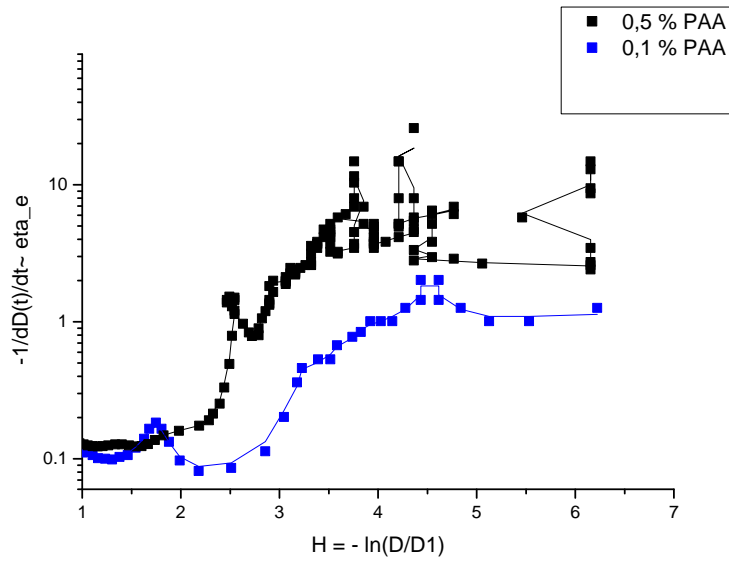


**Figure 3.11.:** Elongational Viscosity for 0.1% and 0.5 % 5 MDa Polyacrylamide solutions.

Rouse model, the longest polymer relaxation mode is

$$t_r \propto \eta_S$$

and therefore, the exponent with which the filament rupture time changes over solvent viscosity, enables one to determine the polymer relaxation times [Rubinstein and Colby, 2003].

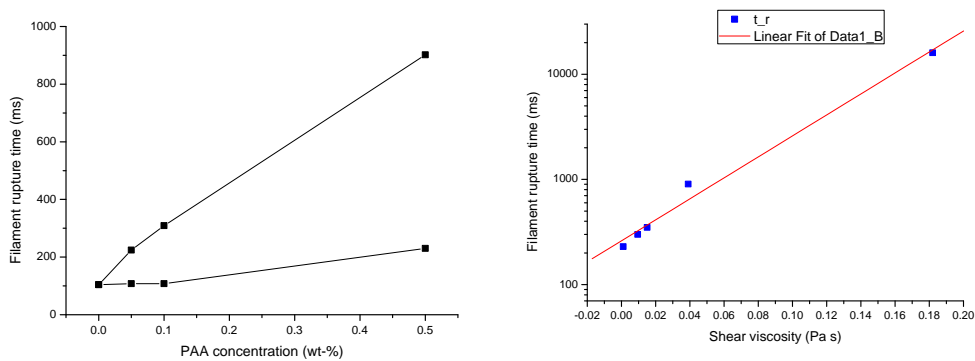


**Figure 3.12.:** Filament rupture times over Polyacrylamide (PAA) concentration and over the corresponding shear viscosity.



## 3.7. Fiber Tester Setup

### 3.7.1. Linearity of Motor

For tensile tests of elastic fibers, it is of great importance to ensure linear movement of clamps, between which the fiber is held. Linearity of the motor movement was tested using a capacitive displacement sensor (WPI, Berlin). The motor was found to operate linearly for the whole range of displacement accessible (Figure 3.13).

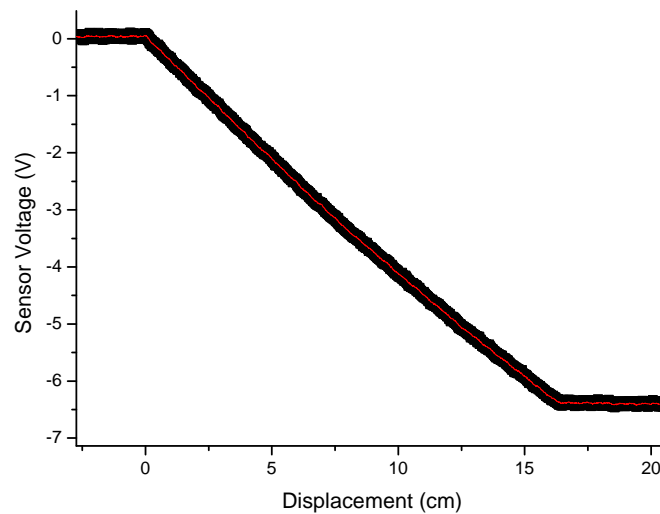


**Figure 3.13.:** A capacitive distance sensor was used to check the linearity of the Linear Motor driving the fiber tester setup.

### 3.7.2. Climatized Chamber

Mechanical properties of silk fibers depend highly on the relative humidity [Vehoff et al., 2007]. For this reason, fiber testing experiments were done in a climatized chamber (Lintek GmbH). This chamber provides both temperature and humidity control. Since the climate chamber itself is optimized to maintain a certain level of humidity over rather long times, it's control cycles are adjusted to react very slowly (Figure 3.14). In order to achieve large increases of relative humidity in short times, an additional electronically controlled room humidifier was placed in the chamber and used when necessary.

### 3. Materials and Methods

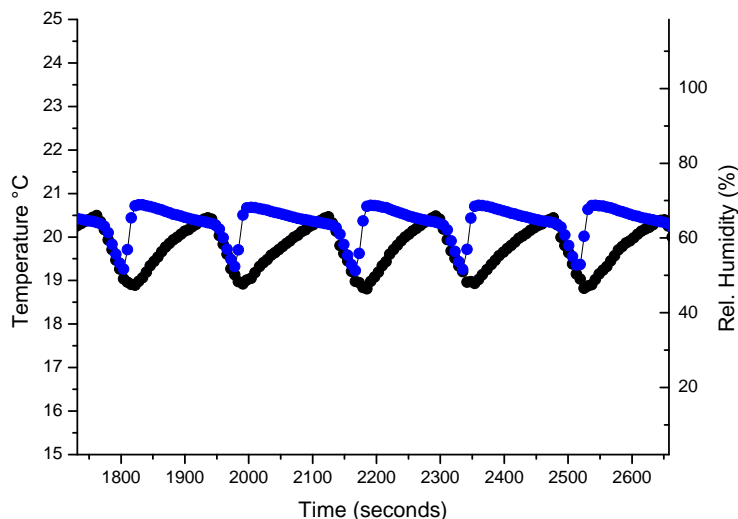


**Figure 3.14.:** For silk fiber testing experiments, a controlled humidity and temperature environment is necessary.

#### 3.7.3. Force Sensor

The force sensor (FT-302, CB Sciences) used in this setup works by measuring small deflections of a cantilever by optical methods. In detail, this means that the measurement cantilever is illuminated by an LED light source, and the total intensity that is collected in the photosensor is measured. For small cantilever deflections, a linear relation between the deflection of the cantilever and the signal in the photosensor is reported by the manufacturer. The force sensor was calibrated by pipetting known volumes of Millipore Water into a vial hanging from the sensor (Figure 3.15). The calibration shows that the sensor is perfectly linear in the range used for these experiments. The fiber testing apparatus is controlled by the software provided by the manufacturer of the linear motor and by a custom-built LabView program which triggers the motor and records force sensor data to the hard disk of the computer.

#### 3.7.4. Sample preparation for fiber testing

In order to place thin and fragile fibers reliably in the fiber testing device, 2-3 cm long pieces of fibers were glued to paper frames (Figure 3.16). These frames were then mounted in the testing setup, and the paper frame was cut. After the humidity and temperature reached the set levels, fiber testing was performed.

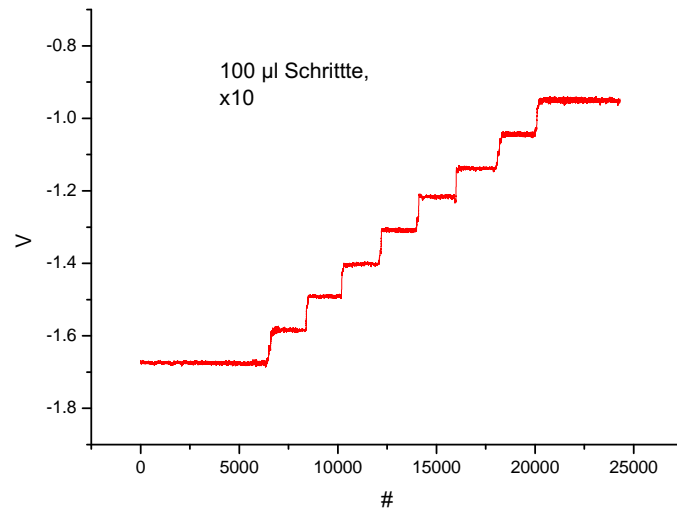


**Figure 3.15.:** Force calibration of the FT10-100 sensor, in 10x amplification setting.

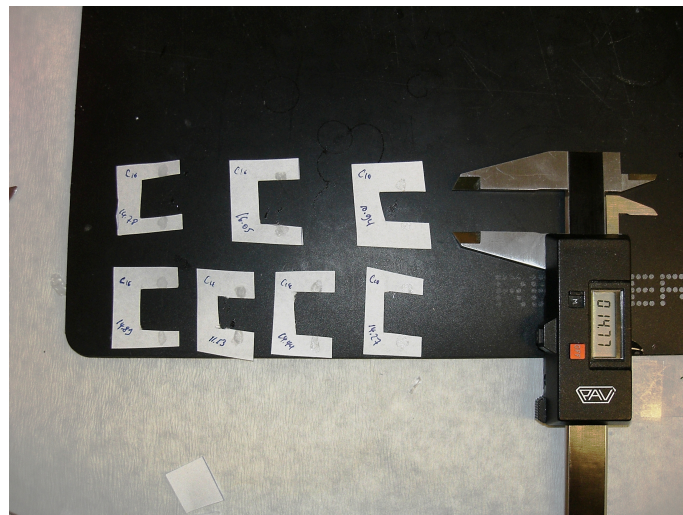


**Figure 3.16.:** Fiber fragments were glued to paper frames for placement in the fiber tester.



## 4. Shear induced aggregation: First insights into silk assembly

Spiders form fibers in a spinning duct, where the silk protein is subject to the addition of phosphate and is exposed to forces arising from the flow through the duct (see chapter 2). Thus, it is very important to know how engineered silk proteins react to the simultaneous addition of ions, as potassium phosphate, and shear forces.

### 4.1. Shear-activated aggregation of eADF3 with phosphate

In a first very simple experiment, droplets of the engineered spider silk eADF3 with varying concentrations of phosphate were placed on microscope slides and a cover slip was put on top of it. The resulting liquid film was sheared by hand lightly in one direction. It was carefully avoided to shear the cover slip back and forth in this stage.

The result of this simple but instructive experiment can be seen in figure 4.1. For low phosphate concentrations, no spherical aggregates form, and no visible alteration of the liquid is taking place upon shearing. In the case of 400  $\mu\text{M}$  phosphate, spherical aggregates are visible just after placing the cover slip on the drop of liquid, before shearing. After shearing, large clusters of aggregated material are visible. Interestingly, after experiments where the cover slip was moved only a little in one direction, oriented aggregates are observed (second row of figure 4.1). After shearing back and forth and in a circular fashion, the aggregates are not oriented any more, but collapsed to more or less spherical aggregates (lower row of figure 4.1).

Interestingly, in the case of 100  $\mu\text{M}$  phosphate, the protein appears to remain in solution and not aggregate into spherical aggregates before shear, but large clusters are visible after shearing. It seems possible, that the addition of salt destabilizes the solution, and additional shear would then cause the protein to precipitate. Similar effects have been observed for silk fibroin solutions from reconstituted *Bombyx Mori* cocoons [Matsumoto et al., 2008].

When the second engineered silk protein (eADF4) was treated with the same

#### 4. Shear induced aggregation: First insights into silk assembly

experimental conditions, a similar formation of spherical aggregates could be observed [Slotta et al., 2008]. However, there is an important difference in response to shear forces: spheres from eADF4 could not be forced into larger aggregates by shearing the cover slip. Thus, eADF4 spheres remained inert to shear forces between the cover slip and the microscope slide.

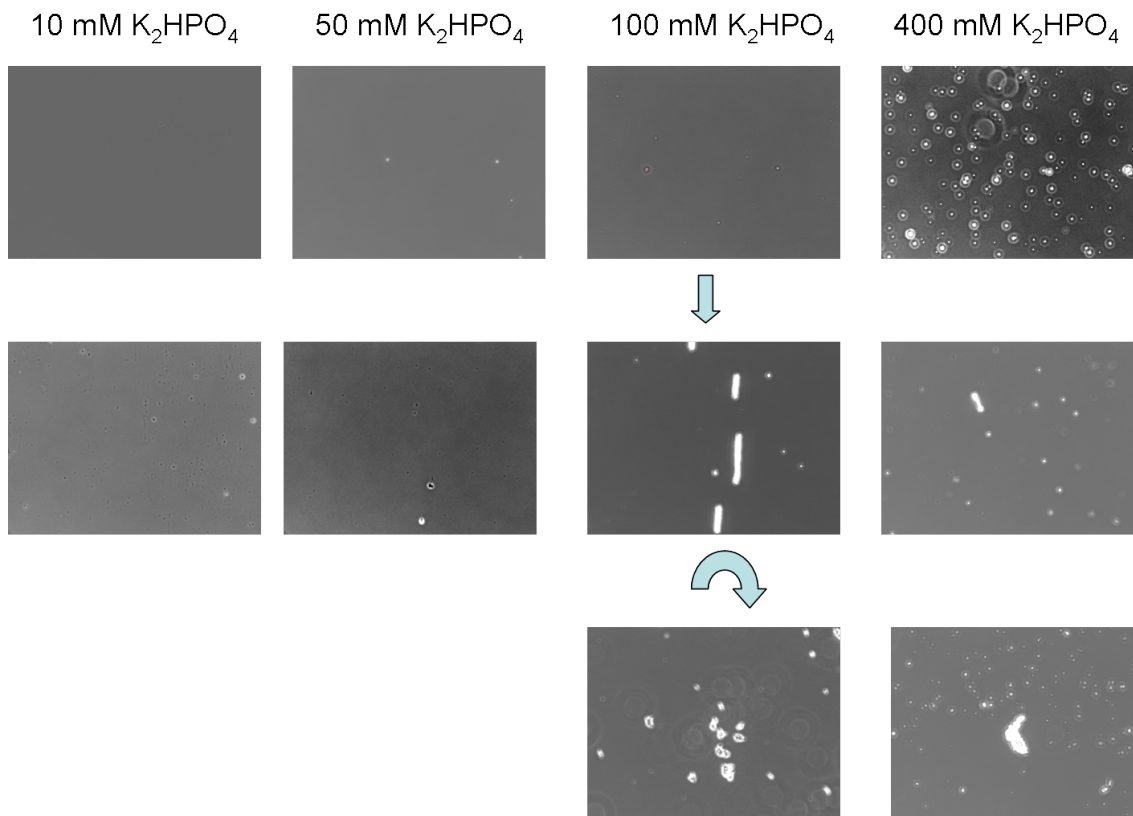


**Figure 4.1.:** Shear induced aggregation of AQ24 spherical aggregates (phase contrast microscopy). In the top row of images, one can see that with 400 mM of phosphate, spherical particles are formed. If the cover slide is sheared unidirectionally over the liquid layer, larger aggregates are formed (Second row). The shearing effect is most visible in the case of 100 mM salt, where oriented aggregates are visible.

In order to elucidate this effect, the poorly defined experiment on the microscope slide was repeated and extended in a shear rheometer. The rheometer allows to carefully control both the strain and the stress exerted on the silk protein solution. The results of these experiments are described in the following two sections.

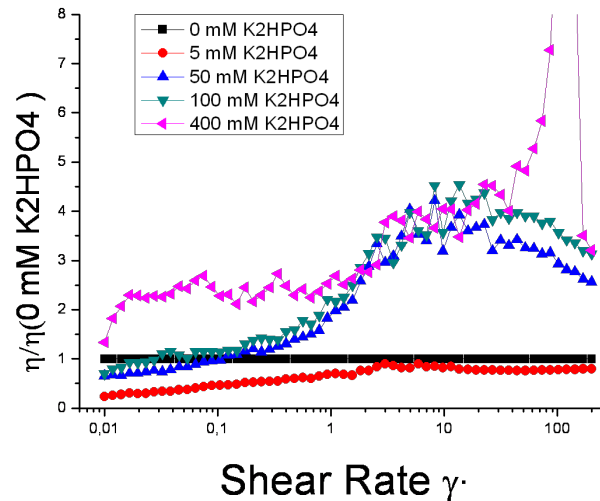


**Figure 4.2.:** The effect observed in figure 4.1 assessed more quantitatively in the rheometer. Addition of phosphate induced shear dependent effects in eADF3 solution. In this plot, the viscosity is normalized to the viscosity of eADF3 without phosphate.

## 4.2. Shear Ramps

When a similar experiment as the one with protein solution between the glass slide and the cover slip is performed in a rheometer, shear activated processes can be quantified.

Shear induced aggregation appears very drastically when the viscosity is plotted normalized to the viscosity of the eADF3 solution with no phosphate present. As can be seen in figure 4.2, addition of low phosphate concentrations (5  $\mu\text{M}$ ) slightly decreases the shear viscosity in the low shear rate regime, compared to a solution of eADF3 without phosphate. After addition of more than 50  $\mu\text{M}$  of phosphate, the viscosity is increased, especially in the high shear rate regime. When 400  $\mu\text{M}$  of phosphate are present in the sheared solution, the viscosity-shear rate curve becomes non-monotone and increases at a shear rate of approximately  $100 \text{ s}^{-1}$ .

## 4.3. Shear Hold

In this series of experiments, the samples were exposed to constant shear rates for several minutes. Again, like in the experiment between the glass slides, a drastic difference in the behavior of eADF3 and eADF4 was found: While suspensions of spherical aggregates of eADF4 flowed undisturbedly under shear rates of 80

#### 4. Shear induced aggregation: First insights into silk assembly

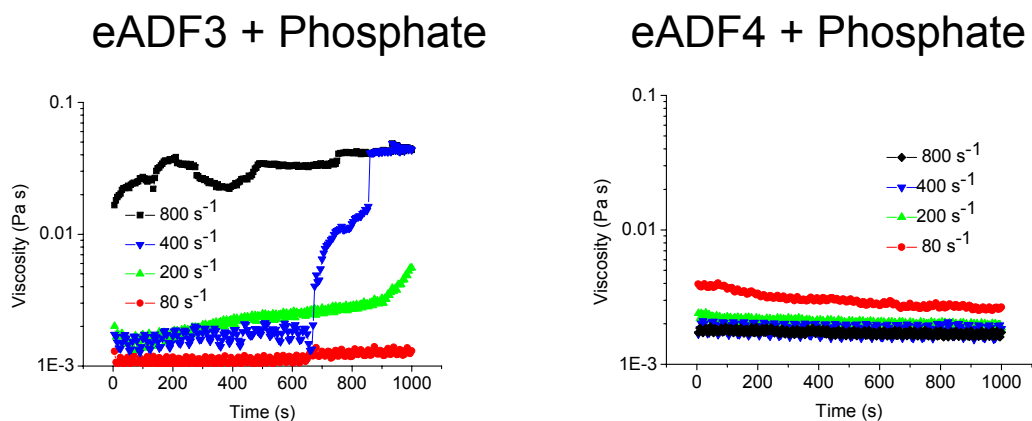


**Figure 4.3.:** Left: A suspension of eADF3 (10 mg/ml) preformed colloidal aggregates is subjected to different shear rates in a cone-and-plate rheometer. For low shear rates, no significant increase in the viscosity is recorded for up to 1000 seconds. At high shear rates, an increase in the apparent viscosity indicates shear-induced aggregation of eADF3 solutions in the presence of 500 mM K<sub>2</sub>HPO<sub>4</sub>. The effect gets stronger with increasing shear rates. Right: No effect of shearing is observed for eADF4 (10 mg/ml) in 500 mM K<sub>2</sub>HPO<sub>4</sub>

s<sup>-1</sup> to 800 s<sup>-1</sup>, suspensions of eADF3 spheres revealed the formation of larger aggregates under identical conditions, as indicated by the irreversible increase of the measured viscosity. Further, aggregation of eADF3 was observed to occur faster with increasing shear rate (Figure 4.3). The resulting induction times  $t_c$  are shown over shear rate in figure 4.4.

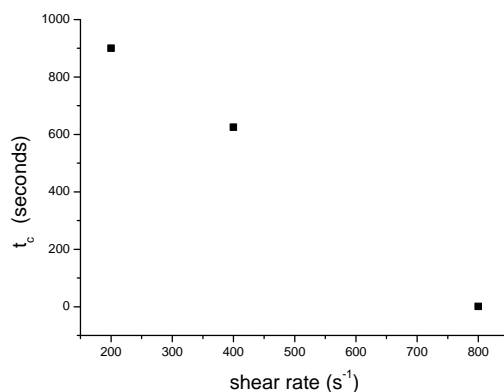


**Figure 4.4.:** Induction time for shear activated aggregation.

This experiment was also carried out with eADF4 and phosphate. Again, no effect of shearing is observed for eADF4 (10 mg/ml) in phosphate concentrations up to 500 mM K<sub>2</sub>HPO<sub>4</sub> (Figure 4.3, left).



#### 4.4. Discussion of the shear activated aggregation

The shear activated aggregation observed on spherical silk assemblies of eADF3 is qualitatively similar to the irreversible shear activated aggregation described earlier [Guery et al., 2006]. As in their work, a shear rate dependent induction time  $t_c$  was found and a sharp increase in the measured viscosity was also observed. These similarities to the results by [Guery et al., 2006] hold only for the eADF3 spherical assemblies. eADF4 particles were found to be inert to shear forces. Thus, an understanding of this aberrant aggregation behaviour must take into account the properties of the single polymer strands, and their amino acid sequences.

One model for shear activated aggregation and shear-thickening flow behaviour that takes into account molecular properties was developed for 'associative polymers' [Tripathi et al., 2006]. They consider condensed polymers, which bury most of their hydrophobic parts in condensed particles, but with some of the ends of the polymers dangling out of the condensed phases, driven by thermal fluctuations. These dangling ends have a certain rate of meeting another condensed particle, and thus cause aggregation.

On the left hand side of figure 4.5, one can see that for the polymer [Tripathi et al., 2006] studied in their work, the onset of shear thickening is between 10 and 20 kg/m<sup>3</sup> (= mg/ml), and that shear thickening effects start to become effective at shear rates around 10 s<sup>-1</sup>. On the right hand side, a schematic representation of the 'dangling ends' model: Polymer strands diffuse from one aggregate to another with a certain rate, which is related to the free energy difference of the bound (to one of the spherical particles) and unbound states.

These results are quite similar to those obtained on the eADF3 protein. One can conclude that eADF3 spherical assemblies seem to be less tightly packed than eADF4 spherical assemblies. This enables shear activated aggregation for eADF3 particles, while eADF4 particles remain inert and do not show enhanced aggregation under shear flow.

Fundamentally, the differing aggregation behaviour of eADF3 and eADF4 suspensions is created by the differences in the amino acid sequence. As can be seen in the hydrophobicity plots (Figure 3.5), the C motif has relatively fewer contributions with negative hydrophobicity index, which means it is overall less soluble. Thus, the C motif repeat sequences tend to show a larger response to the increased hydrophobic effect (by addition of phosphate) than the AQ repeat sequences. This could explain the fact that the C16 (eADF4) particles appear to

#### 4. Shear induced aggregation: First insights into silk assembly

have much less 'dangling ends' sticking out and do not show shear thickening behaviour nor shear activated aggregation.

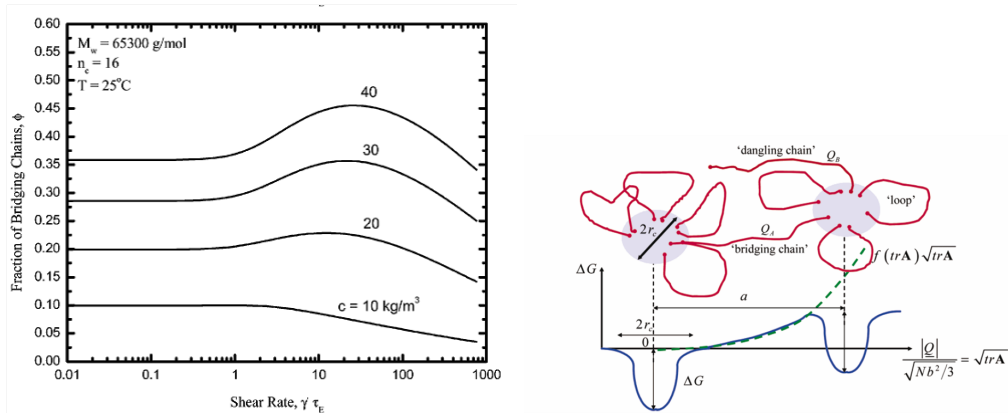


**Figure 4.5.:** Dangling ends (figures taken from [Tripathi et al., 2006]). On the left hand side, one can see that for the polymer studied in their work, the onset of shear thickening is between 10 and 20 kg/m<sup>3</sup> (= mg/ml), and that shear thickening effects start to become effective at shear rates around 10 s<sup>-1</sup>. On the right hand side, a schematic representation of the 'dangling ends' model: Polymer strands diffuse from one aggregate to another with a certain rate, which is related to the free energy difference of the bound (to one of the spherical particles) and unbound states.

In this chapter, it was shown that engineered silk proteins can form spherical assemblies upon addition of salt, and that these assemblies can be forced to aggregate by shear forces. It was also shown that the propensity to aggregate is dependent on the amino acid sequence of the silk proteins and can therefore be controlled carefully.

Furthermore, we know from this chapter's results, that there are still important aspects missing to form fibers instead of more or less random aggregates.

In the next chapter, the attempt to mimick the spider's spinning duct by usage of microfluidic devices will be described.

## 5. Mimicking a spider's spinning duct by microfluidics

### 5.1. Design and Characterization of Microfluidic Channels

As described in Chapter 2, the fiber-forming organ consists of a long duct, where chemical and flow effects take place simultaneously. As it could be shown that engineered silk proteins were also susceptible to the combined application of potassium phosphate and shear forces, and aggregate uncontrolledly in a rheometer, a promising idea to actually produce fibers and study the fiber formation process was to induce and observe the assembly in microfluidic devices.

Thus, microfluidic devices were produced, specifically designed to mimic these spinning ducts in several aspects:

- Ion exchange mechanisms are mimicked by laminar parallel flow of the protein stream and salt-containing outer streams. As the diffusion constant  $D$  for ions is typically at least two orders of magnitude larger than for silk proteins, it is sufficient to consider only the diffusion of salt into the protein stream and neglect the diffusion of protein out into the salt streams. In this fashion, addition of potassium phosphate and alteration of the pH value was achieved.
- Generally, the shear flow present in the spinning duct is also present in the microfluidic channels, and more specifically,
- Elongational flow, which is supposed to play a major role in the formation of fibers, especially in the transition from spherical aggregates to fibers [Jin and Kaplan, 2003] is mimicked by placing narrowing sections in the channels.

These features of the microchannels are combined in a serial way by placing the different elements just after each other along the stream, or combined at one specific site, such as in device for simultaneous mixing and elongation flow shown in Figure 5.1, lower row.

## 5. Mimicking a spider's spinning duct by microfluidics

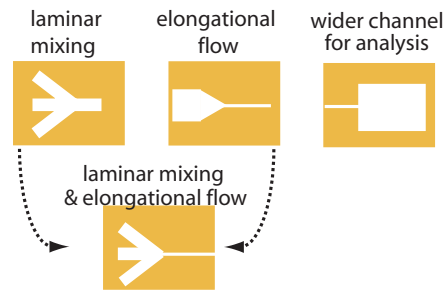


**Figure 5.1.:** Elements of the microfluidic devices used to elucidate the sequence of fiber assembly steps. In the top row, a module where fluids are brought into contact by joining three independent channels to one common one (left), a narrowing channel, which leads to elongational flow components (middle), and a widening channel used to analyze the formed aggregates (right) are sketched. In the lower row, a module that ensures contact of different flow streams while imposing elongational flow is sketched.

The following three designs were used in the experiments discussed in this chapter:

- Laminar Diffusion, Straight Channel: In this type of channels, the secretion of phosphate ions into the spinning dope can be mimicked.
- Laminar Diffusion, Straight Channel, Elongational Flow: In this type of channels, the effect of the elongational flow field can be studied independently of ion-induced effects.
- Simultaneous Laminar Diffusion and Elongational Flow: Finally, this type of channels allows to study simultaneously ion-induced effects and flow effects. This is the class of channels that is most closely related to the natural spinning duct.

Taken together, these three setups allowed to disentangle effects based on salt changes, pH value, and flow properties, by carefully comparing and analyzing the assembled silk aggregates by using Scanning Electron Microscopy, Fluorescence Microscopy, and FTIR. Figure 5.2 shows a micrograph of one of the microfluidic devices with a simultaneous laminar flow and elongational flow part and a wider channel on the left.

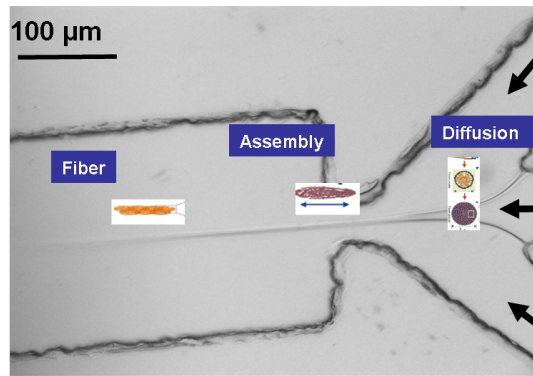


**Figure 5.2.:** Schematic view of fiber formation in microfluidic devices. From the right, protein solution and salt solutions are flown in. As the salt diffuses into the stream of protein, micellar structures begin to form, in analogy to [Jin and Kaplan, 2003]. As the elongational component of the flow increases, symmetry is broken and the spherical aggregates combine into a fiber.

## 5.2. Assembly Process in the microfluidic channels

### 5.2.1. eADF3 assembles into fibers under certain conditions

In rheological studies, eADF3 solutions showed shear induced aggregation, which strongly increased with increasing shear rate (Figure 4.3). Attempting to mimic the processes taking place in the spider's spinning duct one step further towards the natural process, we analyzed eADF3 in our microfluidic channels.

In the microfluidic devices, we were able to produce fibers: however, eADF3 fibers were only found when elongational flow, increase of phosphate concentration (to 500 mM) and a pH drop to pH 6.0 were applied. eADF3 fiber formation started at a flow rate of 600  $\mu\text{l}/\text{h}$  at a concentration of 20 mg/ml. Thus an elongational flow rate of the order of 1000  $\text{s}^{-1}$  suffices to form eADF3 fibers at low protein concentrations. At lower flow rates only spherical eADF3 colloidal aggregates have been observed, similar to aggregates in equivalent quiescent conditions [Exler et al., 2007a]. Under all other experimental conditions with lower phosphate concentrations, without elongational flow or without pH drop, eADF3 assembled into spherical aggregates which slightly differed from those found for eADF4 (Figures 5.3 and 5.6).

Analysis of the resulting eADF3 fibers revealed that they are highly flexible. eADF3 fibers could be stretched by increasing the flow in the direction of the fiber axis or collapsed by inverting the flow direction (Figure 5.4). Analysis of the fibers in crossed-polarizers microscopy showed patches of structurally highly ordered molecules along the thread (Figure 5.4). Their secondary structure con-

## 5. Mimicking a spider's spinning duct by microfluidics

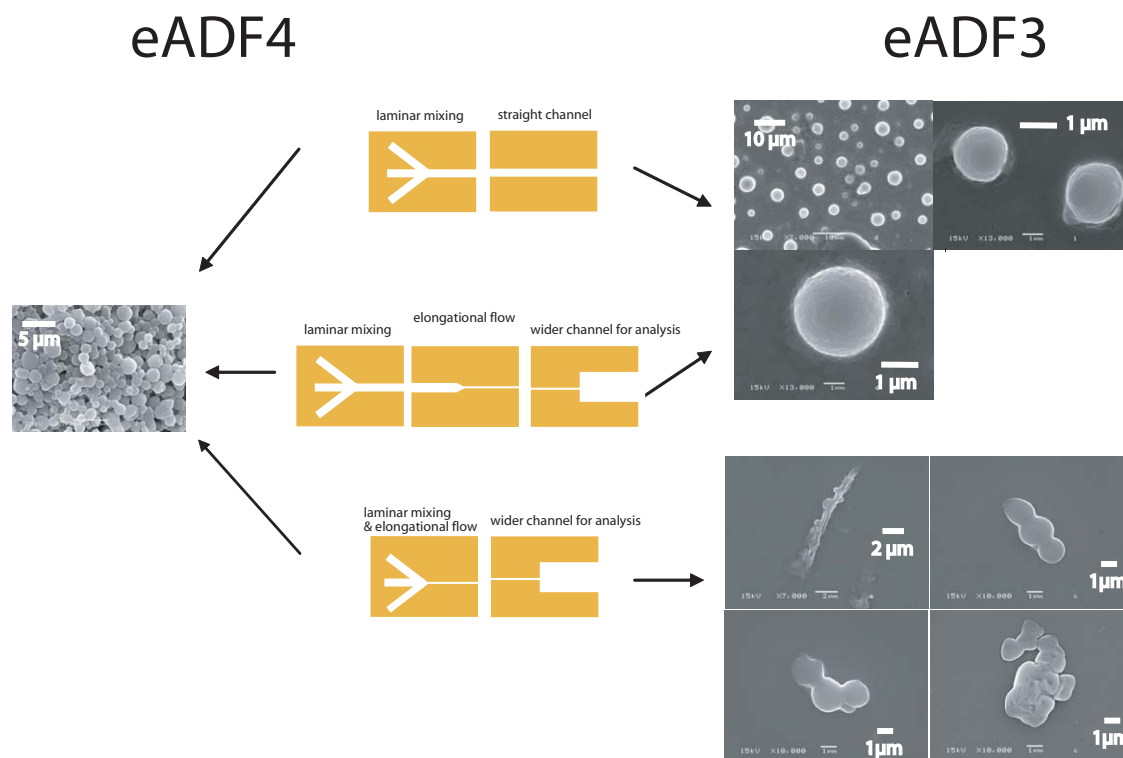


**Figure 5.3.:** The microfluidics modules used in this study: Top, a laminar flow mixing device. No elongational flow component is generated along the flow direction. Middle, a laminar flow mixing device with a bottleneck 1000  $\mu\text{m}$  downstream of the laminar flow mixing region. A fluid element approaching from the left is subjected to an elongational flow just before the bottleneck. Bottom, a laminar flow mixing device with a bottleneck at the point of mixing. An incoming flow element is subjected to elongational flow at the time of mixing with the fluids from the neighboring channels. Mixing always takes place by diffusion only.

tent was observed by FTIR microscopy which revealed that fibers produced in the microfluidic devices contain mainly  $\beta$ -sheets which are responsible for the ordered structural patches as seen in the cross-polarizers spectroscopy. Remarkably, eADF3 fibers were stable in Millipore water even in the absence of potassium phosphate or other ions. This is not the case for the spherical aggregates of eADF3, which disassembled upon replacement of the potassium phosphate buffer with distilled water.

Thus, the presence of attractive interactions between eADF3 spheres alone is not sufficient for fiber formation. Fiber formation is only observed upon simultaneous decrease in pH from 8 to 6 and application of an elongational shear flow. When the solution of eADF3 was adjusted to pH 6 before initiating the elongational flow, no eADF3 fibers were formed (Figure 5.6), and only spherical aggreg-

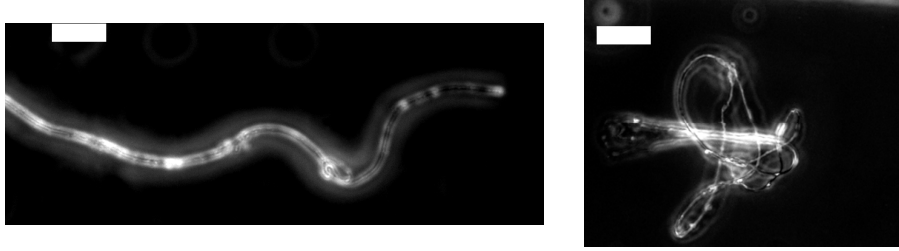


**Figure 5.4.:** Fibers of engineered spider silk proteins assembled in a microfluidic device. (Scale Bar: 10  $\mu\text{m}$ ) Micrographs of fibrous eADF3 (in water). Brighter the intensity in crossed-polarizers microscopy identifies areas of higher and lower molecular orientation. By reversing the direction of flow in the microfluidic device, eADF3 fibers can be collapsed into small coils. Obtained fibers are quite flexible and able to bear large curvatures.

gates were observed. Since only the non-repetitive carboxy-terminal domain of eADF3 contains four amino acids with charged side chains, the necessity of pH change likely indicates the importance of the non-repetitive domain for fiber assembly. NMR studies have shown that the NR domain of eADF3 may work as a dimerization interface and facilitate assembly [Hagn et al., 2009].

It should be noted that the surface of the fibers obtained in the microfluidic channels contain grainy structures, in contrast to the very smooth surfaces of natural silk fibers. Presumably, the assembled structures represent early or intermediate stages of fiber formation, and likely also contain spherical aggregates formed during assembly. Also, it is important to keep in mind that the formation is taking place under water. Drying as found in the natural spinning process is not mimicked in this system and a post-spinning drawing has not been applied.

Importantly, induction of colloidal assembly formation upon addition of potassium phosphate at pH 8 outside the microchannels did not affect fiber assembly: the pre-assembled microspheres converted into fibers when pH drop and elongational flow were applied simultaneously in the microfluidic device. Thus, the pre-formed spheres are forced together by elongational flow and the pH drop mediates irreversible structural conversion into  $\beta$ -sheet rich fibers. These changes in secondary structure are similar to the assembly process of spider silk *in vivo*, and have been reported for rheological *in vitro* studies from *Bombyx Mori* silkworm [Terry et al., 2004].

## 5. Mimicking a spider's spinning duct by microfluidics

### 5.2.2. eADF4 always assembles into spherical aggregates

As shown in figure 4.3, eADF4 does not show shear induced aggregation in the rheometer. The assembly forms observed so far for eADF4 are spherical aggregates [Slotta et al., 2008], nanofibers [Huemmerich et al., 2004c] and hydrogels [Rammensee et al., 2006]. The nanofibers have been shown to grow spontaneously in insect cells as well as *in vitro*.

In order to investigate whether fibers can be formed out of eADF4 in a similar way as out of eADF3, a stream of eADF4 protein solution (10 mg/ml) was mixed with two streams of varying potassium phosphate concentrations and pH values. Surprisingly, no conditions were found for eADF4 to assemble into fibers: only spherical solid protein aggregates were formed under all conditions tested (Figure 5.3 left).

This shows, that the assembly pathways of eADF3 and eADF4 are fundamentally different: While eADF3 forms aggregates that are reversible when potassium phosphate concentration is reduced, and that are highly susceptible to shear forces, the eADF4 assemblies seem to be rather unaffected by their environment, once they have been formed. The differences will be discussed in chapters 5.5.1 and 5.5.2.

### 5.2.3. Blends of eADF3 and eADF4 form stable fibers

Since natural dragline silk consists of both eADF3 and eADF4, we finally investigated the impact of the second dragline silk protein (eADF4) on eADF3 fiber assembly. Therefore, we tested mixtures of both proteins (eADF3:eADF4 weight ratios from 10:1 to 1:1) concerning their behavior in the microfluidic devices. Strikingly, out of the mixture, fibers assembled similar to those of eADF3 alone (Figure 5). In order to visualize the potential incorporation of eADF4, we partially labeled (10 % w/w) eADF4 with the fluorescent dye FITC [Huemmerich et al., 2006]. Fluorescent micrographs revealed homogeneously distributed eADF4 in the assembled fiber (Figure 5.5).

This indicates that neither of the proteins is accumulated or depleted in some regions in the fiber. In contrast, for natural silk a nonuniform distribution of proteins was found [Kummerlen et al., 1996]. Some fibroin proteins were found mainly near the surface of the fiber, and others were concentrated in the interior. It is unknown yet, if this is caused by self-assembly or driven by a mechanism in the spinning duct.



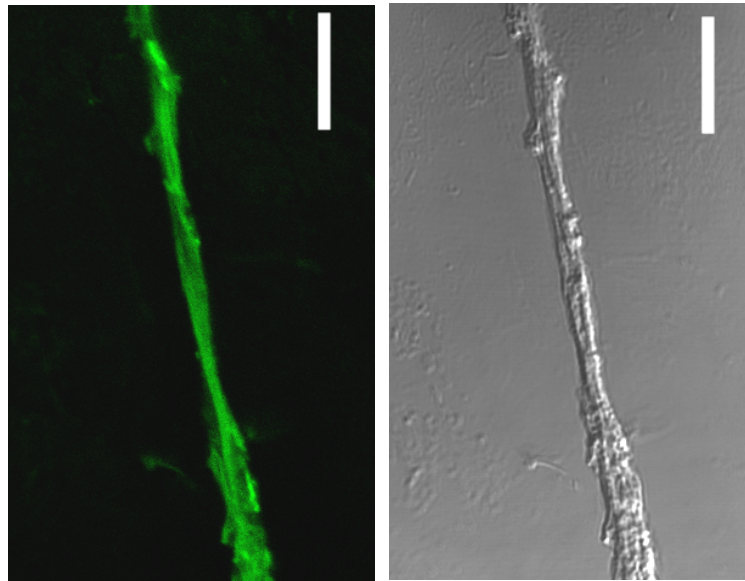


**Figure 5.5.:** eADF3 / eADF4 mixed fibers (Scale bar: 10  $\mu\text{m}$ ) Micrographs of a dried fiber, consisting of both eADF3 and eADF4 (weight ratio 10:1). Left: 10% of the employed eADF4 protein was conjugated with the fluorescent dye FITC (equaling 1% of the total protein). Most FITC-labeled eADF4 has been homogenously integrated into the fiber, as seen by fluorescence microscopy. Right: Differential-interferential contrast micrograph of the same fiber as shown left.

#### 5.2.4. Mode of action of pH change, phosphate addition, and flow effects

Three aspects of fiber formation were varied in our experiments: the addition of potassium phosphate, diffusion of  $\text{H}^+$  ions to lower the pH value, and the shear and elongational flow in the microfluidic channels.

Addition of ions can generally lead to the salting-out of proteins and induces the structure formation of unfolded proteins. Since potassium phosphate plays an important role during the natural spinning process, we investigated its influence on fiber formation in the microfluidic channels [Peng et al., 2005].

Low concentrations of potassium phosphate (<300 mM) help to screen coulombic repulsion between charged amino acids. This effect is reported to screen the repulsion by negatively charged glutamates and lead to self-assembly of eADF4 into nanofibrils with diameters between 2 and 10 nm [Huemmerich et al., 2004b, Slotta et al., 2008]. High salt concentrations (>400 mM) induce formation of microspheres in both eADF3 and eADF4 by altering the protein-water interactions [Munishkina et al., 2004].

## 5. *Mimicking a spider's spinning duct by microfluidics*

Spherical aggregate formation was studied in detail for eADF4(C16). Addition of 1 M potassium phosphate buffer led to an increase in light scattering intensity which reached a plateau after about 5 s, indicating the completion of liquid-liquid phase separation into an aqueous and a concentrated phase [Slotta et al., 2008].

The secondary structure of the microspheres was investigated using FTIR spectroscopy. A maximum at  $1625\text{ cm}^{-1}$  indicates a significant amount of  $\beta$ -sheet structure (64% as determined after deconvolution). Interestingly, the secondary structure of the microspheres is similar to that of nanofibrils formed by the same protein [Slotta et al., 2007].

Importantly, eADF4 microspheres are solely formed above a critical potassium phosphate buffer concentration. Their formation follows a salting-out mechanism which can be considered a liquid-liquid phase separation. The 'one-phase state' is the initial state displayed by a solution of monomeric and intrinsically unfolded protein molecules. Changing a constraint such as the ionic strength by addition of kosmotropic ions alters the free energy of the system and leads to phase separation into protein-rich and solvent-rich phases. This phase-separated state is energetically favored, and the protein concentration in the 'protein phase' increases to a critical level. Results from stopped-flow experiments and Cryo-SEM studies indicating that the spheres are solid suggest that the bulk-growth model of spherical protein is the best explanation for the formation of silk microspheres [Slotta et al., 2008]. Upon reaching the critical concentration for nucleation, several structured nuclei are formed simultaneously in the protein-rich phase. The nuclei start to grow in a spherical manner, interacting with additional monomers and converting their structure. Spherical growth stops when the protein concentration in the protein-rich phase is below the equilibrium of solubility. Hence, the sphere diameter does not increase further. This model is supported by the fact that sphere size depends on protein concentration and mixing conditions [Lammel et al., 2008].

In the natural spinning process, pH changes are another critical parameter. During the passage of the proteins through the spinning duct, the pH is decreased to 6.3 before fibers are formed [Chen et al., 2002]. Therefore, the pH dependence of fiber formation in microfluidic channels was also tested, and it was found that a decrease of the pH from 8 to 6 must occur together with the elongational flow in order to induce fiber formation in the microfluidic channels. However, it was shown previously that fiber formation from the concentrated phase of an eADF3 solution (where the protein concentration exceeds  $1400\text{ }\mu\text{M}$ ) was possible without the change in pH [Exler et al., 2007b]. In that work, it was reported that at pH

### 5.3. Characterization of Spider Silk Aggregates formed in the Channels

values above 8.5 already the liquid-liquid phase separation is inhibited, likely because the usually uncharged tyrosine residues deprotonate at pH 9. The anionic tyrosylates of the hydrophobic blocks increase the hydrophilicity and reduce the hydrophobic interactions. This effect is thought to result in suppression of protein oligomerization, and so no concentrated phase can form. In the case of the assembly in the microfluidic channels, it could be possible that at lower pH lower repulsive forces act between the spherical aggregates, and thus shear-activated aggregation processes are increased (see section 2.5).

Finally, flow effects were shown to induce the aggregation of silk proteins. While the shear effects of the flow are thought to facilitate and accelerate aggregation of the spherical preassemblies, the elongational flow is thought to create the necessary orientation and symmetry-breakup that leads to the formation of fibers instead of spherical or random aggregates. The relative contributions of shear flow and elongational flow effects will be discussed in detail in chapter 5.4.

### 5.3. Characterization of Spider Silk Aggregates formed in the Channels

In order to elucidate specific differences between fibers and aggregates formed under different conditions and with different proteins, several material characterization tests were performed, which will be presented in the following sections:  $\beta$ -sheet content was measured by FTIR spectroscopy, water content was measured by comparing wet and vacuum-dried fibers, and the stability of the aggregates was determined by placing them in denaturing baths of varying strength.

#### 5.3.1. Secondary Structure composition

As the mechanical properties of silk threads are thought to be achieved mainly by intermolecular  $\beta$ -sheets, the secondary structure content of silk assemblies may be a valuable measure to assess the question of how well connected these assemblies are on a molecular level [Lefevre et al., 2007, Rousseau et al., 2006]. Together with information on the stability in chemical and mechanical terms, this information will lead towards a structure-function relation for silk proteins [Porter and Vollrath, 2009].

In solution, eADF proteins do not assume a specific secondary structure. Thus, the Amide-I adsorption has a peak around 1640-1650  $\text{cm}^{-1}$  (Figure 5.7). Several eADF aggregates were tested on their secondary structure content, as shown in

## 5. Mimicking a spider's spinning duct by microfluidics

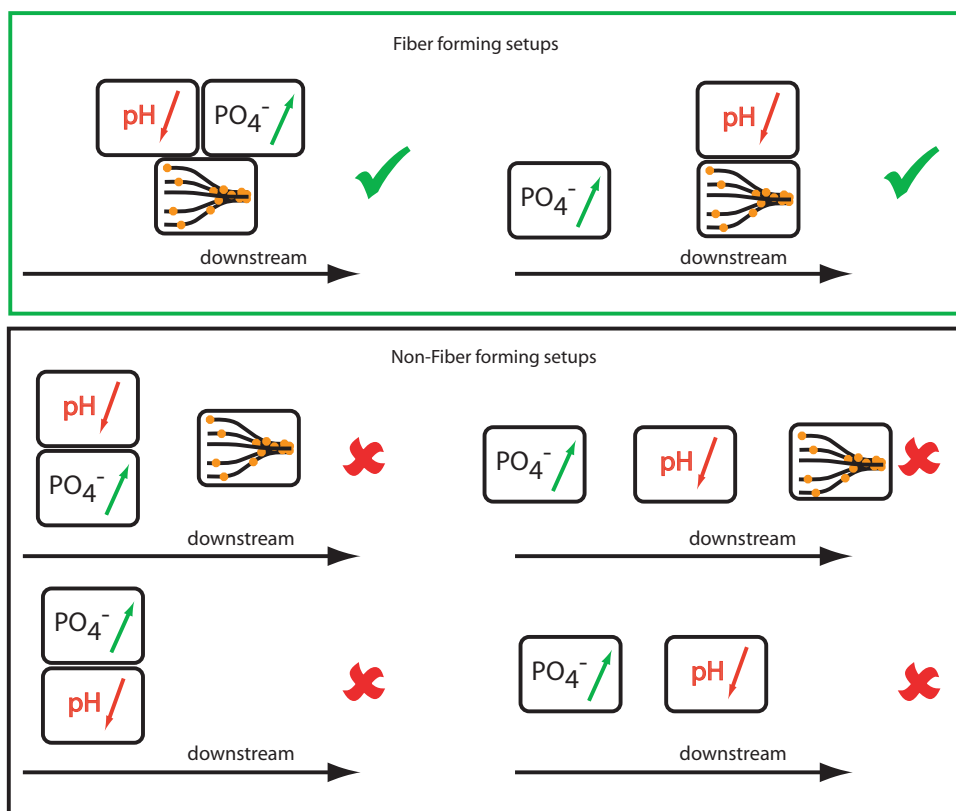


**Figure 5.6.:** Overview of the results on eADF3 assembly in microfluidic devices. Top panel: Elongational flow, salting out, and pH changes are necessary for silk fiber formation. The induction of sphere formation by addition of phosphate occurs before the elongation flow. The pH drop, however, has to accompany elongational flow to induce the aggregation of the pre-formed spheres into fibers. Simultaneous to fiber formation, the secondary structure of the aggregates is changed to  $\beta$ -sheets. Middle panel: If the pH is changed before elongational flow is applied, no fibers can assemble. The simultaneous pH drop and elongational flow is mandatory for fiber formation. Bottom panel: If no elongational flow is applied, fibers do not form in any case. Elongational flows above  $1000 \text{ s}^{-1}$  were found to be necessary for fiber formation in this setup.

table 5.1. As expected from previous results, eADF4 formed aggregates very rich in  $\beta$ -sheets [Slotta et al., 2008]. Most remarkably is the difference in secondary structure from eADF3 spherical assemblies, which contain mostly helical and random coil structures, to eADF3 fibers, which were found to contain more  $\beta$ -sheets. This could be caused by stretching of the nascent fiber in the flow, as extension has been shown to cause transitions from helical to  $\beta$ -sheet structures [Fudge et al., 2003].

The fibers from both eADF3 and eADF4 contained less  $\beta$ -sheets than the eADF4 spheres as well as the eADF4 fibers. It remains a question still to answer, whether this results from different conditions during fiber formation (the condi-

### 5.3. Characterization of Spider Silk Aggregates formed in the Channels

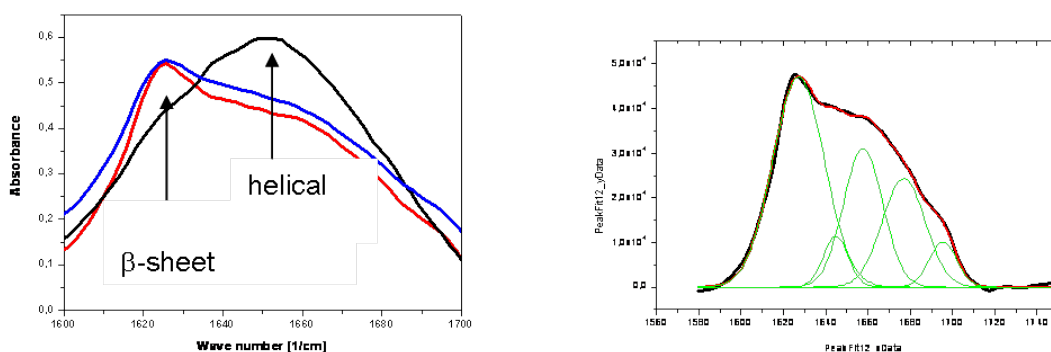


**Figure 5.7.:** Amide I region of infrared spectra of engineered spider silk proteins. All samples were dried on CaF<sub>2</sub> and washed with Millipore water. eADF4 spherical aggregates stayed stable and show  $\beta$ -sheet conformation (left, red curve). eADF3 spherical aggregates dissolved and formed a film with mainly alpha-helical secondary structure (peak at 1660 cm<sup>-1</sup>) (left, black curve). Fibers of eADF3 and eADF4 were stable and showed  $\beta$ -sheet rich secondary structure (peak at 1625 cm<sup>-1</sup>) (left, blue curve). eADF4 alone was not able to form fibers under the employed conditions. In the right panel, the assignment of secondary structure elements is illustrated ([Byler and Susi, 1986]). The results for the different silk assemblies are given in Table 1.

tions could have been unchanged) or the actual molecular interactions between eADF3 and eADF4.

Silk Assembly	helical (1648-1664 cm <sup>-1</sup> )	$\beta$ -sheet (1625-1640cm <sup>-1</sup> , 1688 -1692cm <sup>-1</sup> )	$\beta$ -turn (1665-1685cm <sup>-1</sup> )
eADF3	55 %	18 %	16 %
eADF3 Fiber	31 %	45 %	25 %
eADF4 Sphere	16 %	63 %	21 %
eADF3+eADF4 Fiber	46 %	40 %	13 %

**Table 5.1.:** Secondary Structure contents of a variety of spider silk assemblies. Infrared spectra were analyzed in order to determine secondary structure composition of the protein assemblies. eADF3 assemblies generally showed more helical structures than eADF4 assemblies, which revealed a high content of  $\beta$ -sheet structures. Fibers of eADF3 and eADF4 were thermodynamically stable and showed  $\beta$ -sheet rich secondary structure (peak at 1625 cm<sup>-1</sup>). However, eADF3 fibers revealed a higher relative content of  $\beta$ -sheet structures than the mixed fibers of eADF3 and eADF4.

#### 5.3.2. Stability in denaturing agents

Stability of silk aggregates against dissolving is founded in their secondary structure content. This is due to many intermolecular  $\beta$ -sheets that can be formed in samples which show a high  $\beta$ -sheet content in FTIR spectroscopy. Samples which

## 5. Mimicking a spider's spinning duct by microfluidics

Protein	10 mM Tris	8 M Urea	6 M GdnSCN
eADF3	not soluble	soluble	soluble
eADF4	not soluble	not soluble	soluble
eADF3 spheres	stable	not stable	not stable
eADF4 spheres	stable	stable	not stable
eADF3 fibers (no NR)	stable	< 10 min stable	not stable
eADF3NR fibers	stable	> 40 min stable	not stable
eADF3NR+4 fibers	stable	> 40 min	not stable

**Table 5.2.:** Resistance to denaturing agents

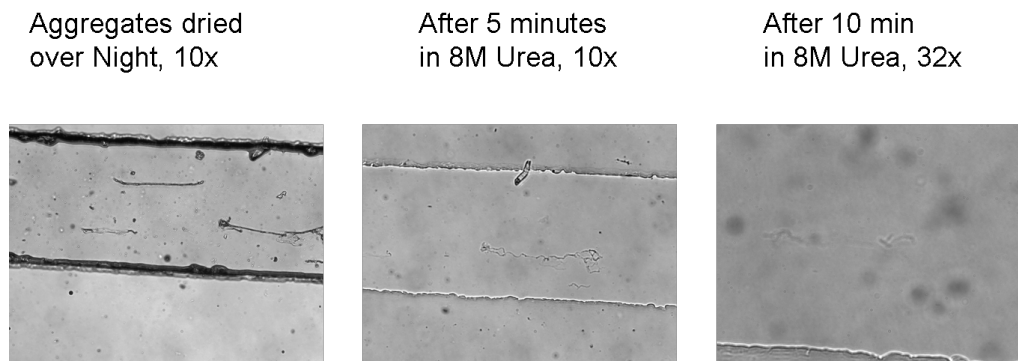


**Figure 5.8.:** Dissolving process of eADF3 aggregates in 8M Urea

do not contain fewer  $\beta$ -sheet structures, cannot develop as many intermolecular hydrogen bonds and can thus be dissolved more easily.

To test the stability, silk aggregates were dried over night and then immersed in the respective solvents (Figure 5.8)

Table 5.2 shows the temporal stability of various silk aggregates against various solvents. It can be seen, that the strongest aggregates are generally those that contain eADF4. Spherical eADF3 aggregates that contain assemblies of eADF3 readily dissolve in 10 mM Tris buffer, after phosphate has been diluted away. Interestingly, fibers formed from eADF3 were more stable than the spontaneously forming spherical aggregates.

The fact that eADF3 fibers with the non-repetitive domain (AQ<sub>24</sub>NR) are 4 times longer stable in 8 M Urea than fibers formed from the eADF3 variant without the non-repetitive domain (AQ<sub>24</sub>), shows that this domain is of high importance in the control of fiber assembly. It was shown that the non-repetitive domain acts as a dimerization interface and as a nucleus for subsequent accretion of additional pairs of dimerized eADF3 proteins [Hagn et al., 2009].

### 5.3.3. Water content

Water content plays a major role in the mechanical properties of silk fibers [Schäfer et al., 2008]. The weight of a silk fiber can consist up to two thirds of water at high relative humidity [Vehoff et al., 2007]. Water swells the amorphous matrix and reduces the number of hydrogen bonds in the intermolecular  $\beta$ -sheets. This effect increases with relative humidity. When the fiber is immersed in water, the fiber shrinks to about half of its original length and the diameter increases six-fold. This process is called Supercontraction [Savage and Gosline, 2008, Savage et al., 2004].

Figure 5.9 shows fibers of eADF3 and eADF4 produced under water in the microfluidic devices. As a preparation for SEM imaging the glass cover slide of the device was removed and the PDMS surface with the fibers adhering to it was sputtered with gold. After the sample is placed in the microscope holder, the instrument is evacuated before taking pictures. In the SEM pictures, the fiber is broken into pieces, because it shrunk during drying and subsequent evaporation of water. It is also possible to see, that the fiber looks very flat.

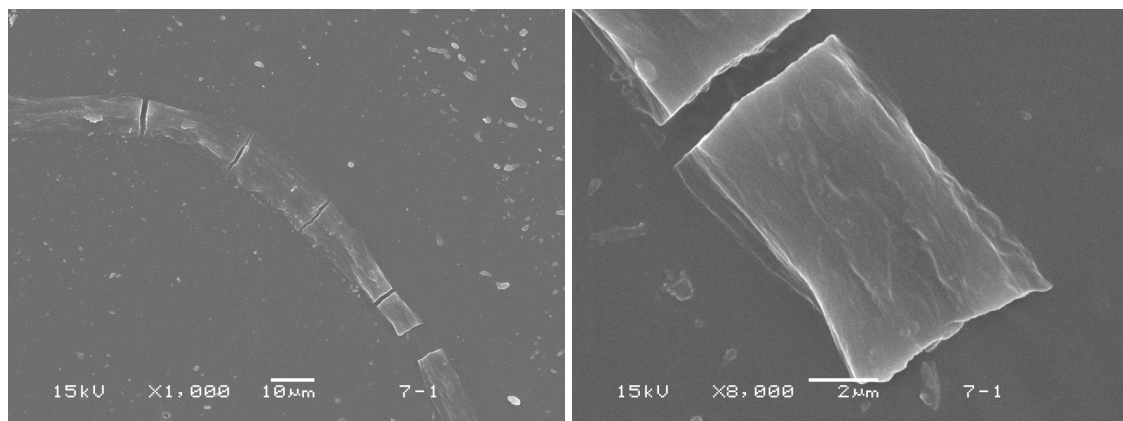


**Figure 5.9.:** SEM image of fiber produced in the microfluidic device

These results show that the fibers produced in the presented microfluidic channels are not yet stable final fibers, but represent probably an early or intermediate step in fiber formation. In nature, water removal is achieved in the third limb of the spinning duct and this process is not at all mimicked in the microfluidic devices so far [Kojic et al., 2004].

Thus, challenging aspect, yet to be mimicked in microfluidic devices, is the extraction of water from the protein stream during fiber formation. This could for instance be achieved by means of dialysis membranes, and placing a very hygroscopic liquid on the outer side of the membrane. However, tight sealing of

## 5. *Mimicking a spider's spinning duct by microfluidics*

membranes to microfluidic devices turned out to be challenging. Furthermore, the optical properties of dialysis membranes are poor.

Another approach towards water management in the fiber formation process in microfluidic devices was to produce the channels in a very porous gel. Materials that were tested in this context include Agarose gels and Polyacrylamide gels. With these materials it turned out to be very difficult to connect the external tubing.

### 5.3.4. Mechanical testing of short fibers

Typical lengths of the silk assemblies formed directly in the microfluidic devices was less than  $300\ \mu\text{m}$ . It is very challenging to assess the mechanical properties of objects in this size range: the fiber fragments are too small to be tested in a conventional fiber testing device, where typically several centimeters of material are required. On the other hand, the fragments are too long and strong for most microscopic methods such as Atomic Force Spectroscopy (AFM).

One micromechanics method that can be used to test short fiber fragments are optical traps. The working principle of an optical trap is the following: When a transparent bead (typically a few  $\mu\text{m}$  in diameter) is in the focus of a laser beam, the diffraction of light caused by the index of refraction mismatch between the material of the bead and the surrounding medium leads to an effective force holding the bead in the center of the laser beam.

In principle, optical traps can assess the length regime that would be of interest to test the short fiber fragments produced in the microfluidic channels. The limiting element in force measurements with optical traps is the spring constant of the trap, and thus the maximum force that the trap can exert on a bead.

The force measurements on the short fragments of engineered silk fibers were done together with Melanie Reisinger. First, eADF fibers from mixed eADF3 and eADF4 were produced, with 50% of the eADF4 in a biotinylated form. These fibers were then mixed with streptavidin coated beads and placed in the optical trap. A bead was trapped and brought into contact with the fiber fragment. The trap strength was determined by the fluctuations of the bead to be 50 pN [Clemen et al., 2005, Gebhardt et al., 2006].

Force was then exerted to the fibers in two ways. First, pulling in the direction of the fiber caused no displacement of the fiber within the optical resolution. Rather than moving or elongating the fiber, the bead was pulled out of the trap.

When force was exerted perpendicular to the fiber axis, the bead could be dis-



### 5.3. Characterization of Spider Silk Aggregates formed in the Channels

placed for about  $1.5 \mu\text{m}$  before it dropped out of the trap.

With the relation for the bending rigidity  $\kappa$

$$\kappa = \frac{F}{y(L)} = 3 \frac{EI}{L^3}$$

where  $F$  is the trap force, and  $L$  is the length of the displaced fiber piece.  $E$  is the elasticity modulus and  $i$  is the planar moment of inertia [Howard, 2001]. Thus,

$$E = \frac{FL^3}{3Iy(L)}$$

We calculated  $E$  to be of the order of 8 kPa for our fibers, with experimental parameters as mentioned above and  $I = (\pi/4)r^4$ . The flexural rigidity  $EI$  of the fiber is thus  $1.0 \cdot 10^{-19} \text{ Nm}^2$ .

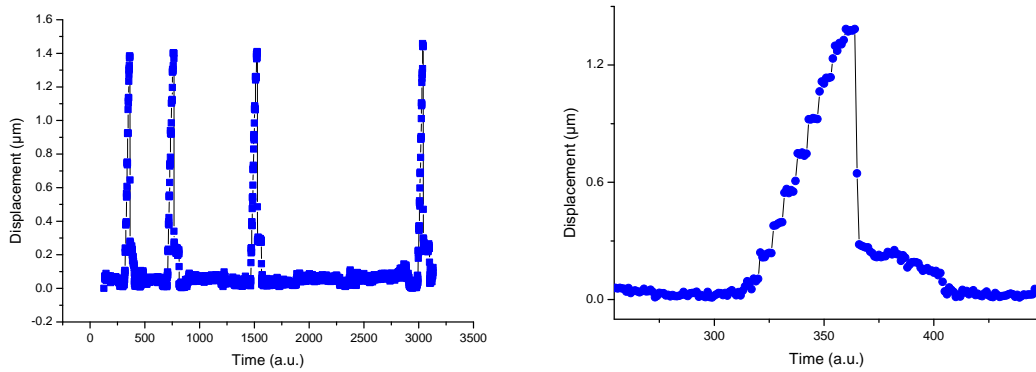


**Figure 5.10.:** Displacement of a bead attached to a silk fiber. The trap strength was 50 pN. On the left hand side, one can see that the deformation was completely elastic, as the fiber relaxes to the original shape. On the right hand side, a larger scaling of the time axis was chosen, to display the displacement and relaxation in detail.

The measured values are very low and can only be regarded as lower bounds for the mechanical properties of silk assemblies produced in the microfluidic devices, as the range of deformation, that could be achieved with the very limited force of the optical trap, was very low. Thus, only the initial modulus at very low deformations was assessed with these experiments. However, it is well known that the force-extension curves of silk fibers show a relatively low increase of the stress with low deformations, and that the stress increases significantly only at larger deformations [Gosline et al., 1999].

## 5.4. Analysis of the Flow Conditions that lead to Fiber Formation

### 5.4.1. Shear thinning behaviour of concentrated eADF solutions

Aequos solutions of eADF3 show a phase separation into a protein-rich and a protein depleted phase when dialyzed slowly from denaturing conditions to 10 mM Tris pH 8 [Exler et al., 2007b].

The protein rich phase of eADF3 shows distinct shear-thinning behaviour typical for polymeric liquids (Figures 5.11 and 5.12). Strikingly, the solutions showed a distinct hysteresis: When a shear ramp was performed from low to high shear rates, the first flow curve shows a viscosity about one order of magnitude larger than the second one. After waiting for times up to one hour, the original behaviour was not recovered. This indicates that even with no potassium phosphate present, highly concentrated eADF3 solutions are susceptible to shear induced aggregation effects, which seem to be qualitatively similar to observations reported on whole spinning dope extracts [Holland et al., 2006, Chen et al., 2002].

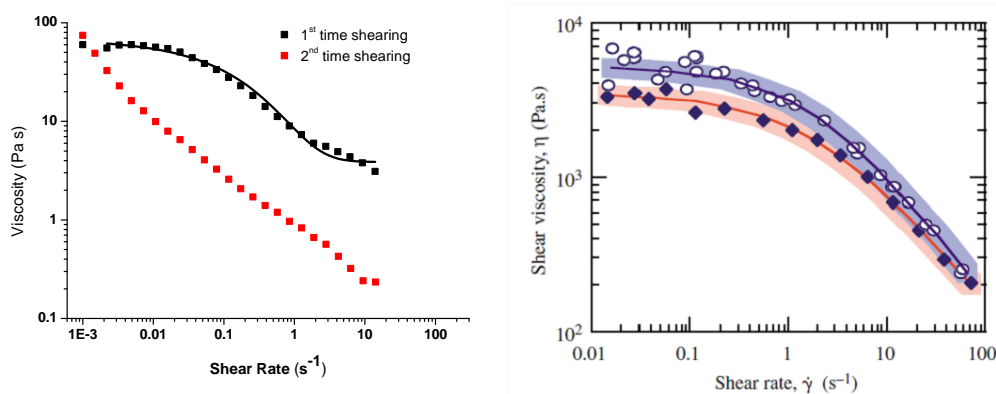


**Figure 5.11.:** Left: eADF3 in aequos solution at 100 mg/ml shows a distinct shear thinning behaviour. Remarkably, the viscosity remains lowered if the shear ramp from low to high shear rates is repeated right after the first experiment. Right: Shear thinning of silk gland extract. Figure from [Kojic et al., 2006]

The results obtained for the shear-thinning behaviour of engineered silk solutions are very similar to those acquired for whole-gland extracts from spider's spinning ducts [Kojic et al., 2006], but the absolute values measured for the viscosity are approximately one order of magnitude lower for the engineered silk solutions.

#### 5.4. Analysis of the Flow Conditions that lead to Fiber Formation

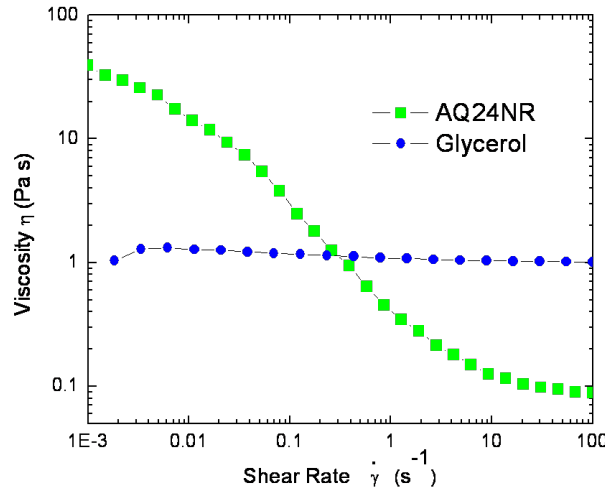


**Figure 5.12.:** eADF3 (60 mg/ml) shows a distinct shear thinning behaviour. In contrast, glycerol is a perfect Newtonian fluid.

Furthermore, shear-thinning is characteristic for concentrated polymer solutions due to the loss of molecular entanglements. It can be described by phenomenological constitutive models such as the Carreau-Yasuda equation:

$$\eta(\dot{\gamma}) = \eta_{\infty} + (\eta_0 - \eta_{\infty})[1 + (\dot{\gamma}\lambda)^a]^{-n}$$

where  $\eta_0$  is the zero-shear rate viscosity,  $\lambda$  is a characteristic relaxation time of the polymer, and  $n$  is the power-law coefficient for the shear-thinning regime, and  $a$  is the rate of transition between the plateau-like zero-shear rate viscosity and the power-law region [Bird et al., 1987].

The best fit parameters to our experimental data are presented in table 5.3 in comparison with results obtained on the full extract of spider's spinning gland. The parameters found for the engineered silk solutions reflect a significantly lower zero-shear viscosity  $\eta_0$ . Accordingly, the values of the parameters  $\lambda$ ,  $a$ , and  $n$ , which describe the shear-rate dependence of shear-thinning are indicating a significantly faster shear-thinning process for the engineered silk solutions. These large differences originate in both the lower protein concentrations used for the engineered solutions as well as in the smaller molecular weight of the engineered silk proteins.

## 5. Mimicking a spider's spinning duct by microfluidics

	eADF4 viscous phase	natural gland extract [Kojic et al., 2006]
$\eta_0$ (Pa s)	60	3500
$\lambda$ (s)	0.015	0.4
a	0.53	0.68
n	12	0.18

**Table 5.3.:** Carreau-Yasuda parameters for solutions of engineered spider silk protein and for natural spinning dope.

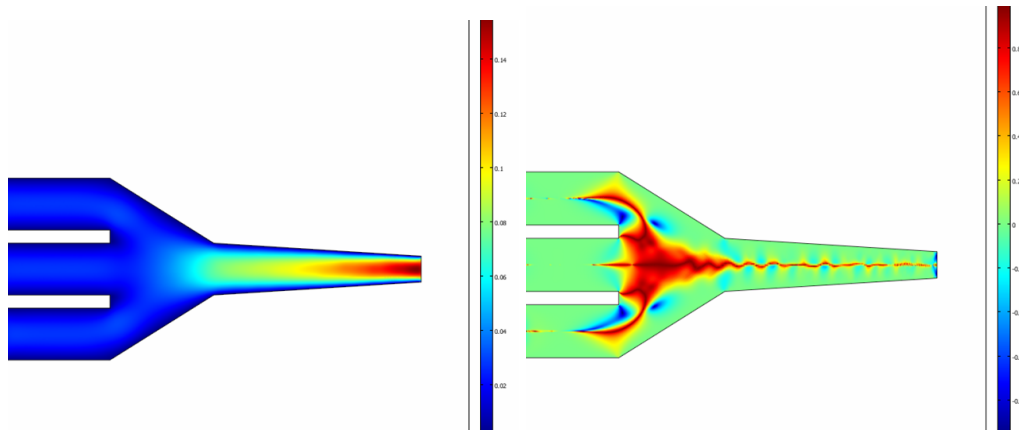


**Figure 5.13.:** Velocity field (left, unit is m/s) and Flow Type Parameter (right, dimensionless) as calculated. The width of the incoming channels from the left is  $100 \mu\text{m}$ . The flow type parameter indicates, that the flow in the narrowing parts of the channel is almost purely of an elongational nature.

### 5.4.2. Simulation of the flow in Fiber forming channels

Generally, a Carreau-Yasuda model for a shear thinning fluid was used to model silk protein flow through the microfluidic devices. The model fluid is described by the shear dependent viscosity

$$\eta(\dot{\gamma}) = \eta_0 [1 + (\dot{\gamma}\lambda)^a]^n$$

where  $\eta_0$  is the zero-shear rate viscosity,  $\lambda$  is a characteristic relaxation time of the polymer, and  $n$  is the power-law coefficient for the shear-thinning regime. It should be noted that the shear thinning model used for the FEM simulations is slightly different from the model used in section 5.4.1. The model used for the simulations does not include a finite viscosity for high shear rates  $\eta_\infty$ , which is favourable for numerical simulations.

In order to characterize the nature of the flow in a given channel with respect to the shear and elongational components, a dimensionless flow-type parameter

is introduced [Lee et al., 2007]:

$$\zeta = \frac{|\underline{\dot{\gamma}}| - |\underline{\omega}|}{|\underline{\dot{\gamma}}| + |\underline{\omega}|}$$

where  $|\underline{\dot{\gamma}}|$  is the magnitude of the strain tensor, and  $|\underline{\omega}|$  is the magnitude of the vorticity tensor. The flow type parameter  $\zeta$  can assume values between 1 and -1, with the following denotations:

- $\zeta = 1$ : Purely elongational flow,
- $\zeta = 0$ : Purely shear flow,
- $\zeta = -1$ : Purely rotational flow.

Figure 5.13 shows the result of a flow field simulation. On the left hand side, one can see that the velocity field increases with the narrowing channel, as expected. On the right hand side, the flow type parameter  $\zeta$  is plotted.  $\zeta$  is around 1 where the three channels meet, indicating that in the region where salt ions are added to the stream of protein, there are predominantly elongational flow effects.

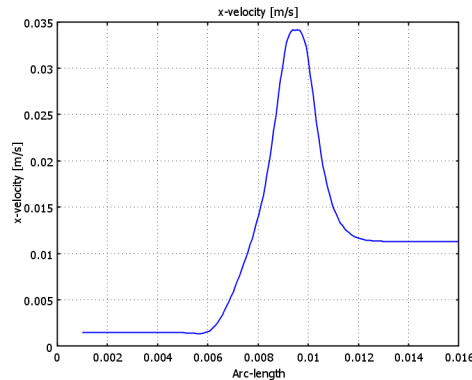


**Figure 5.14.:** Velocity Profile along the center of the microfluidic device.

## 5.5. Discussion of the Fiber assembly process

### 5.5.1. Assembly kinetics

As the main result of the experiments with different setups of microfluidic channels was that elongational flow is a necessary pre-condition for eADF3 fiber formation, the aberrant assembly behavior of eADF3 and eADF4 likely emerges from differences in their response to flow.

## 5. Mimicking a spider's spinning duct by microfluidics

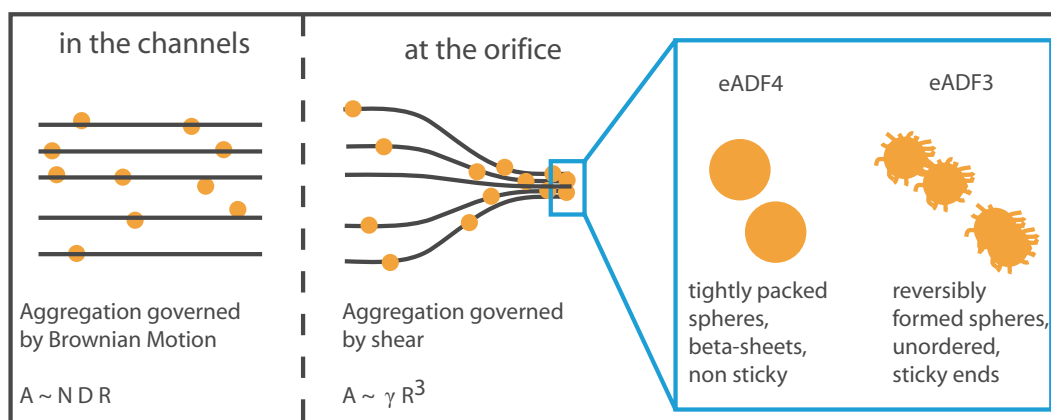


**Figure 5.15.:** Model for interaction of engineered spider silk proteins. Upon moderate flow rates, Brownian motion dominates the aggregation of spherical protein colloidal assemblies. The Aggregation rate  $A$  is proportional to the density of particles  $N$ , their radius  $R$ , and their Diffusion constant  $D$ . In the proximity of the small orifice in the microfluidic device, particles traveling along the streamlines of the medium are forced into contact, drastically increasing the aggregation rate. Under these conditions, aggregation rate  $A$  is proportional to the shear rate  $\dot{\gamma}$  and to the third power of the particles' radius  $R$  [Smoluchowski, 1917]. eADF4 spherical colloidal assemblies are apparently "smooth", no dangling ends stick out and contribute to sticking interactions with neighboring colloidal assemblies. In contrast, eADF3 spherical colloidal assemblies are supposed to have dangling ends which can mediate interactions between neighboring aggregates [Tripathi et al., 2006, Marrucci et al., 1993]. Moreover, eADF3 spherical aggregates can be dissolved before aggregation into fibers.

In the (cone-and-plate) rheometer, only shear flow is present. The flow in the microchannels, however, can be described as a shear flow at comparably low shear rates of  $50 \text{ s}^{-1}$ . Only in the bottlenecks, the superimposed elongational flow is the dominating flow effect, resulting in aggregation of eADF3.

In general, spherical colloidal assemblies are forced into contact when the respective streamlines of the solvent get closer than the diameter of the particles. Such behavior has been shown to be the dominant cause for aggregation for particles in the  $\mu\text{m}$  range [Squires and Quake, 2005] and to induce shear activated irreversible aggregation [Smoluchowski, 1917]. Once the colloidal silk spheres interact, the intrinsic characteristics of eADF3 and eADF4 contribute to a behavior that can be interpreted by a model originally developed for associative polymers in flow [Guery et al., 2006]. Hydrophilic side chains presumably stick out of the spherical colloidal assemblies of eADF3 and form dangling ends that can interact with neighboring spherical colloidal assemblies (Figure 5.15). If interactions are favored kinetically, shear thickening can be observed [Guery et al., 2006]. Shear increases the collision rate of individual proteins or assemblies [Tripathi et al.,

2006] by increasing the root-mean square projection of the chain dimension in the deformation direction. Such behaviour was observed for eADF3 colloidal assemblies which can interact during elongational flow upon increase of the hit rate of dangling ends [Guery et al., 2006]. As a result, viscosity increases over time, and a macroscopic clot of aggregated material forms. Spherical colloidal assemblies of eADF3 revealed predominantly helical conformation, indicating that its conformational state is not that of the final fiber (Table 5.1) [Lefevre et al., 2007, Rousseau et al., 2006]. eADF3 aggregates can be resolved by reducing the concentration of potassium phosphate (and its accompanying salting out effect). Upon sphere formation, conformational changes into  $\beta$ -sheet secondary structure occur as well as irreversible aggregation of eADF3 into fibers induced by applied shear forces. Therefore, we assume that sphere formation is a pre-requisite for fiber formation.

### 5.5.2. Differences between eADF3 and eADF4

In contrast, for eADF4 addition of potassium phosphate (> 300 mM) results in increased hydrophobic interactions accompanied by a dense packing of the proteins. Such tight packing leads to extremely smooth surfaces of the spherical colloidal assemblies. The high aggregation propensity of eADF4 results in the formation of chemically stable spheres in the presence of potassium phosphate [Slotta et al., 2006], with a high content of  $\beta$ -sheet secondary structure (Table 5.1). The lack of dangling ends results in undisturbed flow of the eADF4 colloidal assemblies at the investigated shear rates and times (Figure 4.3). Irreversible sphere formation of eADF4 occurs rapidly, and the accompanying conformational change of the protein is probably initiated in the centre of the spheres [Marucci et al., 1993]. Thus, no further interaction between spherical colloidal eADF4 assemblies is possible, and no fiber assembly of eADF4 occurs (Figures 5.3 and 5.6).

### 5.5.3. Influence of elongational flow

The results of this chapter show that the elongational flow is extremely important in fiber formation. It was shown under which conditions fibers are formed and under which not. By trying many different channel configurations, information about the sequence of steps involved in fiber formation could be obtained.

In a Finite Element Modelling study similar to the work presented above, flow properties in silkworm silk glands and in spider spinning ducts were studied and compared [Breslauer et al., 2009]. It was shown that the elongational flow in the

## 5. *Mimicking a spider's spinning duct by microfluidics*

silkworm's gland is much less pronounced and more steadily distributed along the length of the channel. In spiders, the accumulated strain on the molecules is much higher and most of the extension is applied in the end of spinning duct. It is therefore possible, that the better mechanical properties of spider silk compared to silkworm silk is at least in part due to molecular orientation in spider silk fibers. The orientation is achieved by stretching of proteins in elongational flow, which will be studied in the next chapter. It should be noted that neither in the work presented here nor in the study by [Breslauer et al., 2009], elongational flow effects were actually taken into account to calculate the flow profiles. In both cases, only the shear thinning behaviour of spinning dopes was included in the models.

Further studies in the microfluidic channels could include different geometries which impose varying accumulated elongational strains to the forming fibers, possibly altering their mechanical properties.

### 5.5.4. Further Directions of Research

It would be of great interest to increase the knowledge about when in the fiber formation process the secondary structure of silk proteins actually changes to a beta-sheet rich conformation.

Methods to investigate this would be Raman microspectroscopy, Infrared spectroscopy (FTIR), x-ray diffraction and the employment of dyes that bind specifically to certain secondary structures. Initial work using x-ray diffraction on the assembly of reconstituted Bombyx Mori silk in a microfluidic device has been performed [Martel et al., 2008].

In-situ FTIR has turned out to be challenging. Due to the strong water adsorption band in the Amide I region, proteins have to be transferred into D<sub>2</sub>O for these experiments. Also, it has turned out to be very tedious to build microfluidic devices of IR transparent material (Grabmayr 2008).

Thioflavin T is an example for a dye that binds specifically to beta-sheet structures and undergoes a change in fluorescence emission when bound. Initial experiments with this dye in the microfluidic channels suggested that the dye requires quite a long time to diffuse into the protein stream and to bind to beta sheet structures.



## 6. Capillary Breakup: Rheology and Fiber formation

In order to elucidate the effect of molecular stretching on the formation and quality of fibers, elongational flow in a free surface configuration was studied. This is useful, as even in the microfluidic devices specifically designed to cause elongational flow, shear forces play a -not negligible - role due to the small distances to the walls of the channels. These shear effects could dominate or alter the effects of elongational flow, which can be ruled out in free surface flows.

Elongational viscosimetry mainly probes the stretching relaxation modes of polymers. Practically, this means that a long polymer will remain stretched longer than a short one, and the long polymer will even be more susceptible to stretching at lower elongation rates. The amount of molecular stretching depends on the molecule's Deborah number  $De = \tau_R/t_p$ , where  $\tau_R$  is the characteristic relaxation time of the polymer and  $t_p$  is the typical time-scale of the experiment. In the Rouse model, the longest relaxation time  $\tau_R$  of an ideal chain is given by

$$\tau_R \approx \tau_0 N^2$$

where  $\tau_0$  is the shortest relaxation time and  $N$  is the degree of polymerization [Rubinstein and Colby, 2003].

In the natural spinning process, the final step is the transition from a highly viscoelastic fluid to a solid phase [Vollrath and Knight, 2001, Vollrath et al., 1998, Knight et al., 2000]. This is achieved by water removal in the third limb of the spinning duct, where epithelial cells with increased surface by microvilli adsorb water. The diffusion of water through the forming fiber is considered to be the rate-limiting step [Kojic et al., 2004].

Availability of both elongational and shear viscosity data for a given sample greatly increases the understanding of the various dissipation effects in a more complex flow, such as for instance in the spinning duct of the spider.

This kind of measurement has been impossible up to the availability of very pure engineered spider silk solutions. Previous work has been done to investigate rheological properties of full extracts of spinning glands [Kojic et al., 2006]. The results of this work will be compared with our results in subsection 6.2.

Elongational rheometry measurements were conducted on solutions of both

## 6. Capillary Breakup: Rheology and Fiber formation

eADF3 and eADF4 spider silk proteins with various salt concentrations and in aqueous as well as Hexafluoroisopropanol (HFIP) and Formic Acid solutions.

In very highly concentrated silk protein solutions, the formation of stable fibers was observed. The mechanical properties of these fibers were studied in dependence of Methanol treatment as well as on the addition of short fragments of the engineered silk proteins. Finally, mechanical measurements on natural spider silk were performed in order to compare the properties of fibers from engineered silk and natural silk.

### 6.1. Ohnesorge Number

In order to obtain a stable fiber, the fluid filament must gain stability against being broken up by surface tension during the formation of the fiber. A water filament, for instance, is not stable against surface tension and will break up after a fraction of a second. This effect is well known from any water tap, and the instability that occurs here is known as the Plateau-Rayleigh instability.

This is described by the Ohnesorge number  $Oh$ . It is a dimensionless number describing the relative contributions of viscous forces and surface tension forces. It is defined as

$$Oh = \frac{\eta}{\sqrt{\rho\sigma L}} \quad (6.1)$$

where  $\eta$  is the viscosity,  $\sigma$  is the surface tension,  $\rho$  is the density and  $L$  is a characteristic length scale, in the cases described here typically the fluid filament diameter.

The viscosity  $\eta$  should be understood generally as the resistance to deformations along any axis. Thus, for elongational deformation, we may write  $Oh = \eta_E / \sqrt{\rho\sigma L}$ , with  $\eta_E$  being the elongational viscosity. For newtonian fluids,  $\eta = 3\eta_s$ , as showed in section 2.7. For polymer solutions, the ratio  $\eta_E / \eta_s$  can be of the order of  $10^4$  to  $10^5$ . Thus  $Oh$  for these solutions becomes very large, and stable fluid filament development, often associated with the beads-on-a-string effect, are observed [Edmond et al., 2006, Sattler et al., 2008].

### 6.2. Elongational Viscosity of eADFs in aqueous solution

Elongational flow was found to be an important prerequisite for fiber formation in the microfluidic channels. In order to draw conclusions on possible molecular orientation, elongational rheology data was obtained for solutions of eADF3

proteins.

### 6.2.1. Elongational Rheology of dilute solutions of eADF3

Elongational flow was found to be a prerequisite for fiber formation in the microfluidic channels. In order to determine, how the flow rates that were experimentally used affect the proteins on a molecular scale, it is necessary to measure polymer relaxation times in elongational flow. Thus, eADF3 solutions of a concentration of 10 mg/ml were investigated in the Capillary Breakup Extensional Rheometer. However, a principal experimental problem prevented to directly perform elongational rheometry on these solutions: the shear viscosity of such solutions is only slightly higher than that of water, and thus these solutions are not suitable for CABER, as the surface tension dominates all flow effects. Minimal viscosities for meaningful CABER results were found to be in the order of 70 mPas [Rodd et al., 2005].

By adding glycerol to the solution of spider silk protein, it is possible to increase the shear viscosity and render dilute silk protein solutions suitable for CABER experiments. The longest relaxation time  $\lambda$  of a monodisperse homopolymer in dilute solution is described by the Rouse-Zimm theory [Doi and Edwards, 1986] and scales with the following parameters:

$$\lambda \propto \frac{\eta_s M_w^{3\nu}}{RT}, \quad (6.2)$$

where  $\eta_s$  is the viscosity of the solvent,  $M_w$  is the molecular weight of the solute and the exponent  $\nu$  is related to the Staudinger index of the solvent-solute pair.

Dilute silk protein solutions in 37,5 % glycerol-water mixtures show a distinct difference in necking behaviour compared to the pure solvent (figure 6.1). When imaged at very high frame rates (4000 frames per second), it is clearly visible that the purely newtonian solvent (left) undergoes rapid breakup of the fluid filament in two separated droplets, adhering to the separated plates. One can also observe the formation of a small satellite droplet, which is described to be associated with

In contrast, the dilute silk protein solution shows a distinct fluid filament formation process and shows capillary thinning (figure 6.1, right). It is therefore possible to extract polymer relaxation times from the time course of the mid-filament diameter. An elastocapillary force balance on a uniform cylindrical thread of radius  $R_1$  predicts that the filament radius decays exponentially in time [Rodd et al.,

## 6. Capillary Breakup: Rheology and Fiber formation

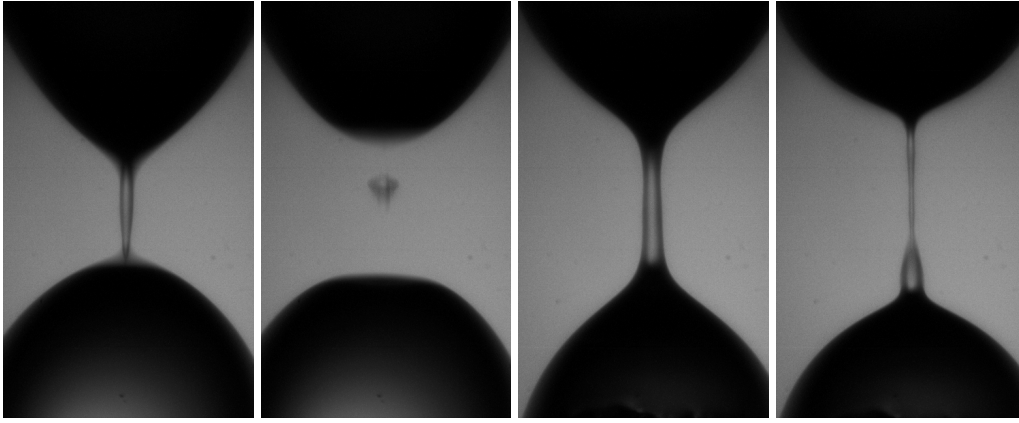


**Figure 6.1.:** Filament breakup of newtonian solvent (left two images) and dilute silk protein solution (right two images).

2005]:

$$\frac{R(t)}{R_1} = \left( \frac{GR_1}{2\sigma} \right)^{1/3} e^{-t/3\lambda} \quad (6.3)$$

The relaxation time for elongational stretching  $\lambda$  for dilute eADF3 in 37,5 % glycerol-water mixture was determined to be  $0.31 \pm 0.02$  ms according to figure 6.2.

Using equation 6.2, and with  $\eta_S = 4$  mPas for the glycerol-water mixture and with 1.0 mPas as the viscosity of water, this results in an extrapolated relaxation time in water of  $\lambda = 80 \mu s$ .

### 6.2.2. Elongational Rheology of Highly Concentrated Phase eADF3

A highly concentrated solution ( $> 150$  mg/ml) of eADF3 protein allows very easy fiber formation by a simple process: After placing a droplet of the spider silk protein solution in a 500 mM potassium phosphate solution, a fiber can directly be pulled out of the protein droplet by a pair of tweezers [Exler et al., 2007b]. The microscopic and molecular details of the described process are not understood, and it is unclear how the fiber is actually formed. However, it is clear that the tweezers exert a force on the droplet of silk protein that give rise to deformations that ultimately allow for a stable connection between the aggregated protein on the surface of the protein droplet and the tweezers.

In order to assess this phenomenon in a more quantitative way, highly concentrated eADF3 solutions were placed between the plates of the CABER setup. The protein solution droplet forms a stable fluid column between the plates which is kept in shape by the surface tension. Next, a 500 mM potassium phosphate so-

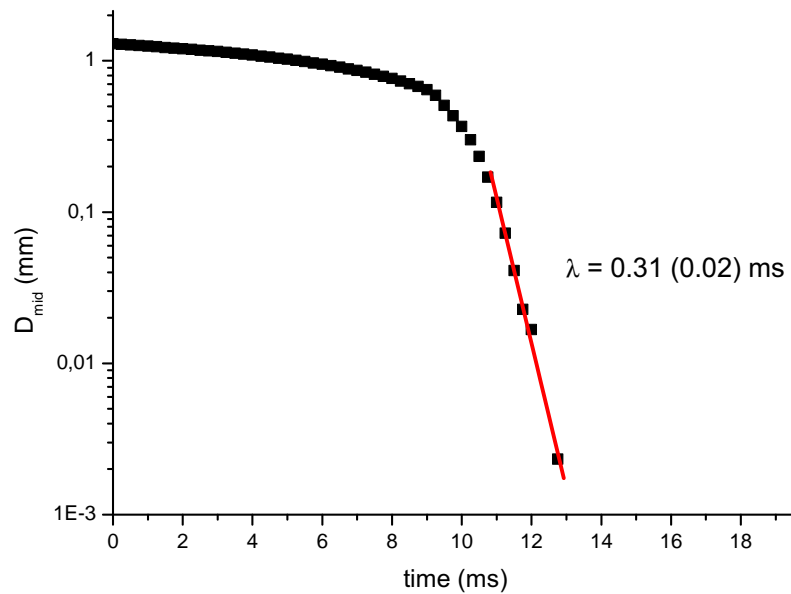


**Figure 6.2.:** Dilute solutions of eADF3 show an exponential decay of the mid filament diameter.

lution is pipetted around the protein solution column. After defined times, the salt droplet is drawn from the protein solution droplet by means of a pipette. Thus, with increased exposure time to the phosphate solution, different amounts of phosphate can diffuse into the protein solutions.

The experimental results show that the filament breakup times increase drastically with increasing interaction time with the phosphate solution. The effect is clearly visible in the apparent elongational viscosity, which is plotted in Figure 6.3. While for samples with no added phosphate no increase in the apparent elongational viscosity is observed, the very slow breakup dynamics of the samples after 3 minutes of exposure to phosphate show a very high increase of the apparent elongational viscosity with increasing strain  $H = \ln(D_m/D_0)$ .

When the eADF3 solution is left too long after addition of phosphate (more than 15 minutes), water evaporates and the material forms stringy ribbons spanning the space between the two plates (Figure 6.5).

Qualitatively, the apparent elongational viscosity for solutions of engineered spider silk with phosphate resembles the data obtained on natural spinning gland extracts (figure 6.4). This suggests that the spinning dope investigated in reference [Kojic et al., 2006] already contains the salt ions required for fiber forma-

## 6. Capillary Breakup: Rheology and Fiber formation

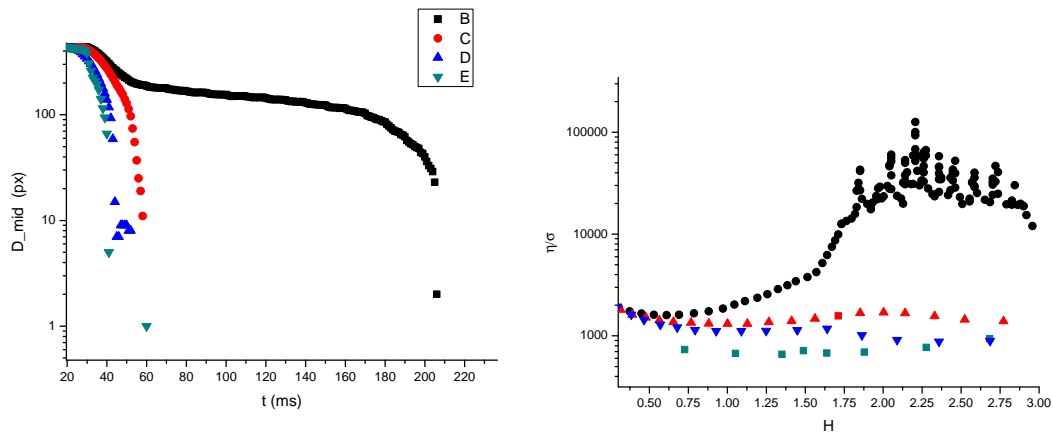


**Figure 6.3.:** Elongational Rheology of the viscous phase of eADF3 in aqueous solution.

tion. This illustrates the value of engineered silk solutions, where salt content and other non-proteinaceous contents can be carefully controlled and set in a well defined manner.

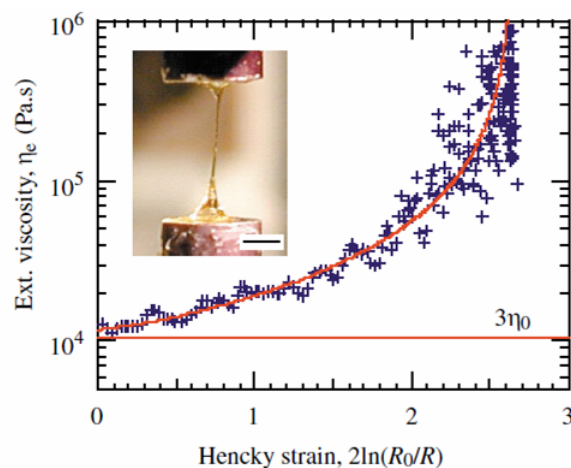


**Figure 6.4.:** Elongational rheology of silk gland extracts. Figure from [Kojic et al., 2006]. The elongational (extensional) viscosity increases strongly for large strains.

The absolute values of  $\eta_e$  observed for the engineered silk solutions are orders of magnitude lower than for the natural dope, which reflects the faster relaxation times in the engineered solution, which were already observed in chapter 5.4, and result from the lower protein concentration in the solutions of engineered proteins. Also, natural silk proteins have a larger molecular weight than the engineered silk proteins employed here (factor 2) and thus  $De$  is significantly larger for the natural silk proteins.

The relatively uncontrolled development of stringy ligaments from one plate

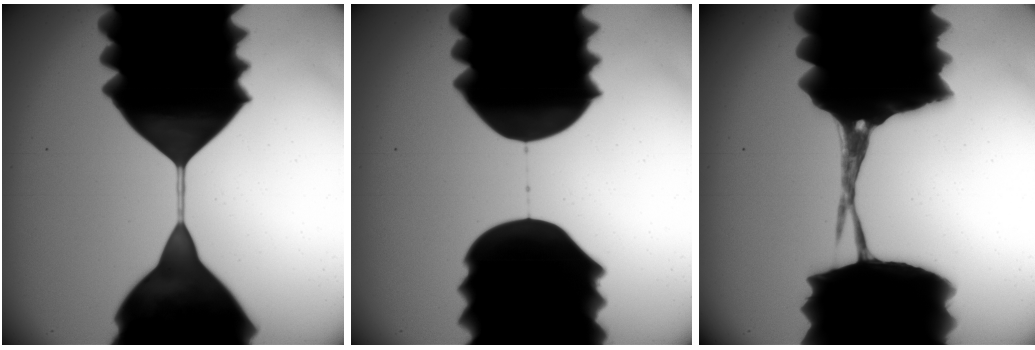


**Figure 6.5.:** Left: Without phosphate, eADF3 solutions flows until a rapidly decaying fluid filament develops. Middle: Under the influence of salt, stable filaments begin to form after the CABER experiment. Right: If the eADF3 solution is left too long after addition of phosphate, water evaporates and the material forms stringy ribbons spanning the space between the two plates.

to the other (Figure 6.5) could be overcome by placing a fine glass micropipette needle in the sample and allow the solvent to evaporate for 15 minutes. When the plates were then separated, a single fiber formed from the tip of the needle (Figure 6.6). However, it is difficult to interpret these observations, as the protein concentration in the sample is no longer known.

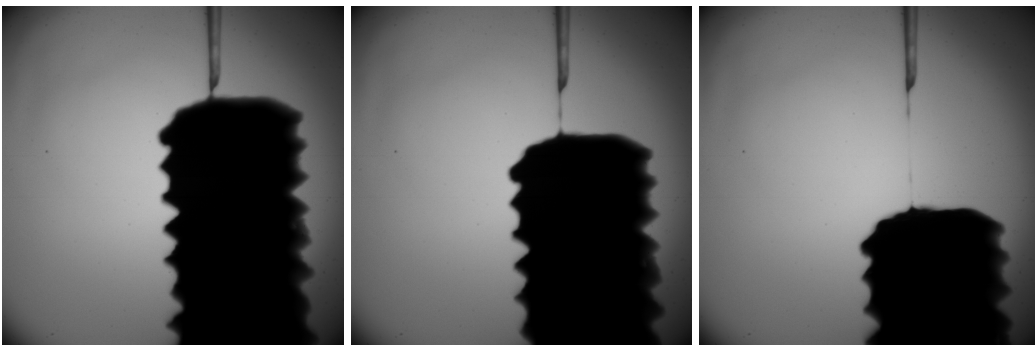


**Figure 6.6.:** Fiber formation from micropipette tip.

### 6.2.3. Discussion

Elongational flow experiments on eADF3 showed that the relaxation times even in diluted solutions were not much longer than 1 ms (figure 6.2). Thus, these solutions are on the very lower limit of the regime that allows to gain insights into elongational flow dynamics (figure 3.7). Therefore, in the next chapter, HFIP will be used as a solvent, which is able to swell the silk proteins better and thus allow more detailed studies of the fiber formation process and the underlying polymer dynamics.

## 6. Capillary Breakup: Rheology and Fiber formation

Solutions of eADF3 in the presence of phosphate ions were found to show an elongational viscosity increasing with Hencky strain. The elongational viscosity increase was stronger for samples that were exposed to phosphate for longer times. When phosphate was allowed to diffuse through the whole sample, the filament breakup curves were most similar to the ones obtained on natural silk gland extracts (Figure 6.4). In previous studies, it was suggested that the S-shaped spinning duct of spiders is optimized to allow for diffusion of phosphate ions through the whole duct [Vollrath and Knight, 2001, Jin and Kaplan, 2003]. Presumably, the growth of elongational viscosity with strain is important for fiber formation, as it reflects the molecular stretching of either individual silk proteins or preassembled aggregates.

These results show, that simulations of fiber formation up to now miss important aspects: Up to now, neither in the work presented here nor in the study by [Breslauer et al., 2009], elongational flow effects were actually taken into account to calculate the flow profiles in the spinning ducts. In both cases, only the shear thinning behaviour of spinning dopes was included in the models. In future studies, it would therefore be of outstanding interest to include the nontrivial, strain-dependent elongational viscosity of these fluids into the calculations.

### 6.3. eADF Rheology in nonaqueous solvents

Polymers assume different conformations depending on the quality of the solvent. Solvent 'quality' is defined as the capability of the solvent to swell the polymer chain. In a good solvent, the radius of gyration will be larger than in a bad solvent, where the polymer is collapsed.

As the C16 silk polymer was available in larger quantities than the other engineered spider silks, these studies could only be performed with C16. It is only soluble in water to less than 8 % wt/vol, so two different solvents were chosen: Hexafluoro-Isopropanol (HFIP) and Formic Acid (COOH). Their physical properties are shown in table 6.1.

These different solvents lead to different molecular conformations and thereby to different measured viscosities. The data is presented in graph 6.7. Both are much better solvents for C16 than water, resulting in an increased mean-square end-to-end distance of the polymers and thus a higher viscosity. It should be noted that for HFIP as well as COOH solvents, the data can be fitted excellently with an exponential growth function of the form  $\eta(c) = \eta_s \exp(ca)$ , where  $\eta_s$  is the viscosity of the respective solvent,  $c$  is the solute, and  $a$  is a parameter



	HFIP	COOH
Density (g/mL)	1.6	1.2
Melting Point (°C)	-3.3	8.4
Boiling Point (°C)	58	101
Viscosity at 20 °C (mPa s)	1.65	1.57
Polar/nonpolar	strongly polar	polar
miscible with water	yes	yes

**Table 6.1.:** Physical properties of HFIP and COOH

that describes how much the polymer swells in the respective solvent. Measured values for  $a$  were 27 ml/mg in formic acid and 45 ml/mg in HFIP.

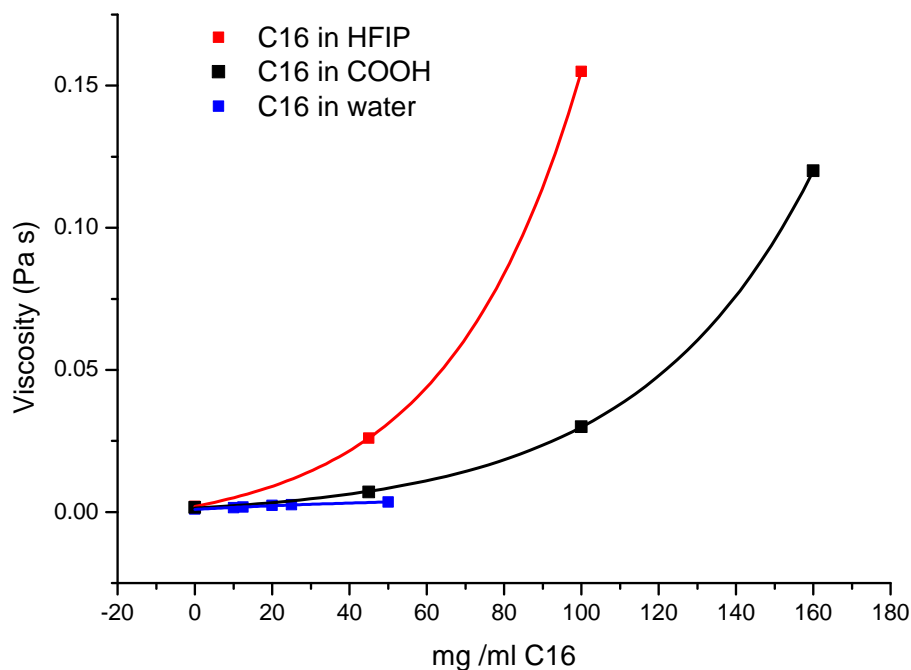


**Figure 6.7.:** Viscosity of C16 solutions in COOH and HFIP. In both solvents, the solubility of C16 is much higher. Both are much better solvents for C16 than water, resulting in an increased means-square end-to-end distance of the polymers and thus a higher viscosity.

Solutions of C16 in HFIP show a significantly higher viscosity at the same protein concentrations as in COOH. From this, we can conclude that HFIP is a better solvent for C16 and causes the protein to assume a conformation with a larger mean end-to-end distance.

For the assembly of silk fibers in free surface flow, which require a high protein

## 6. Capillary Breakup: Rheology and Fiber formation

solubility, HFIP is a better solvent than COOH, as it swells the protein more, therefore increasing the polymer relaxation times. For this reason, the assembly of silk fibers in free surface flow was attempted from HFIP solution 6.4.

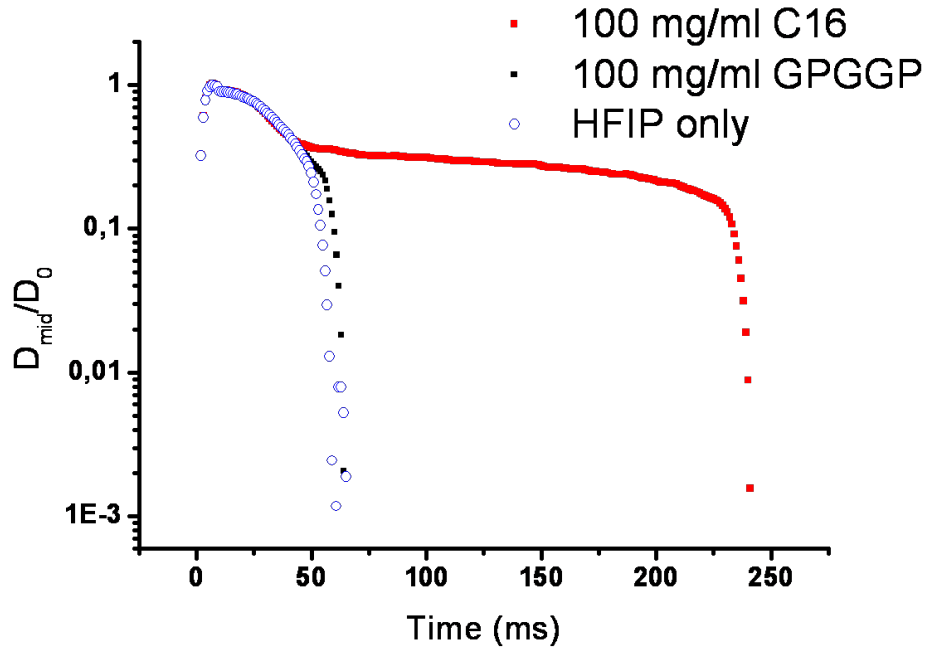


**Figure 6.8.:** Elongational Rheology of Engineered spider silk solutions in HFIP

As in the shear rheology experiments, the results of elongational rheometry are qualitatively similar to those obtained on silk gland extracts [Kojic et al., 2006].

It is important to distinguish effects from polymer dynamics from the aggregation properties of the repetitive sequences in the silk proteins. Thus, short fragments of the repetitive sequences were synthesized (see chapter 3.3.2), dissolved in HFIP and tested in the CABER setup.

As expected, solutions of short peptide fragments of silk proteins did not show a significant elongational viscosity and exposed short filament breakup times (Figure 6.8). Exemplarily, filament breakup curves of the pure HFIP solvent, a 100 mg/ml GPGGP solution, and a 100 mg/ml C16 solution are shown. Even if the mass concentration of protein material is the same in the latter two samples, the filament breakup time is drastically longer in the case of the C16 solution. This is solely due to elongational viscosity effects.

The longest eADFs, C32, was observed to show strong increase in elongational

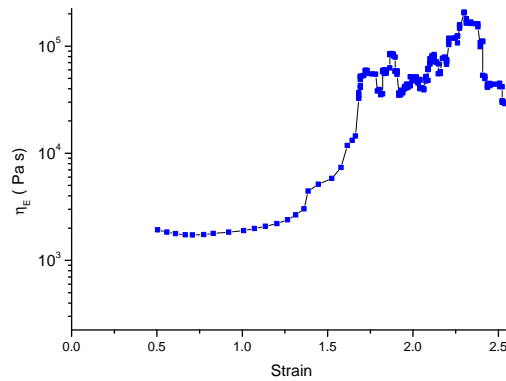


**Figure 6.9.:** Apparent Elongational Viscosity for C32 silk solution.

viscosity with increasing strain (figure 6.11) at 50 mg/ml concentration. At 100 mg/ml, it was even possible to induce a liquid-solid transition during the stretching process (chapter 6.4).

It was found that solutions containing engineered silk proteins show an increase of the apparent elongational viscosity with increasing strain (Figure 6.9). The qualitative behavior is very similar to the elongational viscosity of silk gland extracts (Figure 6.4), but the values for  $\eta_E$  observed for the engineered silk solutions are more than one magnitude smaller. This can probably be attributed to both the lower concentration of our solution and to the higher molecular mass of the natural silk proteins.

**Conclusions** From the shear viscosity studies, it was also concluded that HFIP is the better solvent for high concentrations of C16 than COOH, because the solution show a higher viscosity at the same protein concentration.

Rheological analysis of engineered silk protein solutions leads to two fundamental results: Firstly, the shear thinning that is observed for silk gland extracts is found to be similar in eADF solutions. This is of great importance for potential fiber production strategies from these engineered proteins. As has been shown for natural silk glands, the shear thinning behaviour reduces the pressure drop required to maintain the observed flow speeds in the silk gland (and thus the speed of fiber production) by a factor of 500 [Holland et al., 2006, Kojic et al., 2006].

Secondly, it was observed that at least highly concentrated solutions of C16 and C32 show a distinct elongational viscosity, which is much higher than the shear viscosity. Again, this behaviour of the simple solution of one eADF is remarkably similar to the elongational viscosity behaviour observed in natural silk

## 6. Capillary Breakup: Rheology and Fiber formation

gland extracts [Kojic et al., 2006]. It must be noted however, that the experiment depicted in figure 6.4 already led to a stable fiber, as can be seen by the diverging extensional viscosity for high strains. This is not the case for our data in figure 6.9.

### 6.4. Thread Formation

Thread formation can be described formally as the transition from a purely viscous fluid to a viscoelastic body.

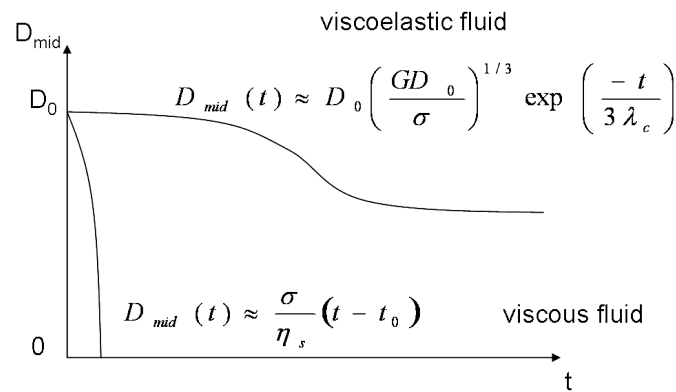


**Figure 6.10.:** Viscous fluids will break up after a finite time after a step strain. Viscoelastic fluids are able to maintain a finite  $D_{mid}$ .

The filament breakup times increased dramatically with increasing length of silk protein (figure 6.11) and increasing protein concentration.

Figure 6.11 shows that for C32 solutions at 50 mg/ml the necking dynamics are slowed down significantly, but the fluid filament breaks after about 240 ms. At 100 mg/ml however, the filament simultaneously strain hardens and undergoes evaporative drying. This leads to a complete halt of the necking process and leads to an axially uniform fiber. The apparent elongational viscosity diverges at this point (similar to figure 6.9) and the fluid thread ultimately dries to form a solid filament with a fixed diameter.

This effect can directly be attributed to the stretching of the C32 proteins in elongational flow. The C16 protein, which consists of exactly the same amino-acid sequence, just less repeats undergoes filament breakup at 100 mg/ml concentration (Figure 6.8). As the longest relaxation time for a polymer in the Rouse model scales with  $N^2$ , the Deborah number for the imposed step strain is much larger for C32 than for C16, giving rise to the aberrant behaviour and the formation fibers.

A similar behaviour has been studied for Polyethylene-oxide (PEO) solutions with extremely high molecular weight (2 MDa) [Sattler et al., 2008]. In this system, nanometer thin filaments of PEO were produced in CABER experiments.

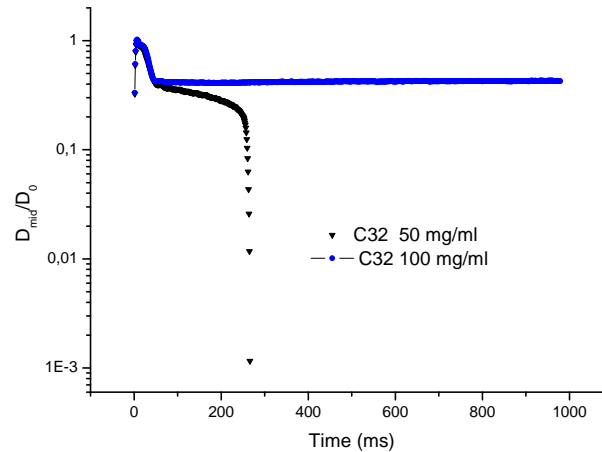


**Figure 6.11.:** At 100 mg/ml, C32 solution is viscous enough to form a stable fiber.

There is an important difference to the natural spinning process of silk: Dragline is spun under a constant force corresponding to the weight of the falling spider [Gosline et al., 1999], while in the capillary breakup experiment there is no externally imposed tension. This could explain in part why the filaments formed in our experiments are much thicker than natural silk, even if the solutions from which they were spun were much less viscous.

## 6.5. Mechanical properties of formed fibers

Both the molecular composition of fibers and the processing history are thought to influence the mechanical properties of the fibers [Vollrath et al., 2001].

In order to investigate the mechanical properties, pieces of the fibers were glued to paper frames, which were mounted on the extensiometer. After cutting the paper frame, the piece of fiber is fixed between the extensiometer fixtures and not supported by the carrier any more.

In general, mechanical properties of silk protein fiber depend strongly on the moisture content (relative humidity) of the surrounding air [Vehoff et al., 2007]. For natural spider silk, it was found that wetted silk fibers undergo a strong contraction process, termed 'supercontraction' [Shao and Vollrath, 1999, van Beek

## 6. Capillary Breakup: Rheology and Fiber formation

et al., 1999]. Supercontracted silk fibers are extensible up to three times as long as untreated fibers [Savage et al., 2004].

In order to assess the Extensional Stress  $\sigma = F/A$ , each fiber was analyzed in the microscope using a 100x objective with a numerical aperture of 1.4. This leads to a resolution of approximately  $1.1 \mu\text{m}$ .

### 6.6. Effect of Methanol treatment

The force curves of engineered Spider Silk reported in this thesis were obtained from eADF4 fibers spun from HFIP solution.

eADF4 fibers were found to be much less extensible than natural spider silk, and the stress at fracture was found to be similar to natural silk fibers treated with formadelhyde [Grabmayr, 2008]. This leads to the conclusion, that fibers from the engineered silk protein eADF4 contain too many intermolecular interactions, which makes them brittle.

Treatment with Methanol changed the mechanical properties significantly. Methanol induces a high content of  $\beta$ -sheets (see Appendix A), while the untreated Fibers contain mostly disordered secondary structure [Huemmerich et al., 2006, Rousseau et al., 2004, Slotta et al., 2006, Um et al., 2001]. As expected, the mechanical stability of fibers treated with methanol was higher than for untreated fibers. An increase in the stress at failure of about a factor 4 was observed (Figure 6.12).

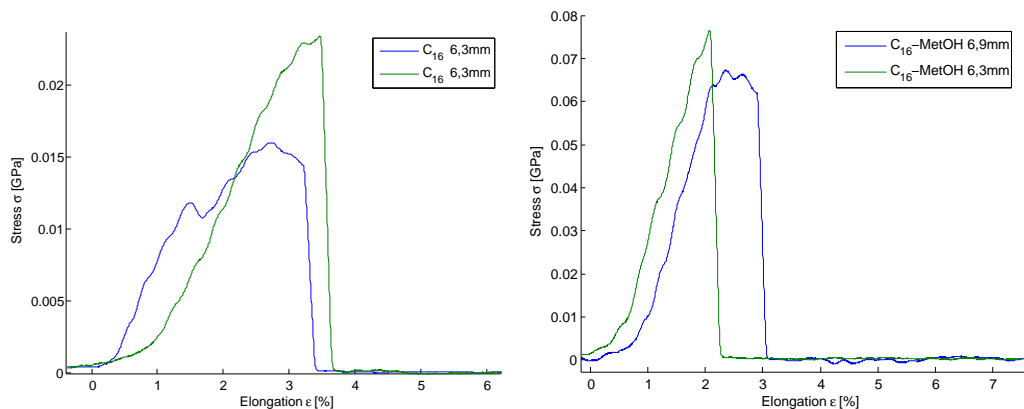


**Figure 6.12.:** Methanol increases the strength of the tested C16 fibers by a factor of approximately 4 (With H. Grabmayr).

## 6.7. Molecular Weight Dependence of the Mechanical Stability

To elucidate the question, whether the mechanical properties of silk fibers depend on the molecular weight of the proteins in the fiber, fibers from different length eADFs and of short fragments of eADFs were produced. Table 6.2 lists the respective protein contents:

Average Molecular Weight	Content
22	C16 + short peptides
44	C16
88	C16 + AQ24NR3
100	C32 + AQ24NR3

**Table 6.2.:** Constitution of fibers with different average molecular weight.

It was not possible to form stable fibers from a 150 mg/ml solution of any the short peptides. This is in accordance with the results from chapter 6.4, where it was shown that at this concentration only a polymer chain of the length of the C32 construct can form fibers, due the stretching of the polymers in the elongational flow.

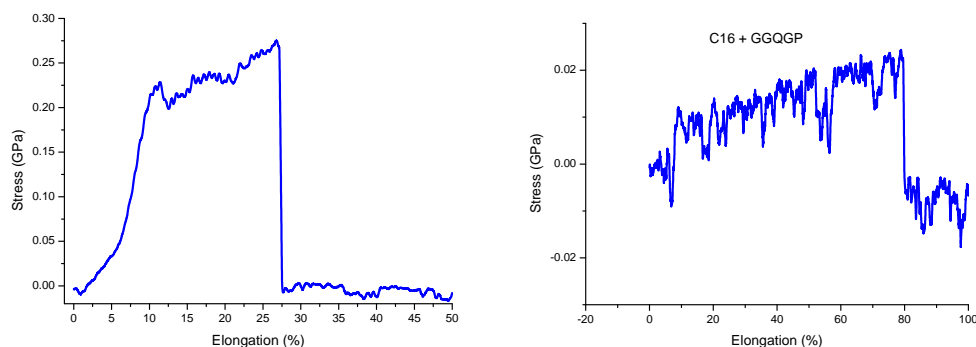


**Figure 6.13.:** Force-extension curves of engineered Spider Silk Protein fibers with different protein molecular weight. Left: C32+AQ24NR3 leads to a strong and tough fiber. Right: C16 with the short fragment GGQGP leads to a brittle fiber.

Fibers formed by C16 and a mixture of the short peptides were found to be extremely brittle. However, in some force curves it appears that up to 80 % deformation was achieved. This is probably an effect caused by the force that is generated by the sliding of two already broken parts of the fiber, against each other (Figure 6.13 ). From the movies recorded with the camera at 10x magnification, it is not possible to resolve this event. Thus, the data obtained from these solution is included in figure 6.14.

## 6. Capillary Breakup: Rheology and Fiber formation

The strongest fibers were formed by C32 and AQ24NR3 (Figure 6.13). Remarkably, force-extension curves of these fibers show not only a higher stress at fracture than C16 fibers, but also a plateau region, where the force almost does not increase any more. This region could be explained with small domains of the fiber breaking and relaxation processes taking place subsequently.

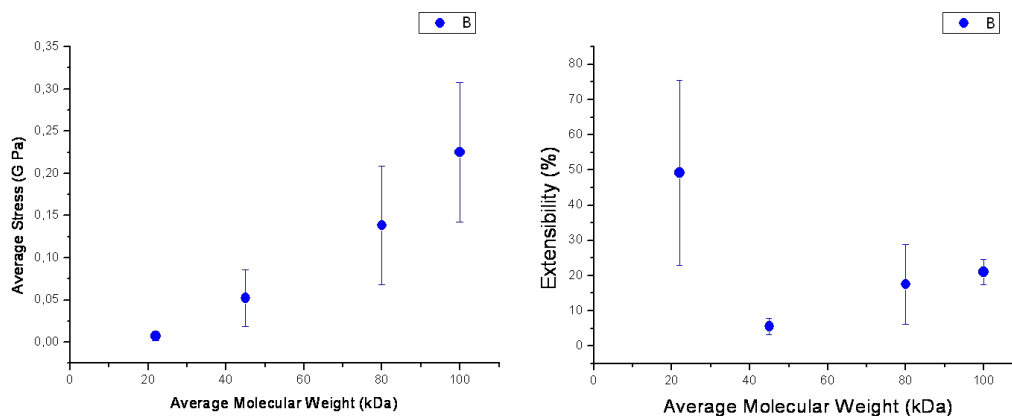


**Figure 6.14.:** Left: Stress at rupture increases with increasing average molecular weight for fibers spun from HFIP solutions. Right: Extensibility also increases with average molecular weight.

The stress at failure increased approximately linear with the average molecular weight for the samples tested. The number of samples was  $N=10$  for each molecular weight, and the error bars in Figure 6.14 give the standard deviation.

The observed increase of the stress at failure with increasing average molecular mass can be explained in a very simple way: if one considers the protein in the fiber to be partially oriented along the axis of the fiber, and estimates the minimal number of hydrogen bonds, that have to rupture, one finds that for longer oriented polymers the average number of bonds that have to break is larger than for short proteins (Figure 6.15). Also, the effect of molecular alignment gets stronger with increasing molecular weight. The accumulated strain during fiber formation was the same for all samples, so the Deborah number  $De = \tau_R/t_p$  is significantly larger for the longer proteins.

For future studies, it will be essential to investigate in detail not only the effect of the molecular weight of the proteins but to also study in detail the influence of protein type (e.g. eADF3 or 4).



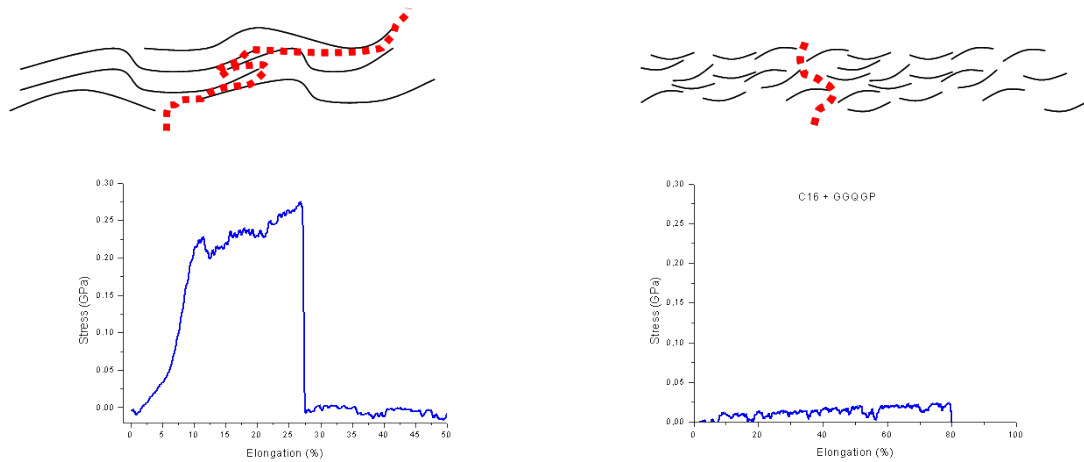


**Figure 6.15.:** In a fiber made of long, oriented molecules interconnected by hydrogen bonds, the average number of bonds that must be broken to rupture the fiber is higher than for a fiber consisting of short molecules.

## 6.8. Natural Spider Silk

In order to be sure that the measurements on synthetic silk fibers are in accordance with results previously published on natural silk fibers, final experiments were carried out with natural silk fibers.

Silk fibers obtained from a Garden Spider (*Araneus diadematus*) were coiled around a plastic frame, and 5 cm pieces of this fiber were cut with scissors. After gluing these pieces to paper frames, the length of each fiber was determined using a caliper.

The results show that the experimental setup constructed can reproduce the mechanical properties of spider silk as published previously. In figure 6.16 one can even see that the dragline silk consists actually of two fibers that are wound around each other.

At low deformations, spider silk behaves like an elastic solid 6.16. In the initial deformation range, no creep upon the imposition of stress is observed. This is in accordance to other studies on spider dragline silk [Vehoff et al., 2007].

When immersed in water, spider silk undergoes a change called supercontraction (see 2.3). In figure 6.18, a force extension curve of a supercontracted silk fiber is shown. This fiber was mounted in the fiber tester, then the distance between sensor and moving stage was reduced to 20 % of the original distance, so that the mounted fiber had a lot of slack. The fiber was then gently rinsed with water from a pipette. After waiting for an hour, the force extension curve was obtained. Notably, the stress at failure is comparable to that of the dry fiber, but the shape

## 6. Capillary Breakup: Rheology and Fiber formation

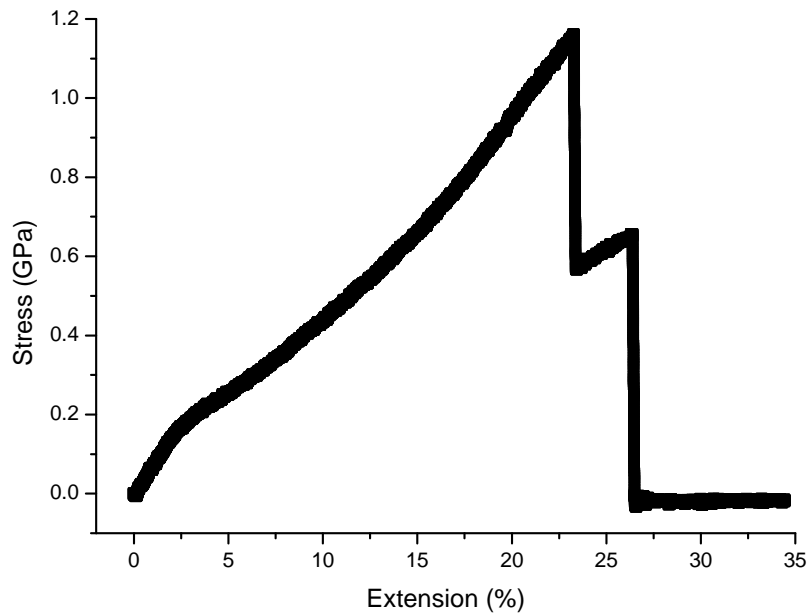


**Figure 6.16.:** Force extension curve of natural dragline silk.

of the force extension curve is completely different.

If one includes information on natural spider silk in the plot of maximum observed stress 6.19, remarkably the values found for natural silk represent a linear extrapolation of the values found for the short fragments. This extrapolation should however be considered critically, as the properties of natural silk fibers vary quite strongly from animal to animal and on the speed of forced silk-spinning [Madsen et al., 1999]. However, the qualitative relation is encouraging efforts to improve engineered silk fibers towards the performance of natural silks.

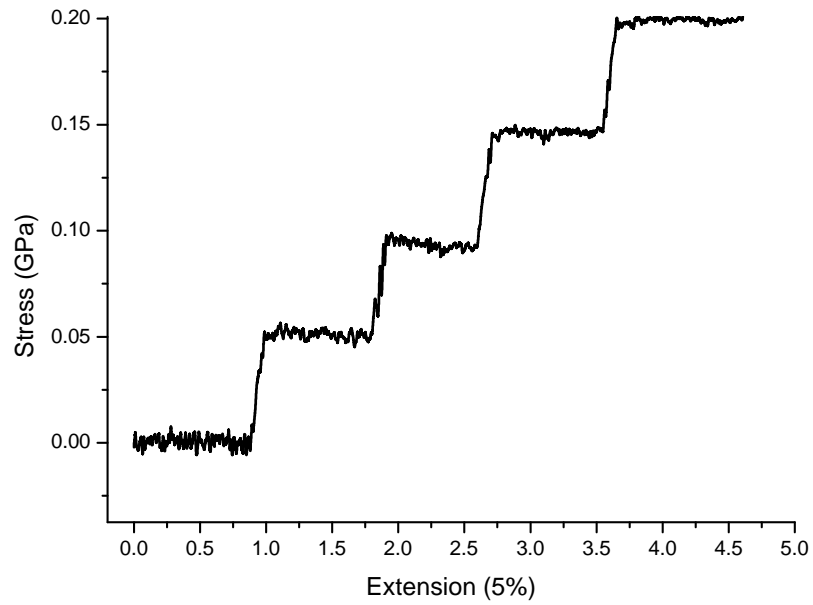


**Figure 6.17.:** At low extension, dragline silk shows no creep or hysteresis.

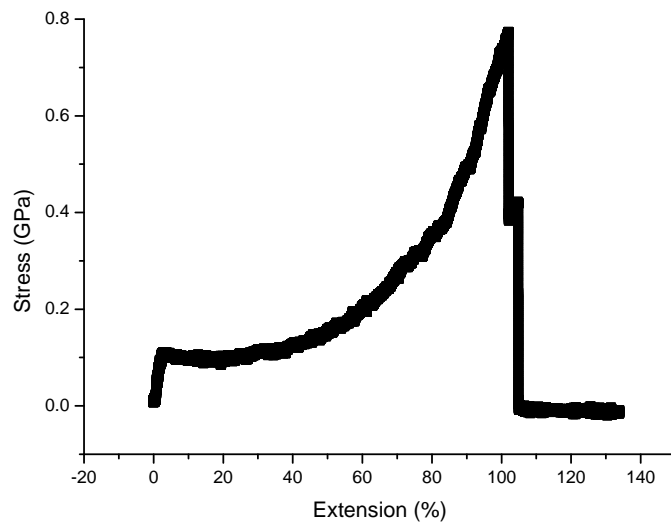


**Figure 6.18.:** Wetted spider silk undergoes supercontraction and is much more extensible than untreated silk.

## 6. Capillary Breakup: Rheology and Fiber formation

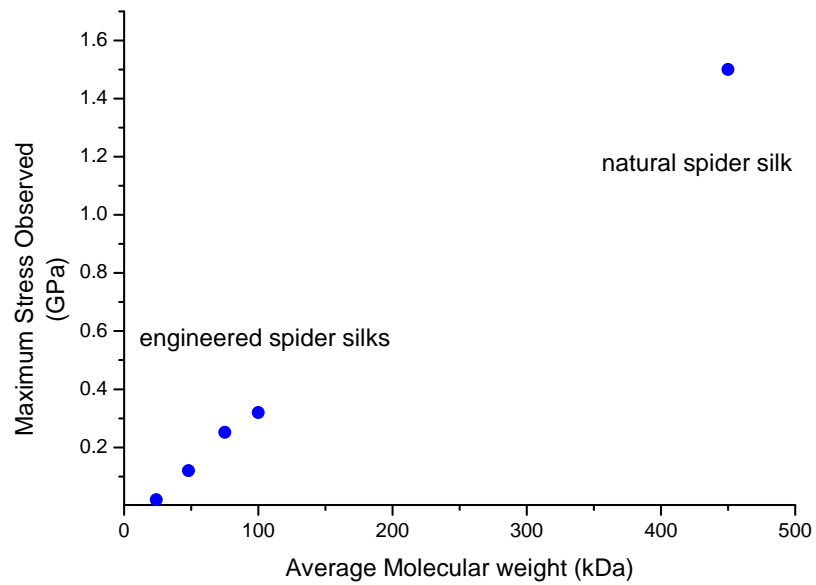


**Figure 6.19.:** If the stability of engineered spider silk is linearly extrapolated, one would very precisely end with the actually observed mechanical stability of spider silk. One has to take into account though, that the engineered fibers referred to here are drawn by hand and their properties could probably enhanced further.

## 7. Discussion and Outlook

Assembly of spider silk was studied in microfluidic devices, which led to new insights into the temporal and spatial organization of silk fiber formation. Elongational flow was identified to be a prerequisite of fiber formation.

In order to assess the rheological properties of the highly non-newtonian silk solutions in elongational flow, capillary breakup rheology experiments have been performed. It was shown that under the influence of phosphate ions, the elongational viscosity of engineered silk solutions approaches that of natural spinning dopes extracted from spiders.

Finally, the mechanical properties of fibers formed from engineered spider silk were related to the average molecular weight of the constituting proteins and compared to the properties of natural spider silk.

In summary, we were able to determine the physical mechanism for fiber formation in spiders. Our results in the microfluidic channels are in good agreement with the model of silk formation in insects as proposed by Jin and Kaplan [Jin and Kaplan, 2003].

It was observed that colloidal aggregates are a prerequisite for fiber formation. The pre-aggregation leading to micrometer-sized aggregates is necessary to allow shear-induced fiber assembly [Squires and Quake, 2005]. Once the particles come into contact, their attractive interaction is highly important. Since the interaction between the eADF4 spherical aggregates is not sufficiently attractive, fiber formation of ADF4 does not occur. Importantly, only protein solutions of low or medium concentration have been employed in the microfluidic channels in this study, indicating that liquid crystalline behavior of the spinning dope is not a necessary prerequisite for fiber spinning under the conditions tested.

However, high flow rates are necessary in our system to induce fiber assembly. In nature, extremely high protein concentrations and thus dramatically increased viscosities enable fiber formation already at much lower elongational flow rates.

The presented approach combining modular microfluidics devices and protein engineering is a promising route to gain further insights into silk and other protein aggregation processes.

## 7. Discussion and Outlook

Taken together, the following points could be achieved:

- Microfluidic devices can be utilized to assemble engineered spider silk proteins into fibers, while enabling the direct observation of the process by various microscopic techniques. For optical techniques, PDMS-based microfluidics was shown to be sufficiently transparent and accessible for all methods used, including immersion oil microscopy and fluorescence imaging.
- Using Finite Element Simulations, it could be shown that the flow profile in the microfluidic channels, in which fiber formation was observed, is mostly of elongational nature.
- Engineered Spider silks, which can be produced in bacteria and are purified, can serve as a valuable model to study the natural spinning process. The most prominent advantage of using engineered silks is their availability in research grade purity, with exactly known salt concentrations. This is a great advantage compared to studying extracts from natural silk glands.
- Our observations and previous studies lead to the notion that rheological properties of the spinning dopes play a central role in the fiber formation process. Since elongational viscosity was regarded to be the most important rheological property in this context, the elongational behavior of various spider silk solutions was investigated.
- Finally, initial relations between engineered silk polymer length and fiber stability could be established.

In future, the results obtained will be helpful to develop valuable applications for engineered silk fibers. Using engineered silk proteins to produce fibers provides new opportunities to incorporate functionalities directly into the fibers [Scheibel, 2004]. For instance, it is possible to introduce new functionalities by editing the amino acid sequence of the fiber forming proteins. These new properties could be, but are not limited to: Chemically reactive sites (enzymes), antimicrobial properties, dyes, cell attachment sites, and biodegradation sites.

Together with knowledge on the fundamental principles of fiber assembly, the ability to tune the fibers properties on the molecular level will open many new applications of spider silk:

Due to the high costs in early stages, initial applications will be most likely in the medical field. Possible applications could be wound closure systems or extremely thin sutures for neurosurgery. Natural spider silk fibers have been

successfully employed as guidance systems for peripheral nerve regeneration [Allmeling et al., 2008].

Since spider silks are produced at low pressures, room temperature and in aqueous solution, it might also be possible to include living cells in the fiber formation process and generate fibers that are covered with cells.

Strategies to further improve the properties of spider silk are also developed. It is a scientifically exciting and commercially interesting question, whether it will be possible to produce fibers which are stronger than natural spider's. The strategies to improve the strength of silk fibers can be classified in four groups:

1. Optimization of the silk's amino acid sequence. This might be difficult, as the sequences of silk genes seem to be very well conserved. Thus, there might not be much progress possible with this approach.
2. Combination of silk proteins with biomineralization. In this approach, the properties of silk fibers could be combined with the useful properties of mineralic materials, such as bone. Some studies have already successfully produced fusion genes of silk fibroin and silica mineralization proteins [Foa et al., 2006].
3. Optimizations in the spinning process. By adopting the natural spinning process, it might be possible to produce fibers that are specifically useful for a given application. For instance, a fiber with a given moisture content for use in a well-defined environment could be produced.
4. Treatment of formed fibers with cross-linking agents or other additives. We have shown that treatment with methanol increases the strength for fibers made from eADF4. Other compounds that could be used to increase the strength of engineered and natural silk fibers are metal ions. A great increase in the strength of natural silk fibers after treatment with metal-ion vapor was reported [Lee et al., 2009].

The mentioned challenges and questions in studying the production, assembly and application of spider silk are of great diversity. Thus, it is essential that scientists from mutually complementary fields such as biochemistry, biotechnology, chemical engineering, polymer physics and others work together on these fascinating questions.





## Bibliography

- [Allmeling et al., 2008] Allmeling, C., Jokuszies, A., Reimers, K., Kall, S., Choi, C. Y., Brandes, G., Kasper, C., Scheper, T., Guggenheim, M., and Vogt, P. M. (2008). Spider silk fibres in artificial nerve constructs promote peripheral nerve regeneration. *Cell Prolif*, 41(3):408–420.
- [Babcock et al., 2003] Babcock, H. P., Teixeira, R. E., Hur, J. S., Shaqfeh, E. S. G., and Chu, S. (2003). Visualization of molecular fluctuations near the critical point of the coil-stretch transition in polymer elongation. *Macromolecules*, 36(12):4544–4548.
- [Bird et al., 1987] Bird, R., Armstrong, R., and Hassager, O. (1987). *Dynamics of polymeric liquids 1 - Fluid Mechanics*. John Wiley & Sons, 2nd edition.
- [Breslauer et al., 2009] Breslauer, D. N., Lee, L. P., and Muller, S. J. (2009). Simulation of flow in the silk gland. *Biomacromolecules*, 10(1):49–57.
- [Byler and Susi, 1986] Byler, D. and Susi, H. (1986). Examination of the secondary structure of proteins by deconvolved ftir spectra. *Biopolymers*, 25:469–487.
- [Chen et al., 2002] Chen, X., Knight, D. P., and Vollrath, F. (2002). Rheological characterization of nephila spidroin solution. *Biomacromolecules*, 3(4):644–648.
- [Chu et al., 1995] Chu, S., Quake, S., Perkins, T., and Smith, D. (1995). Polymer experiments on single dna-molecules. *Abstracts of Papers of the American Chemical Society*, 209:374–PHYS.
- [Clemen et al., 2005] Clemen, A. E.-M., Vilfan, M., Jaud, J., Zhang, J., Bärmann, M., and Rief, M. (2005). Force-dependent stepping kinetics of myosin-v. *Biophys J*, 88(6):4402–4410.
- [Corporation, 2003] Corporation, T. E. (2003). *Instruction Manual Haake CaBER 1*.
- [Doi and Edwards, 1986] Doi, M. and Edwards, S. (1986). *The Theory of Polymer Dynamics*. Oxford university Press.
- [Dontula et al., 1997] Dontula, P., Pasquali, M., Scriven, L., and Macosko, C. (1997). Can extensional viscosity be measured with opposed-nozzle devices? *Rheol Acta*, 36:429–448.
- [Doyle et al., 1998] Doyle, P. S., Shaqfeh, E. S. G., McKinley, G. H., and Spiegelberg, S. H. (1998). Relaxation of dilute polymer solutions following extensional flow. *Journal of Non-Newtonian Fluid Mechanics*, 76(1-3):79–110.

## Bibliography

- [Edmond et al., 2006] Edmond, K. V., Schofield, A. B., Marquez, M., Rothstein, J. P., and Dinsmore, A. D. (2006). Stable jets of viscoelastic fluids and self-assembled cylindrical capsules by hydrodynamic focusing. *Langmuir*, 22(21):9052–6.
- [Exler et al., 2007a] Exler, J., Huemmerich, D., and Scheibel, T. (2007a). The amphiphilic properties of spider silks are important for spinning. *Angewandte Chemie-International Edition*, 46(19):3559–3562.
- [Exler et al., 2007b] Exler, J. H., Hümmerich, D., and Scheibel, T. (2007b). The amphiphilic properties of spider silks are important for spinning. *Angew Chem Int Ed Engl*, 46(19):3559–3562.
- [Foo et al., 2006] Foo, C. W. P., Patwardhan, S. V., Belton, D. J., Kitchel, B., Anastasiades, D., Huang, J., Naik, R. R., Perry, C. C., and Kaplan, D. L. (2006). Novel nanocomposites from spider silk-silica fusion (chimeric) proteins. *Proceedings of the National Academy of Sciences of the United States of America*, 103(25):9428–9433.
- [Fudge et al., 2003] Fudge, D., Gardner, K., Forsyth, V., Riekkel, C., and Gosline, J. (2003). The mechanical properties of hydrated intermediate filaments: Insights from hagfish slime threads. *Biophysical Journal*, 85(3):2015–2027.
- [Fuller et al., 1987] Fuller, G., Cathey, C., Hubbard, B., and Zebrowski, B. (1987). Extensional viscosity measurements for low viscosity fluids. *Journal of Rheology*, 31:235–249.
- [Gasteiger et al., 2005] Gasteiger, E., Hoogland, C., Gattiker, A., S, D., Wilkins, M., Appel, R., and Bairoch, A. (2005). *Protein Identification and Analysis Tools on the ExPASy Server; in: The Proteomics Protocols Handbook*. Humana Press.
- [Gebhardt et al., 2006] Gebhardt, J. C. M., Clemen, A. E.-M., Jaud, J., and Rief, M. (2006). Myosin-v is a mechanical ratchet. *Proc Natl Acad Sci U S A*, 103(23):8680–8685.
- [Geisler et al., 2008] Geisler, M., Pirzer, T., Ackerschott, C., Lud, S., Garrido, J., Scheibel, T., and Hugel, T. (2008). Hydrophobic and Hofmeister effects on the adhesion of spider silk proteins onto solid substrates: An AFM-based single-molecule study. *Langmuir*, 24(4):1350–1355.
- [Glisovic et al., 2008] Glisovic, A., Vehoff, T., Davies, R. J., and Salditt, T. (2008). Strain dependent structural changes of spider dragline silk. *Macromolecules*, 41(2):390–398.
- [Gosline et al., 1999] Gosline, J. M., Guerette, P. A., Ortlepp, C. S., and Savage, K. N. (1999). The mechanical design of spider silks: from fibroin sequence to mechanical function. *J Exp Biol*, 202(Pt 23):3295–3303.

- [Grabmayr, 2008] Grabmayr, H. (2008). Molekulare orientierung in natürlicher und künstlicher spinnenseide. Master's thesis, Technische Universität München.
- [Guery et al., 2006] Guery, J., Bertrand, E., Rouzeau, C., Levitz, P., Weitz, D. A., and Bibette, J. (2006). Irreversible shear-activated aggregation in non-brownian suspensions. *Physical Review Letters*, 96(19):198301.
- [Hagn et al., 2009] Hagn, F., Eisoldt, L., Hardy, J., Vendrely, C., M, C., Scheibel, T., and Kessler, H. (2009). The carboxy-terminal non-repetitive domain of a spider dragline silk protein regulates nucleation of silk assembly. *in preparation*.
- [Heim et al., 2009] Heim, M., Keerl, D., and Scheibel, T. (2009). Spider silk: From soluble protein to extraordinary fiber. *Angew Chem Int Ed Engl*, 48:2–15.
- [Hellmich et al., 2005] Hellmich, W., Regtmeier, J., Duong, T. T., Ros, R., Anselmetti, D., and Ros, A. (2005). Poly(oxyethylene) based surface coatings for poly(dimethylsiloxane) microchannels. *Langmuir*, 21(16):7551–7557.
- [Hermanson et al., 2007] Hermanson, K., Huemmerich, D., Scheibel, T., and Bausch, A. (2007). Engineered microcapsules fabricated from reconstituted spider silk. *Advanced Materials*, 19(14):1810–1815.
- [Holland et al., 2006] Holland, C., Terry, A. E., Porter, D., and Vollrath, F. (2006). Comparing the rheology of native spider and silkworm spinning dope. *Nature Materials*, 5(11):870–874.
- [Horinek et al., 2008] Horinek, D., Serr, A., Geisler, M., Pirzer, T., Slotta, U., Lud, S. Q., Garrido, J. A., Scheibel, T., Hugel, T., and Netz, R. R. (2008). Peptide adsorption on a hydrophobic surface results from an interplay of solvation, surface, and intrapeptide forces. *Proceedings of the National Academy of Sciences U.S.A.*, 105(8):2842–2847.
- [Howard, 2001] Howard, J. (2001). Mechanics of motor proteins and the cytoskeleton.
- [Huemmerich et al., 2004a] Huemmerich, D., Helsen, C. W., Quedzuweit, S., Oschmann, J., Rudolph, R., and Scheibel, T. (2004a). Primary structure elements of spider dragline silks and their contribution to protein solubility. *Biochemistry*, 43(42):13604–13612.
- [Huemmerich et al., 2004b] Huemmerich, D., Helsen, C. W., Quedzuweit, S., Oschmann, J., Rudolph, R., and Scheibel, T. (2004b). Primary structure elements of spider dragline silks and their contribution to protein solubility. *Biochemistry*, 43(42):13604–13612.
- [Huemmerich et al., 2004c] Huemmerich, D., Scheibel, T., Vollrath, F., Cohen, S., Gat, U., and Ittah, S. (2004c). Novel assembly properties of recombinant spider dragline silk proteins. *Current Biology*, 14(22):2070–2074.

## Bibliography

- [Huemmerich et al., 2006] Huemmerich, D., Slotta, U., and Scheibel, T. (2006). Processing and modification of films made from recombinant spider silk proteins. *Applied Physics a-Materials Science & Processing*, 82(2):219–222.
- [Husband and Adams, 1992] Husband, J. and Adams, J. (1992). Shear induced aggregation of carboxylated polymer latices. *Colloid and Polymer Science*, 270(12):1194–1200.
- [Jelinski, 1998] Jelinski, L. (1998). Establishing the relationship between structure and mechanical function in silks. *Current Opinion in Solid State & Materials Science*, 3(3):237–245.
- [Jin and Kaplan, 2003] Jin, H. and Kaplan, D. (2003). Mechanism of silk processing in insects and spiders. *Nature*, 424(6952):1057–1061.
- [Keten and Buehler, 2008] Keten, S. and Buehler, M. J. (2008). Geometric confinement governs the rupture strength of h-bond assemblies at a critical length scale. *Nano Lett*, 8(2):743–748.
- [Knight et al., 2000] Knight, D. P., Knight, M. M., and Vollrath, F. (2000). Beta transition and stress-induced phase separation in the spinning of spider dragline silk. *International Journal of Biological Macromolecules*, 27(3):205–210.
- [Kojic et al., 2006] Kojic, N., Bico, J., Clasen, C., and McKinley, G. H. (2006). Ex vivo rheology of spider silk. *Journal of Experimental Biology*, 209(21):4355–4362.
- [Kojic et al., 2004] Kojic, N., Kojic, M., Gudlavalleti, S., and McKinley, G. (2004). Solvent removal during synthetic and nephila fiber spinning. *Biomacromolecules*, 5(5):1698–1707.
- [Kummerlen et al., 1996] Kummerlen, J., vanBeek, J. D., Vollrath, F., and Meier, B. H. (1996). Local structure in spider dragline silk investigated by two-dimensional spin-diffusion nuclear magnetic resonance. *Macromolecules*, 29(8):2920–2928.
- [Lammel et al., 2008] Lammel, A., Schwab, M., Slotta, U., Winter, G., and Scheibel, T. (2008). Processing conditions for the formation of spider silk microspheres. *ChemSusChem*, 1(5):413–416.
- [Lee et al., 2007] Lee, J. S., Dylla-Spears, R., Teclemariam, N. P., and Muller, S. J. (2007). Microfluidic four-roll mill for all flow types. *Applied Physics Letters*, 90(7).
- [Lee et al., 2009] Lee, S.-M., Pippel, E., Gösele, U., Dresbach, C., Qin, Y., Chandran, C. V., Bräuniger, T., Hause, G., and Knez, M. (2009). Greatly increased toughness of infiltrated spider silk. *Science*, 324(5926):488–492.
- [Lefevre et al., 2007] Lefevre, T., Rousseau, M. E., and Pezolet, M. (2007). Protein secondary structure and orientation in silk as revealed by raman spectromicroscopy. *Biophys J*, 92(8):2885–95.

- [Madsen et al., 1999] Madsen, B., Shao, Z. Z., and Vollrath, F. (1999). Variability in the mechanical properties of spider silks on three levels: interspecific, intraspecific and intraindividual. *International Journal of Biological Macromolecules*, 24(2-3):301–306.
- [Marrucci et al., 1993] Marrucci, G., Bhargava, S., and Cooper, S. L. (1993). Models of shear-thickening behavior in physically cross-linked networks. *Macromolecules*, 26(24):6483–6488.
- [Martel et al., 2008] Martel, A., Burghammer, M., Davies, R. J., Di Cola, E., Vendrely, C., and Riekel, C. (2008). Silk Fiber Assembly Studied by Synchrotron Radiation SAXS/WAXS and Raman Spectroscopy. *Journal of the American Chemical Society*, 130(50):17070–17074.
- [Matsumoto et al., 2008] Matsumoto, A., Lindsay, A., Abedian, B., and Kaplan, D. L. (2008). Silk fibroin solution properties related to assembly and structure. *Macromol Biosci*, 8(11):1006–1018.
- [McDonald et al., 2000] McDonald, J. C., Duffy, D. C., Anderson, J. R., Chiu, D. T., Wu, H. K., Schueller, O. J. A., and Whitesides, G. M. (2000). Fabrication of microfluidic systems in poly(dimethylsiloxane). *Electrophoresis*, 21(1):27–40.
- [McDonald et al., 2001] McDonald, J. C., Metallo, S. J., and Whitesides, G. M. (2001). Fabrication of a configurable, single-use microfluidic device. *Analytical Chemistry*, 73(23):5645–5650.
- [McDonald and Whitesides, 2002] McDonald, J. C. and Whitesides, G. M. (2002). Poly(dimethylsiloxane) as a material for fabricating microfluidic devices. *Accounts of Chemical Research*, 35(7):491–499.
- [Munishkina et al., 2004] Munishkina, L. A., Henriques, J., Uversky, V. N., and Fink, A. L. (2004). Role of protein-water interactions and electrostatics in alpha-synuclein fibril formation. *Biochemistry*, 43(11):3289–3300.
- [Peng et al., 2005] Peng, X. N., Shao, Z. Z., Chen, X., Knight, D. P., Wu, P. Y., and Vollrath, F. (2005). Further investigation on potassium-induced conformation transition of nephila spidroin film with two-dimensional infrared correlation spectroscopy. *Biomacromolecules*, 6(1):302–308.
- [Perkins et al., 1994] Perkins, T. T., Quake, S. R., Smith, D. E., and Chu, S. (1994). Relaxation of a single dna molecule observed by optical microscopy. *Science*, 264(5160):822–826.
- [Porter and Vollrath, 2009] Porter, D. and Vollrath, F. (2009). Silk as a biomimetic ideal for structural polymers. *Angew Chem Int Ed Engl*, 21:487 – 492.
- [Porter et al., 2005] Porter, D., Vollrath, F., and Shao, Z. (2005). Predicting the mechanical properties of spider silk as a model nanostructured polymer. *European Physical Journal E*, 16(2):199–206.

## Bibliography

- [Rammensee et al., 2006] Rammensee, S., Huemmerich, D., Hermanson, K. D., Scheibel, T., and Bausch, A. R. (2006). Rheological characterization of hydrogels formed by recombinantly produced spider silk. *Applied Physics a-Materials Science & Processing*, 82(2):261–264.
- [Rodd et al., 2005] Rodd, L., Scott, T., Cooper-White, J., and McKinley, G. (2005). Capillary break-up rheometry of low-viscosity elastic fluids. *Applied Rheology*, 15(1):12–27.
- [Rousseau et al., 2006] Rousseau, M. E., Beaulieu, L., Lefevre, T., Paradis, J., Asakura, T., and Pezolet, M. (2006). Characterization by raman microspectroscopy of the strain-induced conformational transition in fibroin fibers from the silkworm *Samia cynthia ricini*. *Biomacromolecules*, 7(9):2512–2521.
- [Rousseau et al., 2004] Rousseau, M. E., Lefevre, T., Beaulieu, L., Asakura, T., and Pezolet, M. (2004). Study of protein conformation and orientation in silkworm and spider silk fibers using raman microspectroscopy. *Biomacromolecules*, 5(6):2247–57.
- [Rubinstein and Colby, 2003] Rubinstein, M. and Colby, R. (2003). *Polymer Physics*. Oxford University Press.
- [Ruppert et al., 2004] Ruppert, E., Fox, R., and Barnes, R. (2004). *Invertebrate Zoology: A Functional Evolutionary Approach, 7th Edition*. Brooks/Cole.
- [Sapede et al., 2005] Sapede, D., Seydel, T., Forsyth, V. T., Koza, M. A., Schweins, R., Vollrath, F., and Riekkel, C. (2005). Nanofibrillar structure and molecular mobility in spider dragline silk. *Macromolecules*, 38(20):8447–8453.
- [Sattler et al., 2008] Sattler, R., Wagner, C., and Eggers, J. (2008). Blistering pattern and formation of nanofibers in capillary thinning of polymer solutions. *Phys Rev Lett*, 100(16):164502.
- [Savage and Gosline, 2008] Savage, K. N. and Gosline, J. M. (2008). The role of proline in the elastic mechanism of hydrated spider silks. *J Exp Biol*, 211(Pt 12):1948–1957.
- [Savage et al., 2004] Savage, K. N., Guerette, P. A., and Gosline, J. M. (2004). Supercontraction stress in spider webs. *Biomacromolecules*, 5(3):675–679.
- [Scheibel, 2004] Scheibel, T. (2004). Spider silks: recombinant synthesis, assembly, spinning, and engineering of synthetic proteins. *Microb Cell Fact*, 3(1):14.
- [Scheibel, 2005a] Scheibel, T. (2005a). Protein fibers as performance proteins: new technologies and applications. *Curr Opin Biotechnol*, 16(4):427–433.
- [Scheibel, 2005b] Scheibel, T. (2005b). Protein fibers as performance proteins: new technologies and applications. *Current Opinion in Biotechnology*, 16(4):427–433.

- [Schäfer et al., 2008] Schäfer, A., Vehoff, T., Glisovi?, A., and Salditt, T. (2008). Spider silk softening by water uptake: an afm study. *Eur Biophys J*, 37(2):197–204.
- [Schroeder et al., 2003] Schroeder, C. M., Babcock, H. P., Shaqfeh, E. S. G., and Chu, S. (2003). Observation of polymer conformation hysteresis in extensional flow. *Science*, 301(5639):1515–1519.
- [Shao and Vollrath, 1999] Shao, Z. Z. and Vollrath, F. (1999). The effect of solvents on the contraction and mechanical properties of spider silk. *Polymer*, 40(7):1799–1806.
- [Slotta et al., 2007] Slotta, U., Hess, S., Spiess, K., Stromer, T., Serpell, L., and Scheibel, T. (2007). Spider silk and amyloid fibrils: A structural comparison. *Macromolecular Bioscience*, 7(2):183–188.
- [Slotta et al., 2006] Slotta, U., Tammer, M., Kremer, F., Koelsch, P., and Scheibel, T. (2006). Structural analysis of spider silk films. *Supramolecular Chemistry*, 18(5):465–471.
- [Slotta et al., 2008] Slotta, U. K., Rammensee, S., Gorb, S., and Scheibel, T. (2008). An engineered spider silk protein forms microspheres. *Angew Chem Int Ed Engl*, 47(24):4592–4594.
- [Smith et al., 1999] Smith, D. E., Babcock, H. P., and Chu, S. (1999). Single-polymer dynamics in steady shear flow. *Science*, 283(5408):1724–1727.
- [Smoluchowski, 1917] Smoluchowski, M. (1917). Essay of a mathematical theory of the coagulation kinetics of colloidal suspensions (translated from german). *Zeitschrift für Physikalische Chemie-Frankfurt*, 92(129):129–168.
- [Squires and Quake, 2005] Squires, T. M. and Quake, S. R. (2005). Microfluidics: Fluid physics at the nanoliter scale. *Reviews of Modern Physics*, 77(3):977–1026.
- [Termonia, 1994] Termonia, Y. (1994). Molecular modeling of spider silk elasticity. *Macromolecules*, 27(25):7378–7381.
- [Terry et al., 2004] Terry, A. E., Knight, D. P., Porter, D., and Vollrath, F. (2004). Ph induced changes in the rheology of silk fibroin solution from the middle division of bombyx mori silkworm. *Biomacromolecules*, 5(3):768–772.
- [Tripathi et al., 2006] Tripathi, A., Tam, K. C., and McKinley, G. H. (2006). Rheology and dynamics of associative polymers in shear and extension: Theory and experiments. *Macromolecules*, 39(5):1981–1999.
- [Trouton, 1906] Trouton, F. T. (1906). On the coefficient of viscous traction and its relation to that of viscosity. *Proceedings of the Royal Society of London Series a-Mathematical Physical and Engineering Sciences*, 77 (519):426 – 440.

## Bibliography

- [Um et al., 2001] Um, I. C., Kweon, H. Y., Park, Y. H., and Hudson, S. (2001). Structural characteristics and properties of the regenerated silk fibroin prepared from formic acid. *Int J Biol Macromol*, 29(2):91–97.
- [van Beek et al., 1999] van Beek, J. D., Kummerlen, J., Vollrath, F., and Meier, B. H. (1999). Supercontracted spider dragline silk: a solid-state nmr study of the local structure. *International Journal of Biological Macromolecules*, 24(2-3):173–178.
- [Vehoff et al., 2007] Vehoff, T., Glisovic, A., Schollmeyer, H., Zippelius, A., and Salditt, T. (2007). Mechanical properties of spider dragline silk: humidity, hysteresis, and relaxation. *Biophysical Journal*, 93(12):4425–4432.
- [Vollrath, 2005] Vollrath, F. (2005). Spiders' webs. *Current Biology*, 15(10):R364–R365.
- [Vollrath, 2006] Vollrath, F. (2006). Spider silk: thousands of nano-filaments and dollops of sticky glue. *Curr Biol*, 16(21):R925–R927.
- [Vollrath and Edmonds, 1989] Vollrath, F. and Edmonds, D. T. (1989). Modulation of the mechanical-properties of spider silk by coating with water. *Nature*, 340(6231):305–307.
- [Vollrath et al., 1996] Vollrath, F., Holtet, T., Thogersen, H. C., and Frische, S. (1996). Structural organization of spider silk. *Proceedings of the Royal Society of London Series B-Biological Sciences*, 263(1367):147–151.
- [Vollrath and Knight, 2001] Vollrath, F. and Knight, D. P. (2001). Liquid crystalline spinning of spider silk. *Nature*, 410(6828):541–548.
- [Vollrath et al., 1998] Vollrath, F., Knight, D. P., and Hu, X. W. (1998). Silk production in a spider involves acid bath treatment. *Proceedings of the Royal Society of London Series B-Biological Sciences*, 265(1398):817–820.
- [Vollrath et al., 2001] Vollrath, F., Madsen, B., and Shao, Z. Z. (2001). The effect of spinning conditions on the mechanics of a spider's dragline silk. *Proceedings of the Royal Society of London Series B-Biological Sciences*, 268(1483):2339–2346.
- [Winter and Noll, 1998] Winter, R. and Noll, F. (1998). Methoden der biophysikalischen chemie.
- [Zhou and Zhang, 2005] Zhou, H. and Zhang, Y. (2005). Hierarchical chain model of spider capture silk elasticity. *Physical Review Letters*, 94(2).



## A. Structural Comparison of Films formed from engineered spider silk and short fragments

In order to elucidate, whether the structural changes of the proteins observed in the spinning duct during fiber formation depend on the number of repetitive units in silk proteins, films of C16 engineered silk protein and three short fragments from this silk were investigated.

Solutions of spider silk and of the fragments shown in table A.1

Sequence	Origin	Mass (kDa)
AAAAAASGYGPEN	C	1.1
GSSAAAAAAG	C	1.0
GPGGP	C	0.42
GPQGP	C	0.41

**Table A.1.:** Synthesized fragments of engineered spider silk.

were prepared in HFIP and 10  $\mu$ l of each solution were pipetted onto CaF<sub>2</sub> windows. After drying, FTIR spectra of the films were obtained. C16, GPGGP and GPQGP and AAAAAASGYGPEN films showed mainly random coil conformation, as described previously for C16 films. However, GSSAAAAAAG films also showed a distinct peak at 1625 cm<sup>-1</sup>, indicating a large amount of  $\beta$ -sheet content.

In order to see whether these short peptide fragments would show the same structural changes upon Methanol treatment, 10  $\mu$ l Methanol were pipetted onto each film and allowed to evaporate completely. After drying there was no structural change in the GPGGP and GPQGP films. C16 as well as the fragment AAAAAASGYGPEN showed a distinct change in secondary structure composition. Remarkably, after methanol treatment, the absorbance peak of the AAAAAASGYGPEN peptide is much narrower than for the film of eADF4(C16) spider silk protein. This can be explained with the missing GPGGP and GPQGP motifs, which are present in the C motif, but not present in the AAAAAASGYGPEN fragment.

These results are in good agreement with previous studies on (AQ)12, C16, AQ24NR3, C16NR and combined films of these proteins [Slotta et al., 2006]. It

## A. Structural Comparison of Films formed from engineered spider silk and short fragments

was shown that the presence of the NR domain does not affect structural changes after methanol treatment at all. Also, the resistance of the methanol treated films to denaturing agents only depended on the repetitive motifs, not on the NR domain.

The fact that also the small fragments show a distinct change in secondary structure composition after methanol treatment shows that there is no cooperative effect between the repetitive sequences involved in the formation of beta-sheet structures. This indicates that the unusual size of silk proteins is not a prerequisite for secondary structure change, and that there are probably other aspects which directed the evolution of silk proteins towards the high number of repetitive units we observe.

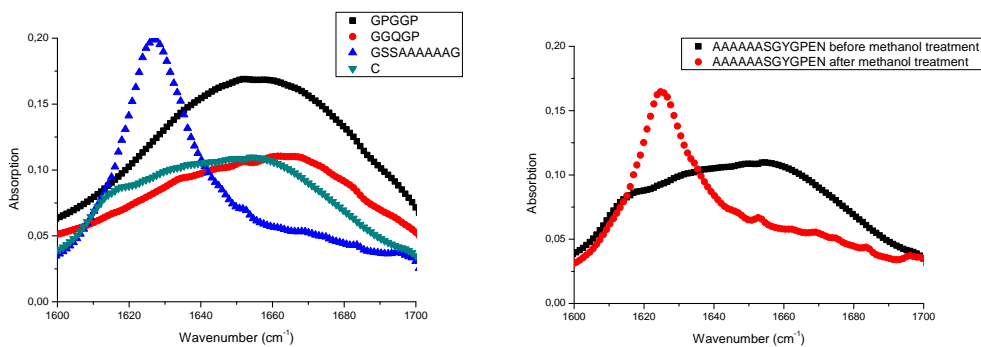


**Figure A.1.:** Infrared Spectra of Different Spider-Silk derived Peptide films. GSSAAAAAAG readily forms  $\beta$ -sheet rich secondary structure. The other films show mainly unstructured structure. Left: IR Absorption of films as cast. Right: IR Absorption of AAAAAASGYGPEN before and after treatment with Methanol.

The results of this experiments showed that spider silk proteins do not need to be especially long to show aggregation into films and to be able to change their secondary structure upon external triggers. AAAAAASGYGPEN was the smallest construct that could be switched from one conformation to another by treatment with methanol.

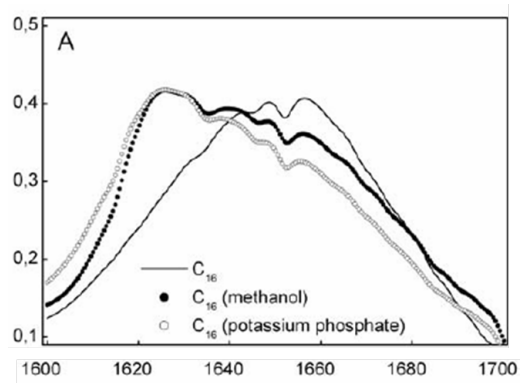


**Figure A.2.:** Amide I Band of C<sub>16</sub> films, untreated, with Methanol, and potassium phosphate. Figure from [Slotta et al., 2006]



## B. Fabrication of PDMS Microfluidic Devices

Microfluidic devices used in this work have been produced in the following way:

### B.1. Preparation of Masters

1. Preparation of lithography Masks: Masks were designed using Adobe Illustrator or Autocad software and then send to Lithofactory GmbH for printing at 4000 dpi on transparent film. Printing on a normal laser printer did not result in sufficient surface covering for exposition.
2. Substrates: Silicon wafers were purchased from Siltronic GmbH and cut to square pieces of approximately 3x3 cm. These pieces were washed in Acetone and Isopropanol, dried with Nitrogen and then dried in a vacuum chamber overnight.
3. Photoresists: Depending on the heights of the structures, a photoresist resin from the SU8 series (Microchem GmbH) was used. SU8-50, which yields a 50  $\mu\text{m}$  high film at 3000 RPM spinning speed was usually used. The times in the following steps refer to 50  $\mu\text{m}$  thickness, values for other thicknesses can be found in the SU-8 Data Sheet.
4. On the spin coater, about 1 ml of photoresist was pipetted centrally onto the slowly turning substrate (3x3 cm). Once the photoresist had wetted the substrate, the speed was ramped up to the final turning speed (3000 RPM mostly). The final RPM rate was maintained for 4 minutes, as the used photoresists are very viscous.
5. Softbake in convection oven: 20 minutes at 95 °C.
6. Exposition: Exposition was performed in a Karl Sues Mask Aligner. Exposition time for 50  $\mu\text{m}$  film thickness was 10 seconds. Exposition time might be adjusted, as the UV lamp gets weaker during its lifetime (check meters for voltage and current).
7. Post-exposure bake: 1 minute at 65 °C, 5 minutes at 95 °C.

## B. Fabrication of PDMS Microfluidic Devices

8. Develop: 6 minutes in SU8 Developer (1-Methoxy-2-propyl acetate).
9. Rinse with isopropyl alcohol, dry gently with air.
10. Treatment with (Tridecafluoro-1,1,2,2-tetrahydrooctyl)trichlorosilane (ACBR GmbH) to prevent strong sticking of PDMS to the photoresist structures. Masters were placed in vacuum chamber, a few drops of the trichlorosilane were placed next to it. Evacuation for 10 minutes.

### B.2. Preparation of PDMS Replicas

1. PDMS was purchased from WPI. PDMS polymer and curing agent (which is a thermally activated cross-linker) were mixed in a ratio of 10:1 on the lab balance and mixed well with the wide end of a Pasteur pipette.
2. The mixed PDMS was degassed for at least 1 hour.
3. PDMS was poured onto the Master Structures.
4. In case of excessive air bubbles in the PDMS covering the replica, a second degassing step was performed (1 hour).
5. PDMS and replica were heated in a convection oven to 75 °C for at least 1 hour.
6. Using a scalpel, the replicas were cut out.
7. Using green WPI (G) biopsy punchers, holes for tubing were punched.
8. To close the microfluidic devices, 60x22mm coverslips were used. These were washed in Hellmanex before usage: Pour 1% Hellmanex solution over coverslip and rub over the coverslip with gloved fingers for 1 minute (Latex gloves). Then the coverslip was thoroughly rinsed with millipore water and dried in Nitrogen stream.
9. PDMS replicas were washed with Isopropanol and also dried in Nitrogen stream.
10. Immediately after the washing steps, both the coverslips and the PDMS were treated with an UV plasma (Harrick PDC32G). Medium setting for 15 seconds. This is thought to induce silanol groups (Si-OH) in the PDMS, which then condense with suitable groups (OH, COOH, ketone) on the other surface when brought into contact [McDonald et al., 2000].

### *B.3. Preparation of Microfluidic Devices for Experiments*

11. Immediately after plasma treatment, the PDMS replicas and the coverslides are brought into contact and gently pressed together.
12. Before further use, the devices should rest for 1 hour to allow the surfaces to bond strongly.

### **B.3. Preparation of Microfluidic Devices for Experiments**

1. 1 % aqueous solution of Pluronic F108 (Ethylene oxide-propylene oxide block copolymer) is flushed into the channels. After incubation for 1 hour at 60 °C, the F108 solution is flushed out with millipore water.
2. Before experiments, the channels are filled with 10 mM Tris pH 8.





## C. Block Diagram for Fiber Tester

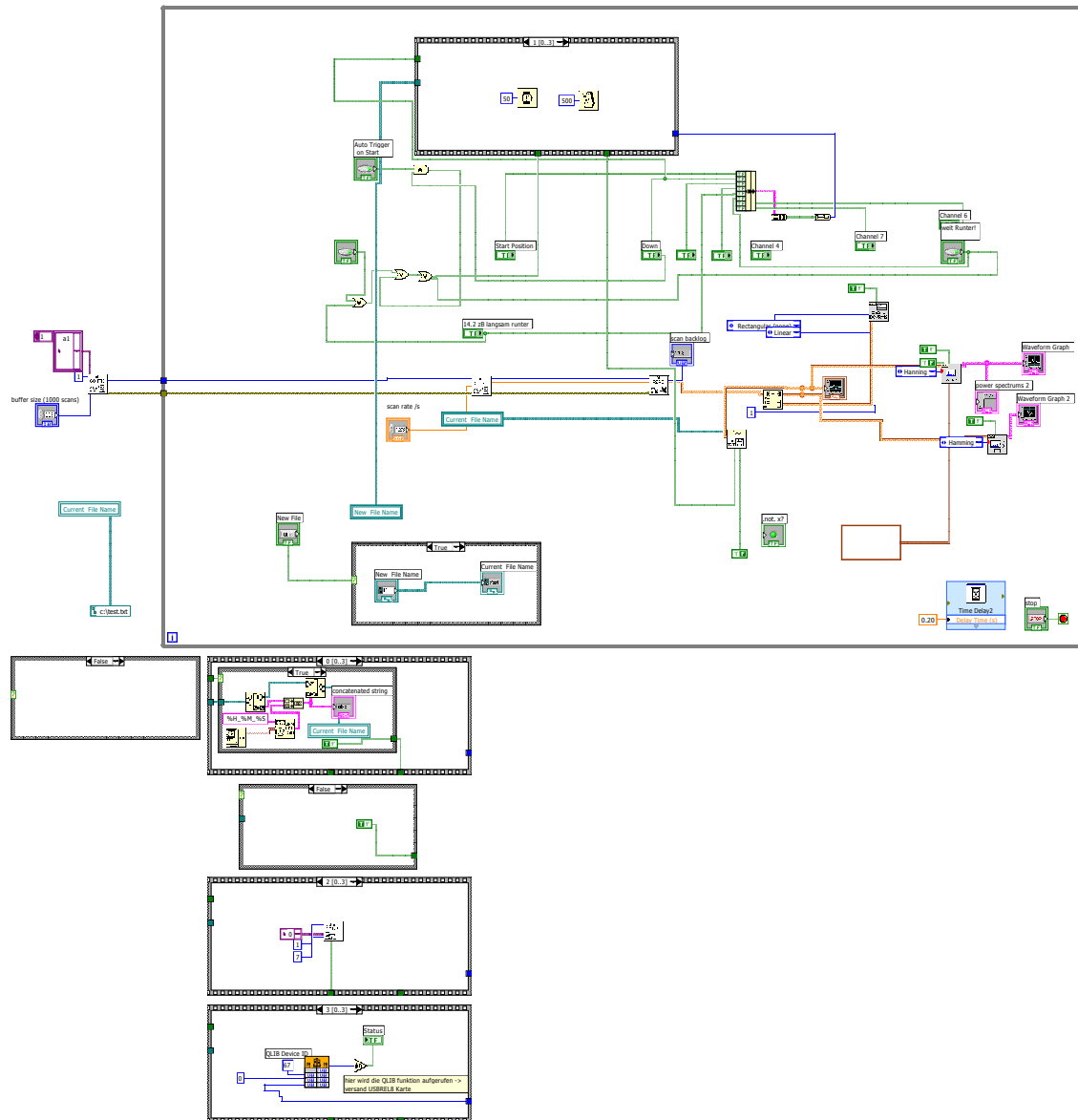


Figure C.1.: Block Diagram of the Labview Program that controls the fiber tester setup.

